The DOE E3SM coupled model version 1: Overview and evaluation at standard resolution

Jean-Christophe Golaz[1], Peter M. Caldwell[1], Luke P. Van Roekel[2], Mark R. Petersen[2], Qi Tang[1], Jonathan D. Wolfe[2], Guta Abeshu[3], Valentine Anantharaj[4], Xylar S. Asay-Davis[2], David C. Bader[1], Sterling A. Baldwin[1], Gautam Bisht[5], Peter A. Bogenschutz[1], Marcia Branstetter[4], Michael A. Brunke[6], Steven R. Brus[2], Susannah M. Burrows[7], Philip J. Cameron-Smith[1], Aaron S. Donahue[1], Michael Deakin[8,9], Richard C. Easter[7], Katherine J. Evans[4], Yan Feng[10], Mark Flanner[11], James G. Foucar[8], Jeremy G. Fyke[2,12], Brian M. Griffin[13], Cécile Hannay[14], Bryce E. Harrop[7], Elizabeth C. Hunke[2], Robert L. Jacob[10], Douglas W. Jacobsen[2], Nicole Jeffery[2], Philip W. Jones[2], Noel D. Keen[5], Stephen A. Klein[1], Vincent E. Larson[13], L. Ruby Leung[7], Hong-Yi Li[3], Wuyin Lin[15], William H. Lipscomb[14], Po-Lun Ma[7], Salil Mahajan[4], Mathew E. Maltrud[2], Azamat Mametjanov[10], Julie L. McClean[16], Renata B. McCoy[1], Richard B. Neale[14], Stephen F. Price[2], Yun Qian[7], Philip J. Rasch[7], J. E. Jack Reeves Eyre[6], William J. Riley[5], Todd D. Ringler[17], Andrew F. Roberts[2], Erika L. Roesler[8], Andrew G. Salinger[8], Zeshawn Shaheen[1], Xiaoying Shi[4], Balwinder Singh[7], Jinyun Tang[5], Mark A. Taylor[8], Peter E. Thornton[4], Adrian K. Turner[2], Milena Veneziani[2], Hui Wan[7], Hailong Wang[7], Shanlin Wang[2], Dean N. Williams[1], Philip J. Wolfram[2], Patrick H. Worley[18], Shaocheng Xie[1], Yang Yang[7], Jin-Ho Yoon[19], Mark D. Zelinka[1], Charles S. Zender[20], Xubin Zeng[6], Chengzhu Zhang[1], Kai Zhang[7], Yuying Zhang[1], Xue Zheng[1], Tian Zhou[7], Qing Zhu[5]

[1]Lawrence Livermore National Laboratory, Livermore, CA

[2]Los Alamos National Laboratory, Los Alamos, NM

[3]University of Houston, Houston, TX

[4]Oak Ridge National Laboratory, Oak Ridge, TN

[5]Lawrence Berkeley National Laboratory, Berkeley, CA

[6]University of Arizona, Tucson, AZ

[7]Pacific Northwest National Laboratory, Richland, WA

[8]Sandia National Laboratory, Albuquerque, NM

[9]University of British Columbia, Vancouver, BC Canada

[10]Argonne National Laboratory, Lemont, IL

[11]University of Michigan, Ann Arbor, MI

[12]Associated Engineering Group of Companies, Edmonton, AB, Canada

[13]University of Wisconsin – Milwaukee, Milwaukee, WI

[14]National Center for Atmospheric Research, Boulder, CO

[15]Brookhaven National Laboratory, Upton, NY
[16]Scripps Institution of Oceanography, University of California, San Diego, La Jolla, CA
[17]Congressional Science Fellow, U.S. House of Representatives, Washington, DC
[18]PHWorley Consulting, Oak Ridge, TN
[19]Gwangju Institute of Science and Technology, Gwangju, Korea
[20]University of California, Irvine, CA

Key Points:

- Description of E3SMv1, the first version of the U.S. DOE Energy Exascale Earth Sytem Model.
- The performance of E3SMv1 is documented with a set of standard CMIP6 DECK and historical simulations comprising nearly 3000 years.
- E3SMv1 has a high equilibrium climate sensitivity (5.3 K) and strong aerosol-related effective radiative forcing (-1.65 W m^{-2}).

Corresponding author: Chris Golaz, golaz1@llnl.gov

Abstract

This work documents the first version of the U.S. Department of Energy (DOE) new Energy Exascale Earth System Model (E3SMv1). We focus on the standard resolution of the fully-coupled physical model designed to address DOE mission-relevant water cycle questions. Its components include atmosphere and land (110km grid spacing), ocean and sea ice (60km in the mid-latitudes and 30km at the equator and poles), and river transport (55km) models. This base configuration will also serve as a foundation for additional configurations exploring higher horizontal resolution as well as augmented capabilities in the form of biogeochemistry and cryosphere configurations.

The performance of E3SMv1 is evaluated by means of a standard set of Coupled Model Intercomparison Project Phase 6 Diagnosis, Evaluation, and Characterization of Klima (CMIP6 DECK) simulations consisting of a long pre-industrial control, historical simulations (ensembles of fully coupled and prescribed SSTs) as well as idealized CO_2 forcing simulations. The model performs well overall with biases typical of other CMIP-class models, although the simulated Atlantic Meridional Overturning Circulation is weaker than many CMIP-class models. While the E3SMv1 historical ensemble captures the bulk of the observed warming between pre-industrial (1850) and present-day, the trajectory of the warming diverges from observations in the second half of the 20th century with a period of delayed warming followed by an excessive warming trend. Using a two-layer energy balance model, we attribute this divergence to the model's strong aerosol-related effective radiative forcing ($ERF_{ari+aci}$ = -1.65 W m^{-2}) and high equilibrium climate sensitivity (ECS = 5.3 K).

Plain Language Summary

The United States Department of Energy funded the development of a new state-of-the-art Earth system model for research and applications relevant to its mission. The Energy Exascale Earth System Model version 1 (E3SMv1) consists of five interacting components for the global atmosphere, land surface, ocean, sea ice and rivers. Three of these components (ocean, sea ice and river) are new and have not been coupled into an Earth system model previously. The atmosphere and land surface components were created by extending existing components part of the Community Earth System Model, Version 1.

E3SMv1's capabilities are demonstrated by performing a set of standardized simulation experiments described by the Coupled Model Intercomparison Project Phase 6 Diagnosis, Evaluation, and Characterization of Klima (CMIP6 DECK) protocol at standard horizontal spatial resolution of approximately 1 degree latitude and longitude. The model reproduces global and regional climate features well compared to observations. Simulated warming between 1850 and 2015 matches observations, but the model is too cold by about 0.5°C between 1960 and 1990 and later warms at a rate greater than observed. A thermodynamic analysis of the model's response to greenhouse gas and aerosol radiative affects may explain the reasons for the discrepancy.

1 Introduction

In 2013, the US Department of Energy (DOE) developed a report summarizing observed long-term trends that, if continued for several decades, would have major impacts on the energy sector [*U.S. Department of Energy*, 2013]. Among these were regional trends in air and water temperatures, water availability, storms and heavy precipitation, coastal flooding and sea-level rise. The ability to simulate and predict significant, long-term changes in these environmental variables important to energy-sector decisions required capabilities beyond the existing state-of-the-science Earth system models. The Energy Exascale Earth System Model (E3SM) project was conceived to meet this mission need [*Bader et al.*, 2014].

Scientific developments in E3SM are dictated by three science drivers that broadly cover the foundational science for advancing Earth system prediction. Notably, water cycle, biogeochemistry, and cryosphere systems govern variability and changes in water availability and storms, air and river stream temperature, and coastal flooding and sea level rise that are all critical to the energy sector [*Leung et al.*, 2019].

E3SM version 1 (E3SMv1) was branched from the Community Earth System Model (CESM1; *Hurrell et al.* [2013]) but has evolved significantly since. E3SMv1 consists of three coupled modeling systems with varying degrees of sophistication. The present work describes the physical Earth system model that represents water and energy cycles in atmosphere, ocean, sea ice, land and river components. This configuration is aimed at addressing the DOE water cycle science questions relating to interactions between the water cycle and the rest of the human-Earth system on local to global scales, water availability, and water cycle extremes. This physical model also serves as a foundation for two additional configurations: (i) a biogeochemistry configuration with interactive nitrogen and phosphorous for interactions between biogeochemical cycles and other Earth system components and (ii) a cryosphere configuration with added interactive ice-shelf cavities for assessing the impacts of ocean-ice shelf interactions on Antarctic Ice Sheet dynamics and the implications for sea level rise.

The focus here is on the physical model at standard resolution useful for simulations like those specified in Coupled Model Intercomparison Project Phase 6 (CMIP6). This includes a 1° atmosphere and land (equivalent to 110 km at the equator), 0.5° river model (55 km), and an ocean and sea ice with mesh spacing varying between 60 km in the mid-latitudes and 30 km at the equator and poles. A higher resolution configuration with a 0.25° atmosphere and land, 0.125° river model, and ocean and sea ice with mesh spacing between 18 km at the equator and 6 km at the poles (roughly equivalent to a 0.1° resolution) will be documented in a subsequent paper.

Given that E3SMv1 features three specific models of components (ocean, sea ice, and river) that have never been used in a coupled Earth System Model and that there were significant developments in the atmosphere and land components, an examination of the model behavior relative to observations and other CMIP class models is needed. We analyze CMIP6 Diagnosis, Evaluation, and Characterization of Klima (DECK) and historical simulations [*Eyring et al.*, 2016] performed with E3SMv1. This allows for a rigorous comparison of E3SMv1 behavior against observations and many other models. This work will also provide a baseline for all future E3SM developments and experiments.

This paper is organized as follows. In Section 2, we present an overview of the model components, with a specific focus on new model components (i.e., those not previously used in coupled Earth system modeling), as well as new developments in the atmosphere and land models. In Section 3, we describe the E3SMv1 initialization and spin-up procedure, including model tuning objectives and simulation campaign. Section 4 provides an overview of the pre-industrial control simulation and Section 5 an analysis of the E3SMv1 climate in the historical simulations including short and long-term variability. An extended discussion of E3SMv1's Effective Radiative Forcing (ERF) and climate sensitivity is provided in Section 6. Finally, we offer a summary of E3SMv1 fidelity and discuss future directions for the fully coupled model in Section 7.

2 Model Overview

E3SM started with a version of the CESM1 [*Hurrell et al.*, 2013, http://www.cesm.ucar.edu/models/cesm1.0] from which we developed the fully coupled E3SMv1 system. Notable changes between E3SMv1 and CESM1 include:

- E3SM Atmosphere Model (EAM) component with a spectral-element (SE) dynamical core, increased vertical resolution, and substantially revamped physics and the capability of regional grid refinement for multi-resolution simulations.

- New ocean and sea-ice components based on the Model for Prediction Across Scales (MPAS) framework that uses Spherical Centroidal Voronoi Tessellations (SCVTs) for multi-resolution modeling.
- The river transport model of CESM1 was replaced by a new river model, Model for Scale Adaptive River Transport (MOSART), for a more physically based representation of riverine processes.
- E3SMv1 land model (ELM) is based on the Community Land Model Version 4.5 (CLM4.5) with new options for representing soil hydrology and biogeochemistry added to enable analysis of structural uncertainty, with important implications to carbon cycle and climate feedbacks for addressing v1 biogeochemistry questions.

The sub-sections below provide a more detailed description of the model components. Coupling of the new MPAS-Ocean, MPAS-Seaice and MOSART models with EAM and ELM provides E3SMv1 with a unique capability for multi-resolution modeling using unstructured grids in most of its component models. This capability is critical for future simulation campaigns that have a strong regional focus to meet DOEâĂŹs needs for Earth system modeling in support of energy-sector decisions.

The project also built a comprehensive infrastructure for code management, development, testing, and analysis to enable development of E3SMv1 and future versions at DOE leadership computing centers. Leveraging DOE investments, a flexible framework provides workflow orchestration, provenance capture and management, simulation analysis and visualization, and automated testing and evaluation capabilities (see Appendix C: for a description of some of the analysis tools).

2.1 Atmosphere

The E3SM Atmosphere Model (EAM) is the atmosphere component of E3SMv1. It is a descendant of the Community Atmosphere Model version 5.3 (CAM5.3). EAM uses a spectral element dynamical core at 100 km resolution on a cubed-sphere geometry. Vertical resolution was increased from 30 layers, with a top at approximately 40 km, in CAM5 to 72 layers with a top at approximately 60 km in EAM. EAM contains many innovations compared to CAM5. While changes in the EAM physics are broadly similar to changes from CAM5.3 to CAM6, many details of tuning, and cloud and aerosols formulations differ in important ways. EAM is described in *Rasch et al.* [2019]. A detailed analysis of its cloud and convective characteristics and the rationale for model tuning are provided in *Xie et al.* [2018]. Sensitivity of EAM to a number of its adjustable parameters is explored in *Qian et al.* [2018].

Key features of EAMv1 include:

- Implementation of a simplified third-order turbulence closure parameterization (CLUBB; Cloud Layers Unified By Binormals) [*Golaz et al.*, 2002; *Larson and Golaz*, 2005; *Larson*, 2017] that unifies the treatment of planetary boundary layer turbulence, shallow convection, and cloud macrophysics.
- An updated microphysical scheme, the version 2 of *Morrison and Gettelman* [2008] [MG2; *Gettelman et al.*, 2015]. The combination of CLUBB and MG2 enables aerosol-cloud interactions in large-scale and shallow convective clouds to be considered. Significant additional changes to nucleation and ice microphysics have also been incorporated compared to MG2 in CAM6.
- The deep convection scheme of *Zhang and McFarlane* [1995].
- The Modal Aerosol Module (MAM4) with revisions to improve aerosol resuspension, convective transport, aerosol nucleation, scavenging, as well as modifications to sea spray emissions so marine ecosystems can contribute organic matter to aerosols.
- A linearized ozone photochemistry to predict stratospheric ozone changes, which provides an important source of stratospheric variability (Linoz v2, *Hsu and Prather* [2009]).

The computational cost of EAMv1 increased by approximately a factor of four relative to CAM5 due to higher vertical resolution and parameterization complexity, along with a larger number of predicted and transported variables (aerosol species and prognostic snow and rain).

2.2 Ocean

MPAS-Ocean, based on the Model for Prediction Across Scales (MPAS) framework [*Ringler et al.*, 2010], is the ocean component of E3SMv1. MPAS-Ocean uses a mimetic finite volume discretization of the primitive equations and invokes the hydrostatic, incompressible, and Boussinesq approximations on a staggered C-grid [*Arakawa and Lamb*, 1977; *Thuburn et al.*, 2009; *Ringler et al.*, 2013]. MPAS-Ocean grid cells for E3SMv1 simulations are near-hexagons (five or more sides), but the MPAS framework supports cells with any number of sides; the algorithms and code are identical for all cell shapes. The tracer advection scheme is the quasi 3rd-order flux corrected transport (FCT) scheme [*Skamarock and Gassmann*, 2011] with separate limiting in the horizontal and vertical. The MPAS-Ocean time stepping method is split-explicit, where the barotropic component is subcycled within each baroclinic time step.

The simulations presented here use a z-star vertical coordinate within an arbitrary Lagrangian-Eulerian scheme, where the layer thicknesses of the full column expand and contract with the sea surface height [*Petersen et al.*, 2015; *Reckinger et al.*, 2015]. The prognostic volume-based equation of motion includes surface mass fluxes from the coupler, thus virtual salt fluxes are not needed. Vertical mixing is computed implicitly at the end of each time step using the Community Vertical Mixing project implementation of the K-profile parameterization (KPP) as described by *Van Roekel et al.* [2018] where our configuration of KPP is based on the results of comparison against large eddy simulations.

E3SMv1 standard resolution simulations employ the classic *Gent and McWilliams* [1990] eddy transport (GM) parameterization. The GM bolus coefficient was tuned, in part, to reduce the transport of heat to depth in the Southern Ocean, to a value of 1800 $m^2\ s^{-1}$ for the simulations presented here. The Redi coefficient, which adds diffusion along isopycnal layers, was set to zero for this set of simulations. In the horizontal, biharmonic viscosity is used for momentum ($1.2 \times 10^9\ m^4\ s^{-2}$). No explicit horizontal tracer diffusivity is included.

2.3 Sea ice

MPAS-Seaice is the sea ice component of E3SMv1. MPAS-Seaice and MPAS-Ocean share identical meshes, but MPAS-Seaice uses a B-grid [*Arakawa and Lamb*, 1977] with sea-ice concentration, volume, and tracers defined at cell centers and velocity defined at cell vertices. Velocity components at cell vertices are not aligned with the mesh, as in sea-ice models with structured meshes and quadrilateral cells. Instead, the velocity components are aligned with a spherical coordinate system that is locally Cartesian and has its poles on the geographical equator. Velocities are determined by solving the sea-ice momentum equation [*Hibler III*, 1979; *Hunke and Dukowicz*, 1997] on cell vertices in an identical manner to the CICE model [*Hunke et al.*, 2015] except for the internal stress term. MPAS-Seaice uses the variational formulation of the internal stress term used by CICE [*Hunke and Dukowicz*, 2002], but modified to use the non-regular polygons of MPAS meshes. Instead of the bilinear basis functions used by CICE, MPAS-Seaice uses Wachspress basis functions [*Dasgupta*, 2003], which are integrated with the quadrature rules of *Dunavant* [1985]. Horizontal transport of ice concentration, volume, and tracers is achieved with an incremental remapping scheme similar to that described in *Dukowicz and Baumgardner* [2000], *Lipscomb and Hunke* [2004] and *Lipscomb and Ringler* [2005] but adapted to MPAS meshes. MPAS-Seaice shares the same column physics code as CICE through the Icepack library [*Hunke et al.*, 2018]. For simulations shown here, MPAS-Seaice uses the "mushy layer" vertical thermodynamics scheme of *Turner et al.* [2013]; *Turner and Hunke* [2015], the level-ice melt pond scheme of *Hunke et al.* [2013], a delta-Eddington shortwave radiation scheme [*Briegleb and Light*, 2007; *Holland et al.*, 2012], a scheme for transport in thickness space [*Lipscomb*, 2001], and a representation of mechanical redistribution [*Lipscomb et al.*, 2007].

Coupling of the sea-ice component to the ocean takes advantage of z-star ocean coordinates as described by *Campin et al.* [2008], and is a departure from the coupling of CICE and POP in CESM1. The weight of sea ice contributes to the ocean's barotropic mode, notably affecting the free surface over continental shelves. In shallow water depths at or less than the floating ice draft, the weight passed to the ocean model is limited to prevent evacuation of the underlying liquid column. When frazil ice forms in the ocean model, the volume of newly formed crystals is passed to the sea ice model with a fixed salinity of 4 PSU, rather than exchanging a freezing potential as in other models. Future versions of E3SM will permit progressive brine drainage to the ocean from the mushy-layer physics used in MPAS-Seaice [*Turner and Hunke*, 2015]. For E3SMv1, brine drainage occurs internally in MPAS-Seaice for thermodynamic calculations, but for the sake of freshwater coupling, the ocean model only receives mass fluxes back from melted sea ice at the fixed salinity that it originally passed to its cryospheric counterpart (4 PSU). The ocean temperature immediately under the ice is the same as the liquid phase in the lowest layer of the sea ice model, and is not fixed at -1.8°C as is typical of previous generation coupled models [*Naughten et al.*, 2017]. For the current version, we have addressed these long-standing ocean-ice coupling issues identified by the modeling community: explicit sea ice mass and salt exchange, a pressure force of the ice on the ocean, a basal sea ice temperature consistent with the ocean model's equation of state, and resolved inertial oscillations [*Schmidt et al.*, 2004; *Hibler et al.*, 2006; *Lique et al.*, 2016].

2.4 Land

The E3SM Land Model, version 0 (ELMv0) is the land component in E3SMv1. ELMv0 adopts many of its capabilities from its parent model, the Community Land Model version 4.5 (CLM4.5). *Oleson et al.* [2013] provide a detailed technical description of that parent model, including descriptions of all fundamental equations representing the modelâĂŹs biogeophysical and biogeochemical dynamics. The model describes interactions of the land surface with the near-surface atmosphere, and includes interactions among land sub-systems such as vegetation, soil, snow, groundwater, runoff, urban areas, and managed ecosystems. These interactions are represented through conservation equations of state for energy, water, carbon, and nitrogen, including terms that couple these states and fluxes. While ELMv0 includes prognostic carbon and nitrogen biogeochemistry and dynamic ecosystem structure, the E3SMv1 water cycle experiments do not make use of these capabilities. Instead, these simulations use a static representation of land ecosystem structure with prescribed seasonal changes in vegetation canopies based on a climatology of satellite remote sensing data. This simulation mode is referred to as satellite phenology (SP), and is based on methods described by *Lawrence and Chase* [2007]. In this simulation mode, regardless of long-term climate changes or short-term anomalies, the global distribution and seasonal variation of vegetation structure is constant over the course of the simulations. This includes model representation of vegetation height, timing and amount of displayed leaf area, and vegetation contributions to land surface albedo.

Several new developments have been made within ELMv0 since its branch point from CLM4.5. First, an extended representation of the influence of aerosols and black carbon deposition on snow was introduced, based on data summarized by *Liu et al.* [2012], causing aerosol optical properties within the snowpack to vary as a function of snow grain size and aerosol/ice mixing state [*Flanner et al.*, 2012]. This development also fixed a bug related to calculation of snow grain size following snow layer division. Second, a minor modification was made to reduce the rate of evaporation from area characterized as pervious road under dry conditions. Third, the numerical scheme for calculation of leaf stomatal conductance was updated to prevent non-physical simulation of negative internal leaf

CO_2 concentrations. Fourth, albedo calculation was modified to return a land albedo of 1.0 in land cells and time steps when the sun is below the horizon.

2.5 River

E3SMv1 replaced the River Transport Model (RTM) [*Branstetter and Erickson III*, 2003], a linear reservoir routing model used in CESM1 and E3SMv0, with the Model for Scale Adaptive River Transport (MOSART), which uses a physically-based kinematic wave approach for river routing across local, regional and global scales [*Li et al.*, 2013, 2015]. In the standard E3SMv1 resolution, MOSART uses a regular latitude-longitude grid with spacing of 0.5°. Surface and subsurface runoff simulated by ELM are mapped from the ELM grid to the 0.5° latitude-longitude grid as input to MOSART, which routes the runoff and provides freshwater input to the ocean model. MOSART does not exchange water with the atmosphere or return water to the land model. MOSART divides each grid cell into three categories of hydrologic units: hillslopes that contribute both surface and subsurface runoff into tributaries, tributaries that discharge into a single main channel, and the main channel that connects the local grid cell with the upstream/downstream grid cells through the river network. Two simplified forms of the one-dimensional Saint-Venant equations are used to represent water flow over hillslopes, in the tributary, or in the main channels. MOSART only routes positive runoff, although spurious negative runoff can be generated occasionally by the land model. Negative runoff is mapped directly from the grid cell where it is generated at any time step to the basin outlet of the corresponding MOSART grid cell. More detailed descriptions of MOSART and its input hydrography data and channel geometry parameters can be found in *Li et al.* [2013]. When driven by runoff simulated by CLM4 with observed meteorological forcing data, streamflow simulated by MOSART is shown to reproduce the observed annual, seasonal, and daily flow statistics at over 1600 stations of the world's major rivers reasonably well in terms of the overall bias and the seasonal variation [*Li et al.*, 2015].

2.6 Coupling and performance

E3SMv1 uses component coupling software from the Common Infrastructure for Modeling the Earth (CIME). The top level driver is cpl7 [*Craig et al.*, 2012], which provides a main program for forming the single executable of E3SM, directs the time integration of the coupled model, and performs any necessary interpolation or time averaging needed between the components. Communication between the parallel components of E3SM and parallel interpolation is provided by the Model Coupling Toolkit [*Jacob et al.*, 2005; *Larson et al.*, 2005] which is included in CIME.

cpl7 implements an online-offline method for interpolating values between different grids in E3SMv1. Grid intersections and interpolation weights are calculated with an offline tool and then read in at runtime and applied during the coupled integration. cpl7 also allows flux and state variables to be interpolated with different weights. The number of different weight files needed is relatively small because the atmosphere and land models share a grid, as do the ocean and sea-ice models. The interpolation weights for nearly all variables are calculated with the ESMF_RegridWeightGen program from ESMF [*Collins et al.*, 2005] using the first-order conservative option. However interpolation weights for state variables from the atmosphere to the ocean/sea ice grids are calculated using TempestRemap [*Ullrich and Taylor*, 2015]. Unlike ESMF, the TempestRemap algorithms have native support for vertex centered finite element grids, such as used by the E3SM atmosphere dycore. Future versions of E3SM will use TempestRemap for all mapping weight calculations.

cpl7 allows several time sequencing options for the components and flexibility for how often the components communicate with the coupler. E3SMv1 uses “RASM_OPTION1" where the sea ice, land and river runoff models execute simultaneously and in sequence with the atmosphere. The ocean model runs simultaneously with all four of those components. Model timesteps are as follows:

- The main atmosphere physics timestep is 30 min, but a few parameterizations use a different timestep. CLUBB and MG2 microphysics are substepped together at a timestep of 5 min. Radiation is updated hourly. Several layers of substepping are used by the atmosphere dynamics and tracer transport: the Lagrangian vertical discretization uses 15 min timesteps, the horizontal discretization uses 5 min timesteps, and the explicit numerical diffusion uses 100 sec timesteps.
- Ocean model timestep is 10 min with a barotropic sub-timestep of 40 sec.
- Sea-ice model timestep is 30 min. The 30 min coupling timestep between the sea-ice and ocean permits transient inertial oscillations in the drift of ice. This can cause instabilities arising from frequent exchange of sea ice weight and sea surface

height between sea-ice and ocean. Thus, we damp the sea-surface-height gradient in the sea-ice momentum equation with a 24-hour Newtonian relaxation constant.

- Land model timestep is 30 min.
- River runoff model timestep is 1 hour.

The coupling frequency for all components is 30 minutes except the river runoff model which communicates every 3 hours.

Simulations in this work were performed on DOE's National Energy Research Scientific Computing Center (NERSC) Edison supercomputer (http://www.nersc.gov/users/computational-systems/edison). Using 285 nodes (each consisting of two 12-core Intel “Ivy Bridge" processors at 2.4 GHz) with 24 MPI tasks per node, the coupled model performance averages 10 simulated years per day. Figure 1 illustrates the sequencing, processor layout and relative cost for all components in E3SMv1.

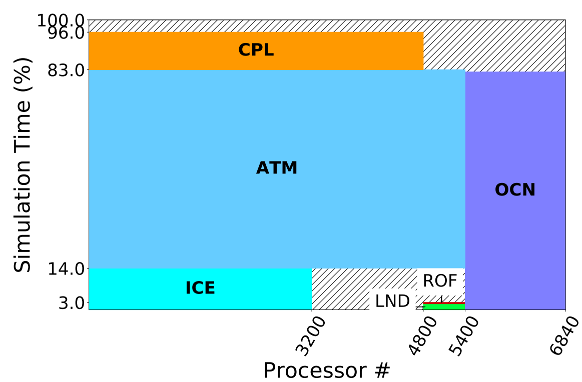

Figure 1. Typical processor layout, performance and sequencing for all components in E3SMv1. Components include coupler (CPL), atmosphere (ATM), ocean (OCN), sea ice (ICE), land (LND) and river runoff (ROF). The hatched area represents unoccupied time. OCN runs concurrently on its own nodes and is load-balanced with ATM+ICE, which run sequentially. Driver overhead is 4%. Other layouts are possible, but we have found this to be the most robust and efficient.

3 Tuning and initialization

3.1 Final coupled model tuning

Tuning is an integral part of climate model development [e.g., *Hourdin et al.*, 2017; *Schmidt et al.*, 2017]. While most of the tuning for E3SMv1 was performed at the model

Table 1. Atmospheric physics parameters that were altered during the development of the coupled model.

Parameter	Initial	Final	Impact	Motivation
`zmconv_ke`	1.5e-06	5.0e-06	Deep convection rain evaporation	MG2 bug fix 1
`so4_sz_thresh_icenuc`	7.5e-08	5.0e-08	SO_4 ice nucleation threshold size	MG2 bug fix 2
`clubb_c14`	1.30	1.06	CLUBB dissipation for $\overline{u'^2}$ and $\overline{v'^2}$	Final coupled tuning

component level, some additional retuning was subsequently required for two reasons: (1) code errors were discovered in the atmosphere model physics while the coupled system was being developed and (2) the coupled tuning objectives required an additional level of adjustment to accommodate biases present in other model components and interactions between components. Two minor code errors were discovered and addressed in EAMv1:

1. An incorrectly positioned parenthesis in the code designed to prevent over-depletion of rain number when multiple microphysics processes act to concurrently deplete rain drops (`https://github.com/E3SM-Project/E3SM/pull/1599`) led to a reduction in the rain drop number concentration process rate. Correcting the error produced a degradation in overall precipitation pattern, approximately compensated for through increasing the efficiency of convective precipitation evaporation with `zm_conv_ke` (see Table 1)
2. Snow crystal number concentration was updated improperly when snow sublimation occurred (`https://github.com/E3SM-Project/E3SM/pull/1765`). Fixing the error decreased the ice water path, weakening both LW and SW cloud radiative effects, which was then countered by a reduction in the sulfate threshold ice nucleation size `so4_sz_thresh_icenuc` to increase ice number concentration (Table 1).

A final tuning of the coupled model with pre-industrial (perpetual 1850) forcings was performed to achieve:

1. A near-zero long-term average net top-of-atmosphere (TOA) energy flux.
2. Minimum long-term drift in global mean surface air temperature.
3. Reasonable absolute global mean surface air temperature.

This final tuning required adjustments of less than one W m^{-2} because the E3SM atmosphere component was already well tuned from simulations with prescribed SSTs and sea-ice concentrations. To simplify the process, we chose to focus on a single parameter in the CLUBB atmosphere turbulence parameterization, `clubb_c14`, which directly impacts dissipation of the horizontal components of the turbulent kinetic energy (TKE). Because of the tight coupling between TKE and boundary layer clouds, `clubb_c14` modulates low-clouds, thus affecting net TOA mostly through SW cloud radiative effects.

While most of the coupled tuning was performed under pre-industrial conditions, we also performed a few additional simulations to monitor climate sensitivity and total effective radiative forcing during the developmental phase of E3SMv1. We evaluated sensitivity using idealized +4 K simulations [*Cess et al.*, 1989] and one abrupt quadrupling of CO_2. Total effective radiative forcing was estimated using pairs of atmosphere simulations with identical SSTs but differing forcing (climatological 2000 vs 1850). One historical test simulation was also performed with a near final version of E3SMv1 ("beta3rc10" below). The outcomes of these intermediate simulations were consistent with the final model. A pragmatic, but deliberate, decision was made not to attempt to reduce the high climate sensitivity or reduce the aerosol forcing. We note however that parameters controlling the autoconversion of cloud water to rain were adjusted during the development of the atmosphere component, resulting in a reduction in the magnitude of the aerosol forcing by approximately 0.3 W m^{-2} [*Rasch et al.*, 2019].

3.2 Spin-up and initialization

Since the coupled ocean and sea-ice system take centuries to spin-up, we chose to accelerate the process by simultaneously performing model spin-up and final coupled tuning. MPAS-Ocean was initially spun up for one year in stand-alone mode, from the Polar science center Hydrographic Climatology (PHC) dataset [*Steele et al.*, 2001] from rest. During this spin-up, sea surface temperature and salinity were relaxed to an annual mean climatology (from PHC) and the currents were forced by an annual averaged CORE-II normal year wind stress [*Large and Yeager*, 2009]. This was followed by a ten year Coordinated Ocean-ice Reference Experiments (CORE-II), inter-annually varying, forced [*Large and Yeager*, 2009] ocean and sea-ice simulation. The ocean and sea-ice state at the end of that simulation served as initial conditions for a series of sequential fully coupled simulations with pre-industrial forcing (Fig. 2).

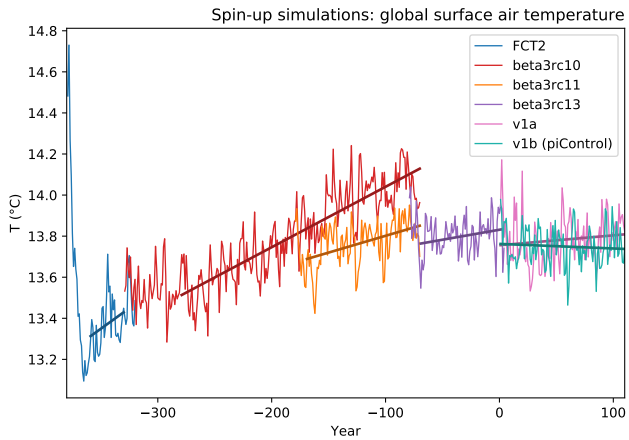

Figure 2. Time evolution of annual global mean surface air temperature for the spin-up simulations. Year 1 marks the first year of CMIP6 DECK *piControl*.

The first of these simulations consisted of 50 years with a prototype E3SMv1 configuration ("FCT2"). Due to the change in forcing from present-day CORE-II to pre-industrial coupled, the simulation experienced a rapid cooling during the first 20 years followed by a relative stabilization. Ocean and sea-ice states after 50 years served as initial conditions for a new coupled simulation ("beta3rc10") that included bug fixes and associated retuning described in Table 1, full implementation of the CMIP6 *piControl* forcings, and a retuning of `clubb_c14` from 1.3 to 1.2 based on a few previous tuning attempts with the "FCT2" model configuration. This beta3rc10 configuration was run for a total of 260 years; it exhibited excessive net influx of energy at TOA and a long-term warm drift with average temperature approaching present-day values near the end, even with pre-industrial forcings. As a result, a new configuration ("beta3rc11") was branched off after 150 years reusing all components states as initial conditions, but with a slight retuning of `clubb_c14` (1.2 to 1.1). This new configuration was run for a total of 100 years. Initially, it cooled slightly from the impact of the retuning, then drifted warm, albeit at a smaller pace than its predecessor. The process was repeated once again with "beta3rc13", further reducing `clubb_c14` from 1.1 to 1.08. This last simulation was run for a total of 80 years. The drift was smaller than the preceding attempt, but 80 years was too short to conclude that the drift had been removed entirely.

At that point, a decision was made to incorporate a minor code change in the atmospheric dynamical core. This change was a workaround for a compiler bug (https:

//github.com/E3SM-Project/E3SM/pull/1922). In the interest of time, two new simulations were started simultaneously from the end of beta3rc13, one with identical tuning ("v1a") and one with a further retuning of the `clubb_c14` parameter from 1.08 to 1.06 ("v1b"). After 110 years, both simulations were examined and "v1b" was selected as the official E3SMv1 tuning because it exhibited the smaller drift of the two.

Table 2. Summary of E3SMv1 simulations.

Label	Description	Period	Ens.	Initialization
piControl	Pre-industrial control	500 years	-	Pre-industrial spinup (Sect. 3.2)
1pctCO2	Prescribed 1% yr^{-1} CO_2 increase	150 years	1	*piControl* (101)
abrupt-4xCO2	Abrupt CO_2 quadrupling	150 years	1	*piControl* (101)
historical_Hn	Historical	1850-2014	5	*piControl* (101, 151, 201, 251, 301)
amip_An	Atmosphere with prescribed SSTs and sea-ice concentration	1870-2014	3	*historical_Hn* (1870)
amip_1850allF_An	Same, but with all forcings held at 1850 values	1870-2014	3	*historical_Hn* (1870)
amip_1850aeroF_An	Same, but with all aerosol forcings held at 1850 values	1870-2014	3	*historical_Hn* (1870)

3.3 Simulation campaign

Table 2 summarizes the E3SMv1 simulation campaign. All simulations were configured to adhere to the CMIP6 DECK specifications [*Eyring et al.*, 2016] as closely as possible (see Appendix B: for details about input data). *piControl* spans a total of 500 years. Jan 1 of year 101 from *piControl* served as initial conditions for the idealized 1% yr^{-1} CO_2 increase (*1pctCO2*) and abrupt CO_2 quadrupling (*abrupt-4xCO2*) simulations, as well as the first member of the historical simulations (*historical_H1*). Subsequent members were branched every 50 years for a total of five ensemble members. AMIP simulations (prescribed SST) were also performed to cover the entire period for which CMIP6 provides surface boundary conditions (1870-2014). Atmosphere and land initial conditions for *amip_A1* were taken from year 1870 of *historical_H1*, and similarly for the other members.

The entire simulation campaign was performed on NERSC Edison. E3SMv1 did not experience any internal failures during the entire 2930 simulated years. The only failures were system related (generally node failures or file system issues) and the model could always be restarted from the last available set of annual restart files. The source code git hash for the *piControl* simulation was `2e145acf` (https://github.com/E3SM-Project/E3SM/commit/2e145acf) and for the remaining simulations was `7de18fc7` (https://github.com/E3SM-Project/E3SM/commit/7de18fc7). The difference in source code version arises from code modifications necessary to support transient simulations that were not in place when the *piControl* simulation was started. The newer `7de18fc7` code bit-for-bit (BFB) reproduces `2e145acf` for *piControl*. A maintenance branch (`maint-1.0`; https://github.com/E3SM-Project/E3SM/tree/maint-1.0) has also been specifically created to reproduce these simulations. BFB results on NERSC Edison will be maintained on that branch for as long as the computing environment supports it.

4 Pre-industrial control simulation

The pre-industrial control simulation (*piControl*) is in energy balance at TOA with an average loss of 0.011 W m^{-2} over the course of 500 years (tuning objective 1; Fig. 3a) and almost no long-term linear trend. Among all the model components, the ocean constitutes the largest reservoir of heat. It takes up heat at an average rate of 0.016 W m^{-2}, leaving a small net imbalance of 0.027 W m^{-2}, either from changes in other components or energy non-conservation. Since this imbalance is sufficiently small compared to anthropogenic forcings of interest, E3SMv1 can be regarded as essentially conserving energy. We note however that developmental versions of E3SMv1 suffered from much larger imbalances (on the order of 0.5 W m^{-2}). That imbalance was caused by inconsistent definitions of energy in the ocean and the atmosphere, with the ocean properly accounting for changes in water heat content with temperature while the atmosphere did not. The 0.5 W m^{-2} imbalance was deemed too large to ignore, but rewriting the atmosphere physics more consistently was impractical due to time constraints. As a result, we decided to incorporate an *ad hoc* correction term. An additional surface (sensible heat) source is introduced to the atmosphere that accounts for the missing energy carried by water molecules leaving the ocean at one temperature, and returning (as condensed water) at another temperature.

The apparent flux is small (0.4 W m^{-2}), and applied uniformly at every point globally. The correction doesn't impact the simulated climatology, but its neglect would had led to a long term drift in the global mean temperature of a few tens of degree by century. With this correction, both atmosphere and ocean communicate consistent energy loss and gain with each other (see Appendix A: for more detail).

The global mean surface air temperature is very stable over the course of the control simulation (tuning objective 2; Fig. 3b). There is a slight positive temperature trend of +0.013°C/century over the entire 500 years, and a much smaller trend of -0.003 °C/century over the last 400 years. We note that all additional simulations were branched from *piControl* in year 101 or later (Table 2), thus ensuring that forcing perturbations are applied atop a non-drifting control simulation. This facilitates subsequent analyses, since it is not necessary to correct for a long term drift in the underlying control. Another measure of the stability of the climate in the *piControl* simulation is provided by the annual maximum and minimum sea ice area in Arctic and Antarctic (Fig. 3c). Both hemispheres have little long term drift in their seasonal cycle of sea ice extent.

Among 42 CMIP5 models analyzed by *Hawkins and Sutton* [2016], a majority of them have pre-industrial global mean surface temperatures between 13 and 14°C, with some as low at 12°C and as high as 15°C. With a long-term average surface temperature of 13.8°C, E3SMv1 falls within the range of the bulk of CMIP5 models (tuning objective 3). This value is also consistent with estimated warming and the present-day global temperature of 14.0±0.5°C by *Jones et al.* [1999] for the period 1961-1990 and with leading re-analyses datasets (14.3 to 14.6°C) for the period 1979-2008 [*Hawkins and Sutton*, 2016].

Water conservation is also important for a global Earth system model. During the early development of the E3SMv1 model, we identified a number of computational problems, leading to water conservation errors in the atmosphere component [*Zhang et al.*, 2018]. These problems were all considered, and suitable remedies applied (e.g., borrowing from adjacent cells to avoid more drastic non-conservative fixers) so that in the 500 year *piControl* simulation, the relative water conservation error (as defined in *Zhang et al.* [2018]) in the atmosphere component is about 0.00226%, equivalent to a computational sea level rise of about 2 mm $century^{-1}$.

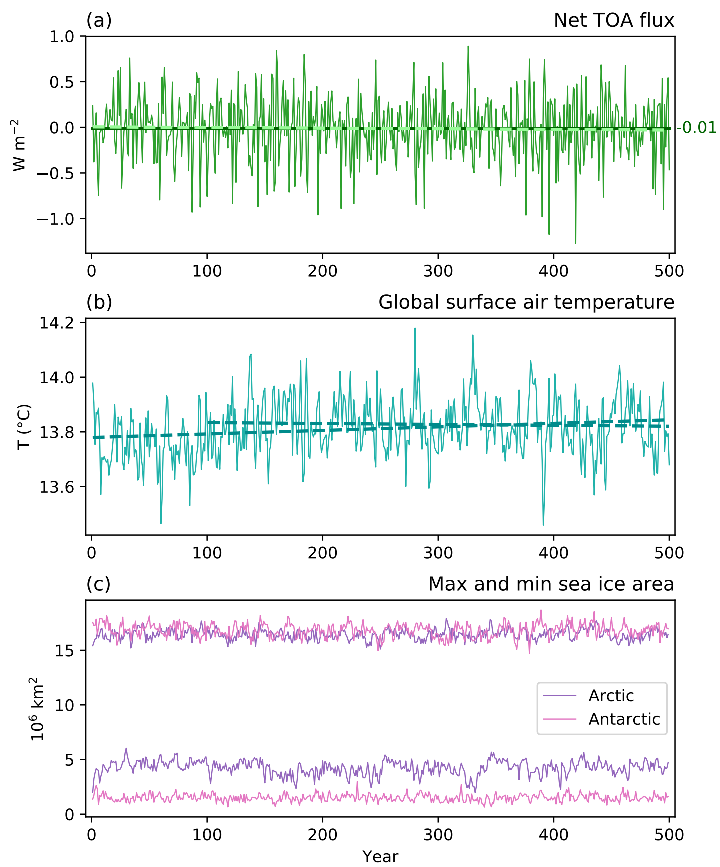

536 **Figure 3.** Time evolution of annual (a) global mean net TOA radiation (positive down), (b) global mean surface air temperature, and (c) maximum and minimum of total sea ice area for the Arctic and Antarctic in the *piControl* simulation. Dashed lines in (a) and (b) represent linear trends. The solid straight line in (a) is the mean TOA energy imbalance of -0.011 W m^{-2}.

Additional problems were also identified in the fully coupled system, including non-conservation caused by inconsistent remapping in the exchange of water between model components, excessive storage capacity in the river routing model, missing perched drainage and ponding in the land surface model, and grid definition inconsistencies between different model components. Some of these errors caused non-conservation errors in sea level rise as large as tens of meters per century but all were resolved and corrected. Unfortunately, a smaller non-conservation error was not uncovered until after E3SMv1 was frozen and the DECK simulations were complete. It manifests itself by a steady loss of water in the ocean of 5 cm century^{-1} in the *piControl* simulation. We note that the water loss does not involve any phase change and therefore does not impact TOA energy balance; however, it does impact ocean heat content. The root cause has since been traced to a nonphysical update of water stored in the unconfined aquifer of urban subgrid land units within the land model. This error, which has been corrected for future versions of E3SM (https://github.com/E3SM-Project/E3SM/pull/2603), was partly masked by incomplete and inconsistent water budget checks within the land model and the coupler. These budgets have also been corrected.

5 Historical simulations

5.1 Atmosphere climatology

We first evaluate the atmosphere in E3SMv1 with climatologies from the final 30 years (1985-2014) of simulations. Five ensemble members of the historical coupled experiment (H1 to H5) and three ensemble member AMIP simulations (A1 to A3) are evaluated. Similar figures are presented in *Rasch et al.* [2019] with comparisons to CAM5.

The net TOA radiative flux (positive down) is shown in Figure 4 compared to CERES-EBAF Ed4.0 [*Loeb et al.*, 2009]. Bias patterns are qualitatively similar between the atmosphere and coupled simulations, indicating a strong imprinting of atmosphere biases on the coupled system, but the biases are frequently larger in the coupled simulations, where component interactions play a role (RMSE of 9.13 vs 7.80 W m^{-2}). Significant positive biases are seen in the subtropical stratocumulus regions off the west coasts of North America, South America and Africa due to an underestimate of cloudiness. The under-predicted coastal stratocumulus is due to both the use of CLUBB and model re-tuning *Xie et al.* [2018]. Southern Oceans are also marked by positive biases due to clouds. The remaining oceanic regions have either neutral or negative biases. Tropical land masses have generally positive biases, while northern high latitudes suffer from negative ones. The global mean net flux is +0.32 W m^{-2} for the coupled simulations and +0.15 W m^{-2} for the AMIP simulations, both slightly smaller than the observational estimates of 0.6 W m^{-2} from CERES-EBAF Ed 4.0. [uncertainty range of 0.2 to 1.0; *Wild et al.*, 2012]. We note that the present-day energy imbalance was not a target of model tuning. Instead, we tuned the pre-industrial control simulation to have a net zero global mean TOA flux. The imbalance for 1985-2014 emerges from the model evolution in response to historical forcings in the case of the coupled simulations or as a result of imposing present-day SST and sea-ice concentrations (as boundary conditions) for the AMIP simulations.

Biases in cloud radiative effects (CRE) at TOA compared to CERES-EBAF Ed4.0 [*Loeb et al.*, 2009] are shown in Figure 5 for SW and LW. Many regional biases apparent in net TOA (Fig. 4) can be traced to SW cloud biases. LW CRE reveal additional biases, such as a lack of LW cloud trapping in the tropics from high clouds and excessive LW trapping from northern high latitudes clouds. As indicated in *Xie et al.* [2018], high clouds are significantly reduced in the tropical deep convection regions due to the increase of model vertical resolution from 30 levels to 72 levels in EAM, which results in a much weaker LW CRE over these regions. Global mean CRE for both SW and LW are approximately 3 W m^{-2} below the observational estimates.

Annual precipitation is depicted in Figure 6 compared to GPCP v2.2 [*Adler et al.*, 2003; *Huffman et al.*, 2009]. Simulated global mean precipitation is slightly above 3 mm day^{-1} for both AMIP and coupled simulations, approximately 15% larger than the GPCP estimate. A comprehensive review of 30 currently available global precipitation data sets found large differences in the magnitude of global land annual precipitation estimates [*Sun et al.*, 2018]. In their estimate of the global energy cycle, *Wild et al.* [2012] note that the GPCP estimate may be too low due to systematic underestimations in the satellite retrievals [*Trenberth et al.*, 2009; *Stephens et al.*, 2012]. *Wild et al.* [2012] estimated the global mean precipitation at 2.94±0.17 mm day^{-1} while the estimate from *Stephens et al.* [2012] is 3.04±0.35 mm day^{-1}. The global mean precipitation from E3SMv1 falls within both estimates.

Major regional precipitation biases in AMIP simulations (Fig. 6b) include a dry Amazon, excessive precipitation over elevated terrain (e.g. Andes, Tibetan plateau), wet

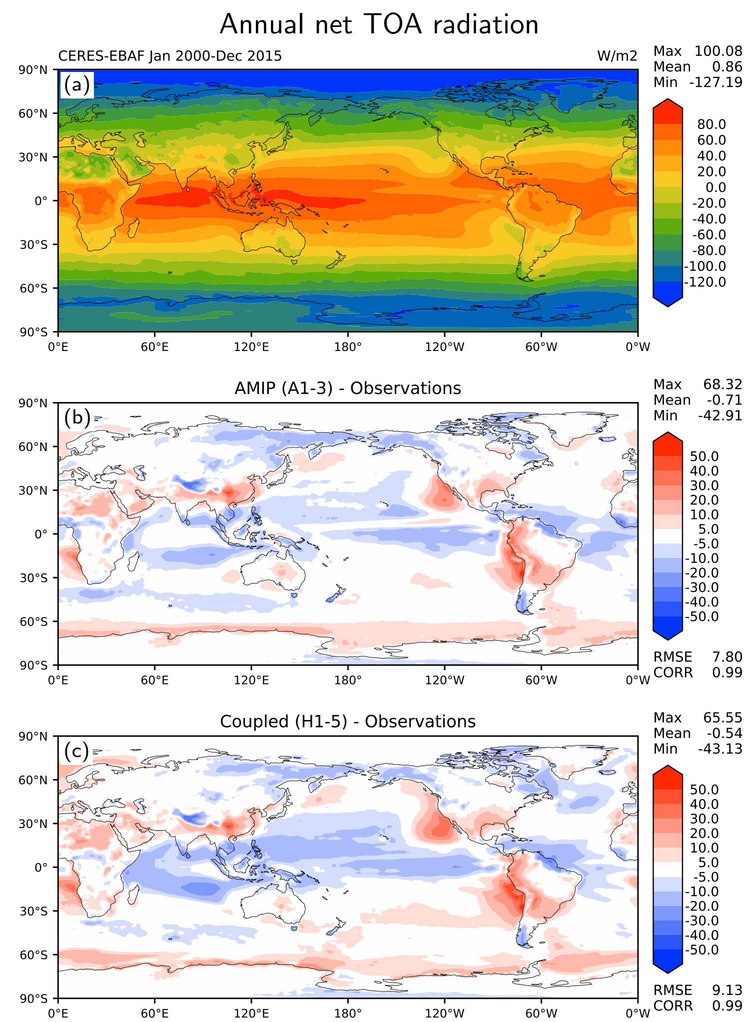

589 **Figure 4.** Annual net top-of-atmosphere (TOA) radiative flux: (a) CERES-EBAF Ed4.0 observational estimate, (b) model bias from the three AMIP ensemble simulations and (c) model bias from the five ensemble historical coupled simulations (1985-2014).

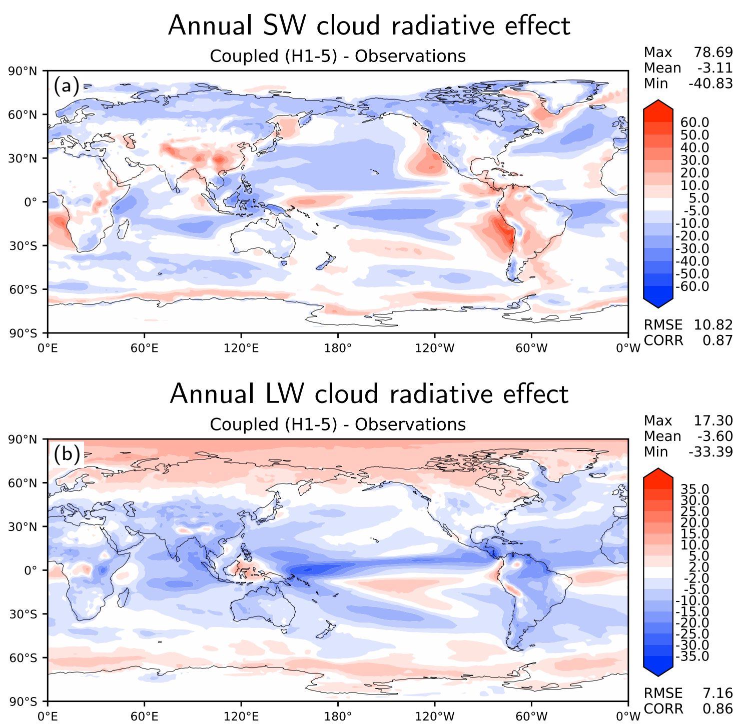

Figure 5. Annual top-of-atmosphere cloud radiative effect model biases (W m^{-2}) of the five ensemble historical simulations (1985-2014) against CERES-EBAF Ed4.0: (a) SW and (b) LW.

biases over tropical Africa and the Indian ocean, and a dry bias over the central US (traced to the Summer time). Coupled simulations (Fig. 6c) tend to amplify regional biases present in AMIP simulations (except the central US), as well as develop biases typical of coupled simulations: double ITCZ and excessive precipitation over the maritime continent. Unsurprisingly, the RMSE error increases from 0.93 to 1.13 mm day^{-1} and the correlation decreases (0.93 vs 0.86) between AMIP and coupled simulations.

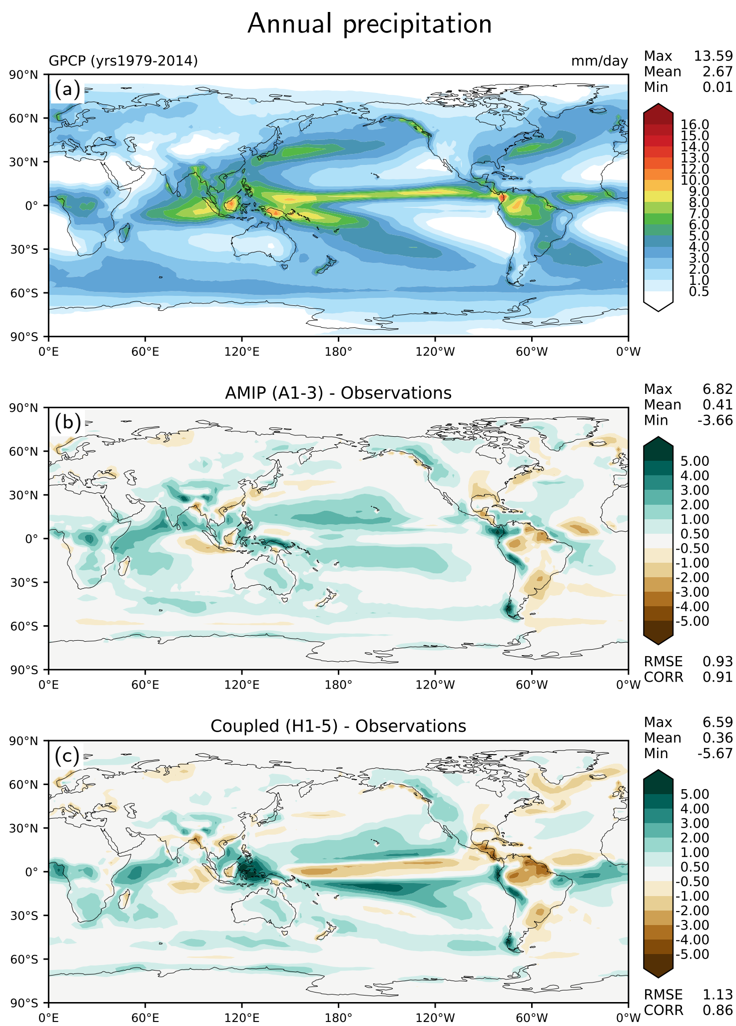

Figure 6. Annual precipitation rate: (a) GPCP v2.2 observational estimate, (b) model bias from the three AMIP ensemble simulations and (c) model bias from the five ensemble historical coupled simulations (1985-2014).

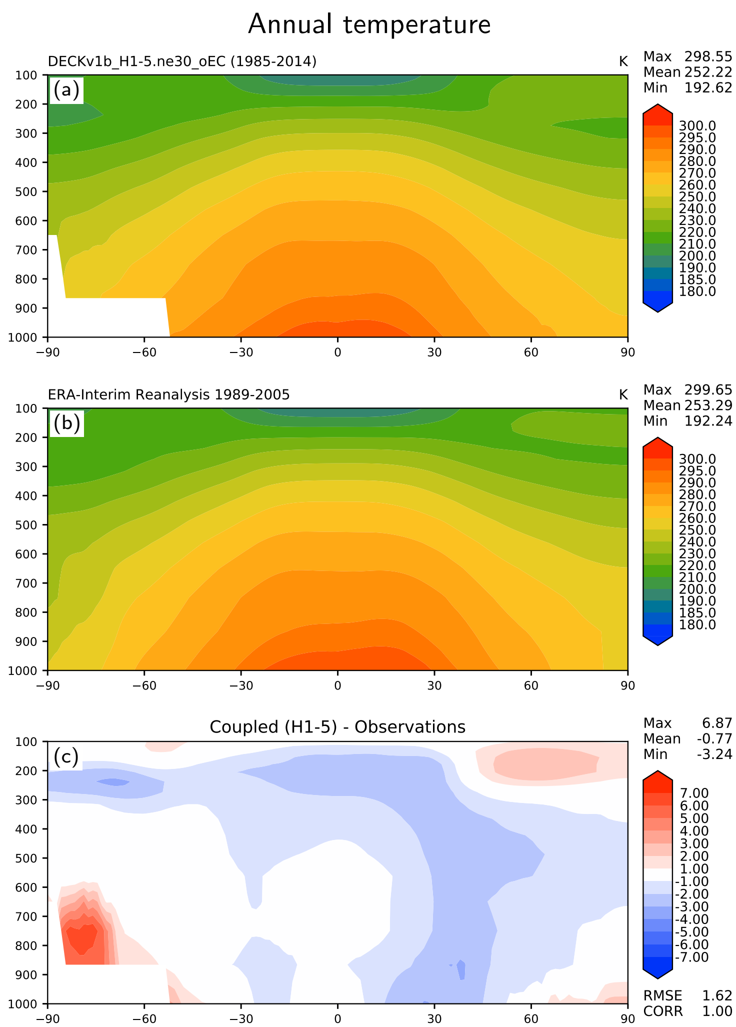

Figure 7. Annual zonally averaged temperature: (a) ensemble mean of historical coupled simulations (1985-2014), (b) ERA-Interim reanalysis, (c) model bias.

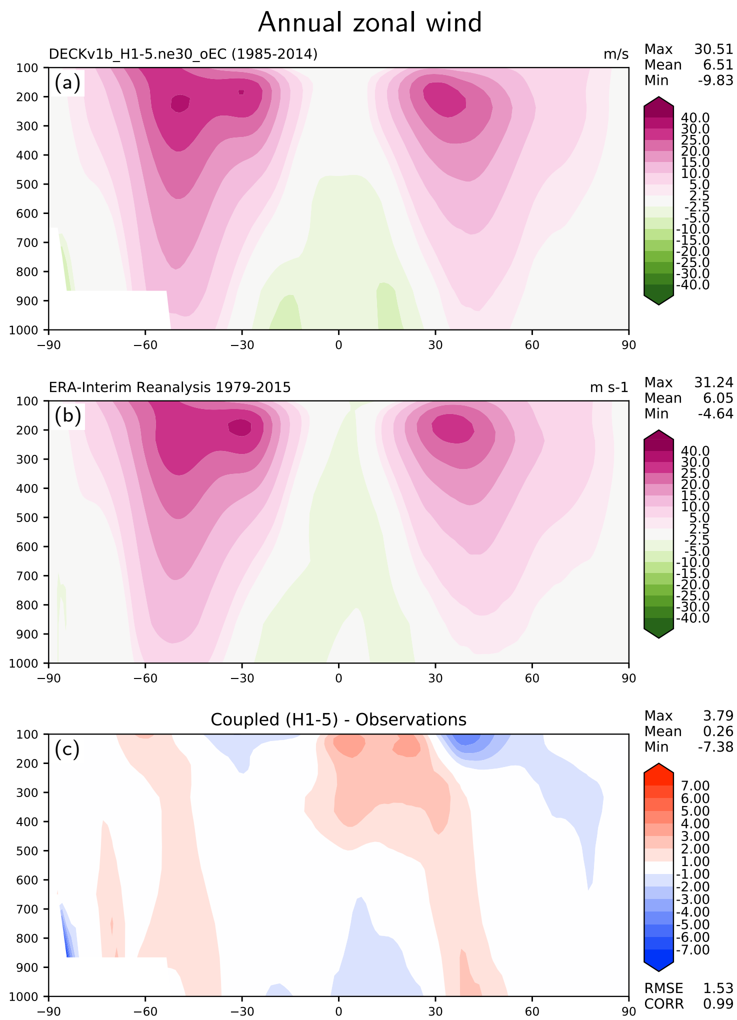

Figure 8. Annual zonally averaged zonal wind: (a) ensemble mean of historical coupled simulations (1985-2014), (b) ERA-Interim reanalysis, (c) model bias.

Figure 7 shows the annual, zonally averaged temperature for the coupled simulations compared to ERA-Interim reanalysis [*Dee et al.*, 2011]. Overall, the model captures the thermal structure of the atmosphere. There is a tropical cold bias in the upper troposphere which correlates with insufficient tropical high clouds (Fig. 5b). In the northern mid-latitudes, the cold bias extends to the surface because of the colder than observed northern latitudes SSTs (see Section 5.2 below). There is also a significant warm bias in the lower portion of the troposphere in the southern high latitudes. The corresponding zonal wind is shown in Figure 8. The locations of the maximum jet locations are displaced equatorward and the wind magnitude is also too large throughout the mid-latitude troposphere. Tropical easterlies are too weak in the upper troposphere and too strong near the surface.

The evaluation above provides only a limited view of the performance of E3SMv1 from an atmospheric perspective. For a more exhaustive evaluation, we turn to a comparison with an ensemble of 45 CMIP5 models using metrics computed with the PCMDI Metrics Package [PMP; *Gleckler et al.*, 2016, 2008]. The comparison covers the period 1981-2005 of the historical simulations. The historical and AMIP ensemble members of E3SMv1 were also processed with PMP. Figure 9 shows global RMSE for the CMIP5 ensemble using box and whiskers plot, as well as the individual E3SMv1 historical simulations with blue dots and AMIP with red dots. Spatial RMSE against observations collected by PMP are shown for nine fields, and each one of them for annual and seasonal averages. Lower values are better. For TOA radiation fields (Fig. 9a-c), E3SMv1 coupled (blue) generally falls within the lowest (best) quartile, and is even competitive with some of the best CMIP5 models for certain fields and seasons. We note that we are comparing a newer model against older ones, so we do not expect this to necessarily hold for CMIP6. For surface variables, precipitation (Fig. 9d), surface air temperature over land (Fig. 9e), and zonal wind stress over ocean (Fig. 9f), E3SMv1's coupled performance is better than the ensemble median and often falls within the lowest quartile, with the exception of surface air temperature over land during DJF and MAM. Precipitation during MAM is also notably worse than other seasons relative to the CMIP5 ensemble. For dynamical variables, zonal wind at 200 and 850 hPa (Fig. 9g-h) and 500 hPa geopotential height (Fig. 9i), E3SMv1 is generally better than the CMIP5 median, except again for MAM.

Unsurprisingly, AMIP simulations (red) perform better than their coupled counterparts (blue). However, the relative degradation between AMIP and coupled helps attribute sources of errors. For example, the difference is relatively small for the zonal mean wind, and thus improving overall performance would likely require atmospheric improvements. On the other hand, surface variables, in particular precipitation and temperature, are much more strongly affected by the coupled model errors that emerge. The MAM seasonal deficiency also appears to be rooted in coupling errors.

In summary, E3SMv1 performs better than the median of the of CMIP5 ensemble for most atmospheric fields and seasons, which helps establish the credibility of the E3SMv1 simulated climate.

cmip5.pdf

Figure 9. Comparison of RMSE (1981-2005) of an ensemble of 45 CMIP5 models (box and whiskers showing 25th and 75 percentiles, minimum and maximum) with the five E3SMv1 historical members (blue dots) and the first member of the AMIP simulations (ret dots). Spatial RMSE against observations are computed for annual and sesonal averages with the PCMDI Metrics Package [*Gleckler et al.*, 2016]. Fields shown include TOA net radiation (a), TOA SW and LW cloud radiative effects (b,c), precipitation (d), surface air temperature over land (e), zonal wind stress over ocean (f), 200 and 850 hPa zonal wind (g,h) and 500 hPa geopotential height (i).

5.2 Ocean climatology

An annual climatology (1985-2014) of the E3SMv1 ensemble mean of sea surface temperature (SST) is shown in Figure 10, compared to the Hadley-NOAA/OI merged data product [*Hurrell et al.*, 2008] averaged over the same period. Overall, E3SMv1 captures the observed SST well, with an ensemble mean bias of 0.093°C and an ensemble mean RMSE of 0.939°C. A few biases do emerge. First, there is a cold bias in the North Atlantic associated with excessive sea ice in the Labrador Sea. Consistent with this sea ice bias, these cold SST biases are stronger in the first half of the year than in the second half (not shown). While the exact cause of the Labrador Sea ice bias is unknown, it is likely that missing critical heat transports (*e.g.*, from the East and West Greenland currents, Irminger current, and the Northwest corner), perhaps from low resolution or excessive horizontal viscosity [*Jochum et al.*, 2008] play an important role. Second, there are warm biases on the eastern sides of ocean basins, coincident with SW CRE biases discussed in sec. 5.1. Finally, the Southern Ocean is also ≈ 2°C warmer than observed. It is possible this last bias is associated with the relatively large value for the Gent-McWilliams bolus coefficient used, which was chosen to prevent excess heat transport to the deep ocean (see sec. 2.2).

The E3SMv1 sea surface salinity (SSS) bias is shown in Fig. 11. The model output is compared to the 2011-2014 NASA-Aquarius data [*Lagerloef et al.*, 2015]. Overall the surface ocean is too fresh, with the largest bias in the Labrador Sea. The two minor exceptions to this pattern are the positive salinity bias region over the west Pacific warm pool, which is coincident with the atmospheric precipitation maximum being shifted westward relative to observations (Fig. 6) and a positive salinity bias in the Arctic.

The ensemble average Mixed Layer Depth (MLD) annual climatology, based on a critical density threshold (σ_c = 0.03 kg m^{-3}), is presented in Figure 12. The model output is compared to data described by *Holte et al.* [2017]. The globally averaged model MLD is too shallow relative to observations, with the largest bias coincident with the large fresh bias in the North Atlantic. Unlike many other CMIP5 models [*e.g.*, *Sallée et al.*, 2013], the E3SMv1 MLD in the Southern ocean is slightly deeper than observed. This is due to the region of deeper mixed layers in E3SMv1 being broader than observed (Fig. 12a), possibly due to a positive bias in the Southern Ocean wind stress. The maximum MLD simulated by E3SMv1 is still much shallower than observations, which is consistent with other CMIP5 models.

Figure 13 shows the E3SMv1 maximum Atlantic Meridional Overturning Circulation (AMOC) at 26°N, the site of the RAPID array [*Smeed et al.*, 2017]. The mean AMOC simulated in the historical ensemble (approximately 11 Sv) is weaker than the observed mean (16.9 ± 3.35 Sv) and also on the weak end of CMIP model AMOC strength (*e.g.*, *Cheng et al.*, 2013 their Fig. 1). There are a number of possible causes for the weak AMOC in E3SMv1. Currently, MPAS-Ocean utilizes a z-star coordinate [*Adcroft and Campin*, 2004], which is broadly consistent with a traditional z-level coordinate in the deeper ocean. Z-coordinate models are known to experience spurious diapycnal mixing [*e.g.*, *Griffies et al.*, 2000], which could reduce AMOC strength. Second, recent work has shown that Nordic overflows [*Wang et al.*, 2015] and Arctic Freshwater transports [*Wang et al.*, 2018] have a strong impact on AMOC. At low resolution, these processes are poorly

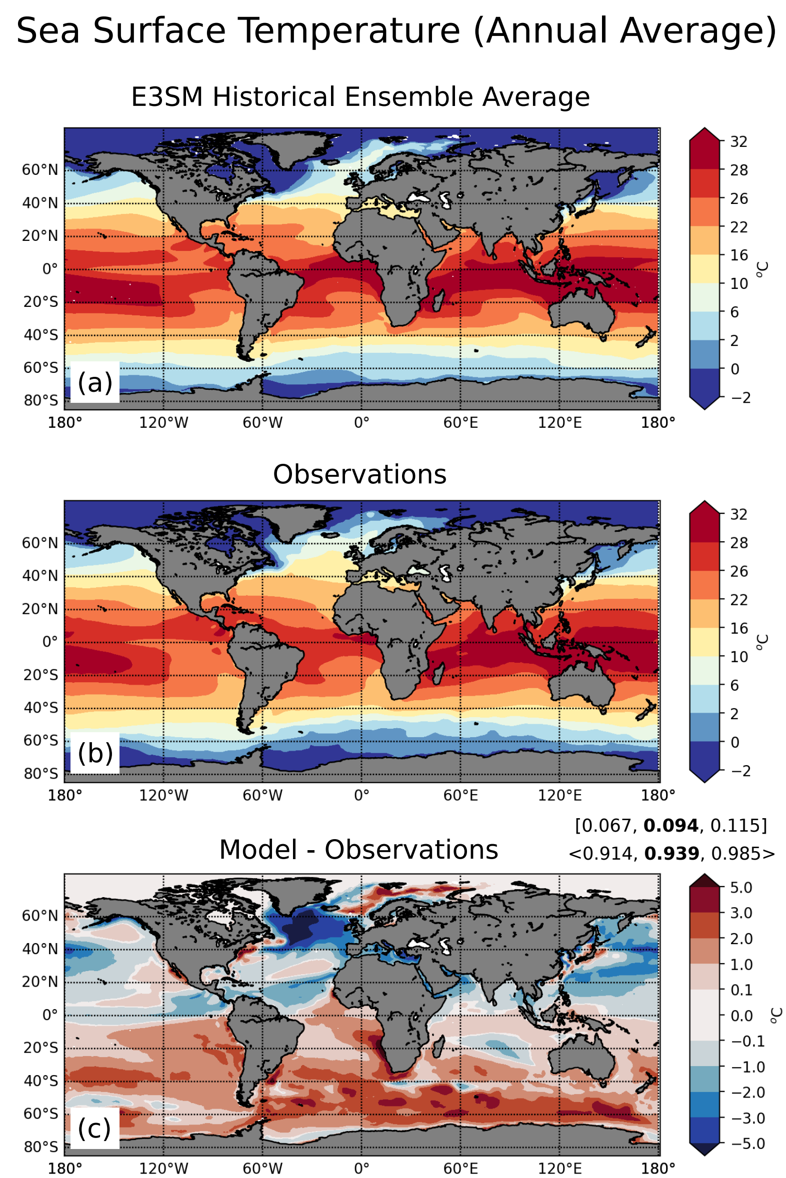

Figure 10. Annually averaged SST climatology (1985-2014) for (a) E3SMv1 historical simulation (ensemble mean), (b) Hadley-NOAA/OI merged SST dataset (1985-2014; [*Hurrell et al.*, 2008]), and (c) Model bias. In the upper right corner of panel (c), the mean bias is shown in square brackets and the RMS error is in angular brackets. For each error, the min, **mean**, max is listed for the historical ensemble.

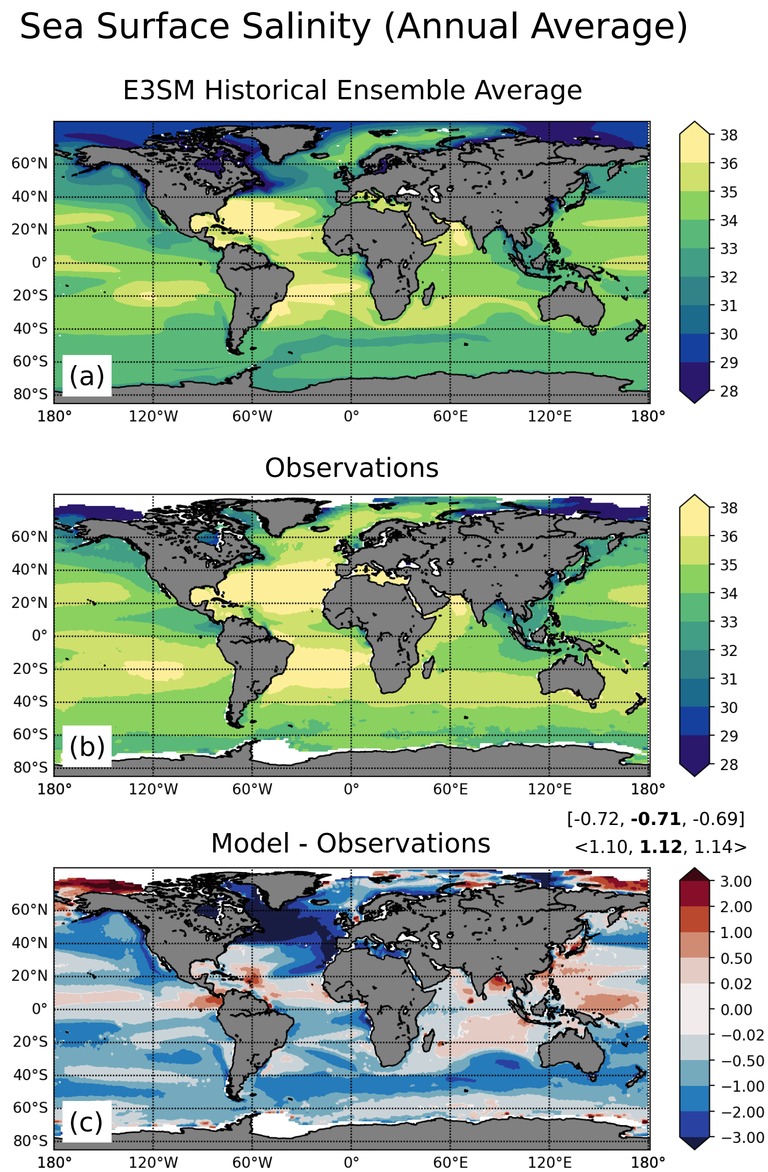

704 **Figure 11.** As in Figure 10 but for Sea Surface Salinity (PSU). The dataset in (b) is from NASA Aquarius
705 data (averaged 2011-2014).

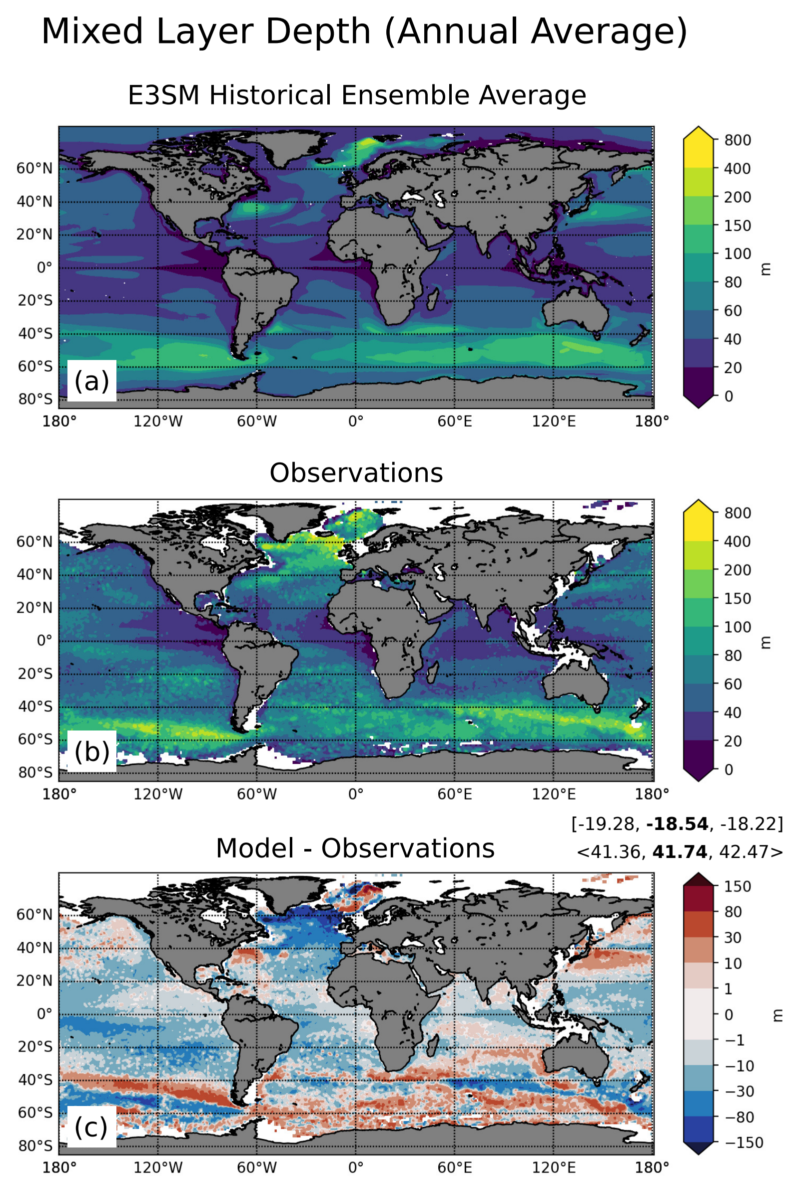

Figure 12. As in Figure 10 but for the annual average mixed layer depth. The data in (b) is from *Holte et al.* [2017]. Data has been averaged from 2001-2017.

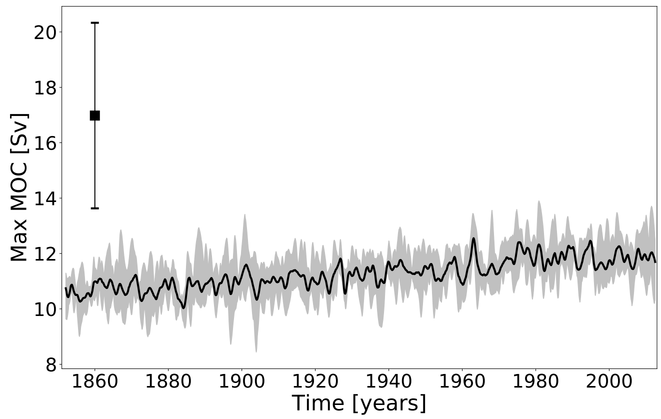

Figure 13. Annually averaged maximum Atlantic Meridional Overturning Circulation at 26.5°N below 500m depth. The solid black line represents the ensemble mean and the spread of the shaded gray region represents the maximum and minimum of the ensemble. The observed AMOC and standard deviation at the RAPID array is shown by the vertical bar (16.9 ± 3.35Sv.)

represented, where the latter is likely too strong as critical passageways being too wide (e.g. Davis Strait). Finally, since E3SMv1 exhibits excess sea ice in the Labrador sea, the simulated MLD (Fig. 12) is reduced, which reduces deep convection and hence AMOC strength.

5.3 Sea ice

Sea ice in E3SMv1 is too extensive at the end of winter and too confined in late summer, reflecting a heightened model seasonality relative to both the Arctic and Southern Ocean passive microwave record, regardless of the algorithm used to derive ice area from these retrievals [e.g., *Cavalieri et al.*, 1996; *Meier et al.*, 2017]. This result is summarized in Figures 14, 15, and 16. Embedded within this heightened seasonality, the melt-season minimum is delayed in the Northern Hemisphere relative to observations. In the high north, the heightened winter seasonal extent relative to observations occurs mainly in the Labrador Sea, as well as the Iceland Sea and Pacific margin of the Sea of Okhotsk, evident in the historical 5-member ensemble means (Figs. 14a and 14b). Comparison with satellite-derived albedo, shown for June to August in Figure 17, suggests that surface radiative processes leading to an albedo bias in the central arctic are unrelated to the physical exchanges responsible for the Labrador sea bias. As a result, the Labrador Sea bias is unlikely to be attributable to MPAS-Seaice alone, and is more likely a result of coupled interactions and unresolved heat advection in the region.

The model possesses a negative climatological trend in Arctic sea ice thickness that is qualitatively consistent with observed basin-wide trends [e.g., *Kwok and Rothrock*, 2009], as quantified in Figure 14. The 1980-1999 hemispheric mean spread among the five ensemble members for March (September) decreases from 1.5-1.71 m to 1.16-1.37 m (1.55-2.12 m to 0.79-1.35 m) for the period 2000-2014, which includes the thinnest periods known in the Arctic sea ice thickness record. Still, the spatial ice thickness pattern in the central Arctic does not reflect the predominant build-up of thick ice against the Canadian Archipelago seen in observational estimates, including those of *Bourke and McLaren* [1992], *Kwok and Cunningham* [2008], and *Tilling et al.* [2015]. This represents a second sea ice bias being addressed in ongoing improvements to the polar components of E3SM. There is no significant climatological trend in mean Southern Ocean sea ice thickness from the historical simulations, in the ensemble mean or spread (Fig. 15). Extent bias stemming from the heightened polar seasonality of E3SMv1 is consistent across our chosen 1980-1999 and 2000-2014 analysis periods, seen in Figure 15. While the model does not replicate the observed climatological trend in austral sea ice extent (Fig. 16), it does simulate the critical decrease in Northern Hemisphere minimum sea ice extent, which has had a significant impact on planetary albedo in the current century and is therefore an important contribution to the energy balance of E3SMv1 as a whole.

5.4 Land and river

Figure 18 shows a comparison of the mean annual total (surface and subsurface) runoff simulated by ELM with the composite runoff map from the Global Runoff Data Center (GRDC) [*Fekete and Vörösmarty*, 2011]. Since the GRDC data only provides monthly runoff for 1986-1995, the comparison is shown for the annual total runoff averaged over the same period of the *historical_H1* simulation. ELM captures the general spatial distribution of the GRDC runoff, but in relatively arid regions such as Australia and the western U.S., ELM has wet biases, while in the Amazon tropical forest, dry biases are notable. These biases are consistent with the precipitation deficiencies shown in Figure 6.

The seasonal cycle of streamflow is an important metric of water availability, as water deficits resulting from a mismatch in the timing of water supply and water demand

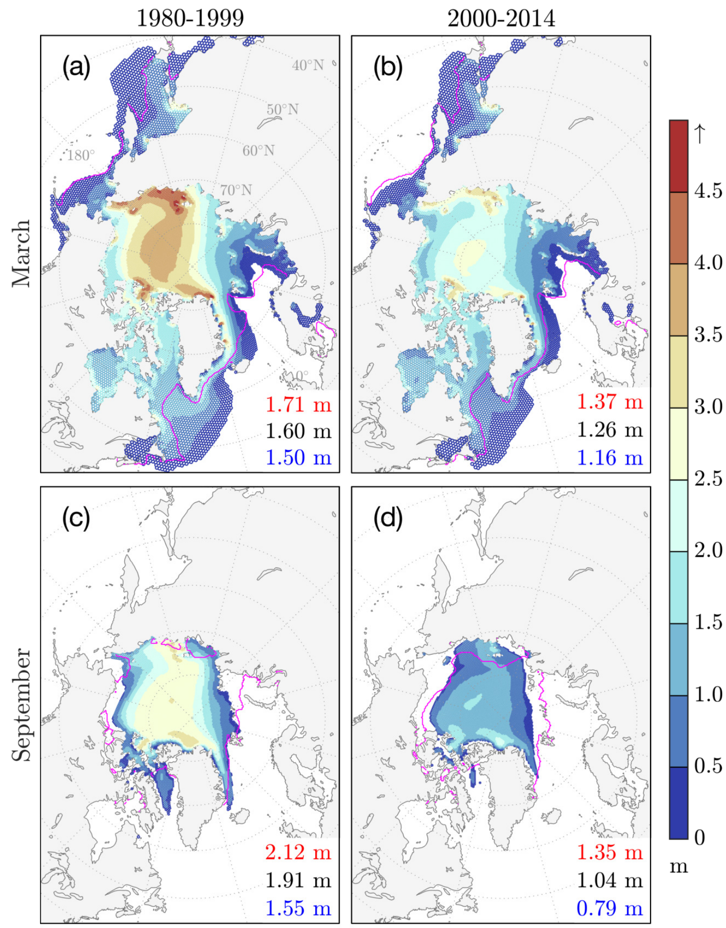

Figure 14. Northern hemisphere ensemble mean March and September sea ice thickness for two decades leading up to year 2000 (a and c), and the first 15 years of the 21st century (b and d). Model ice thickness is truncated at 15% concentration, and magenta represents the *Meier et al.* [2017] NOAA Climate Data Record (CDR) ice extent for the same averaging periods. Grid density on the polar stereographic projection is indicated by cell translucence. Numbers in the lower right corner of each panel indicate the mean hemispheric ice thickness thickness for the thinnest ensemble member (blue), the multi-ensemble mean rendered in the map (black), and the thickest ensemble member (red) for the each period.

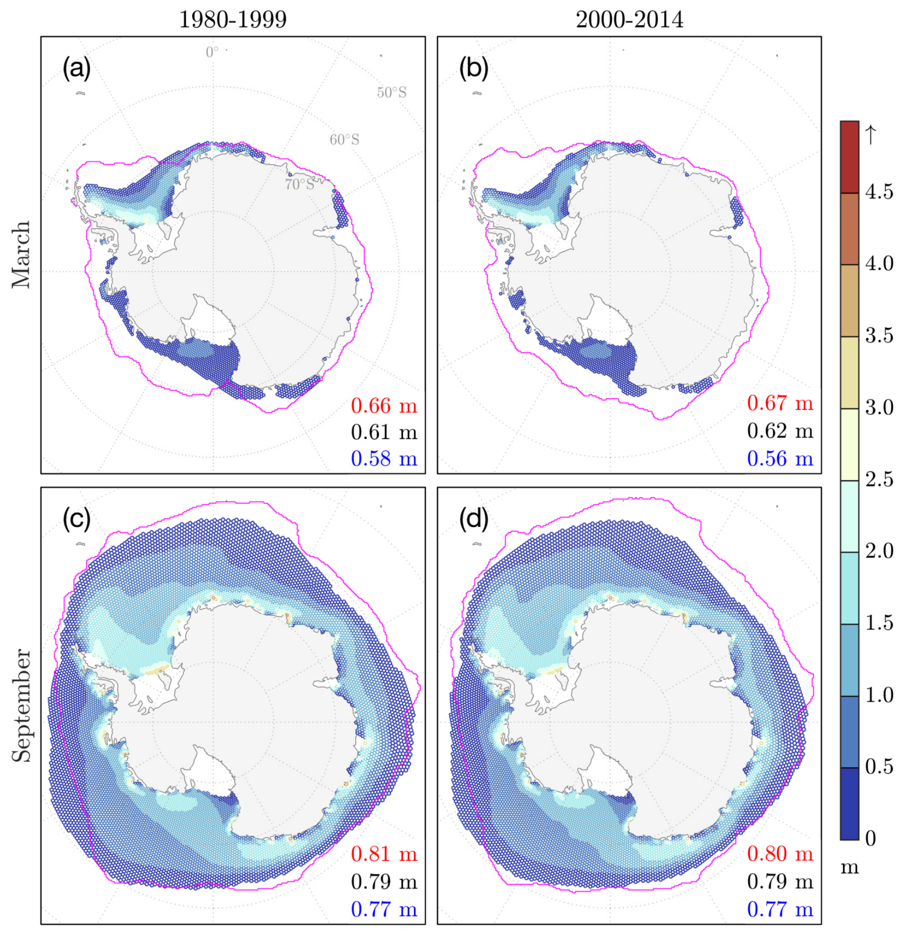

777 **Figure 15.** As for figure 14, but for the southern hemisphere.

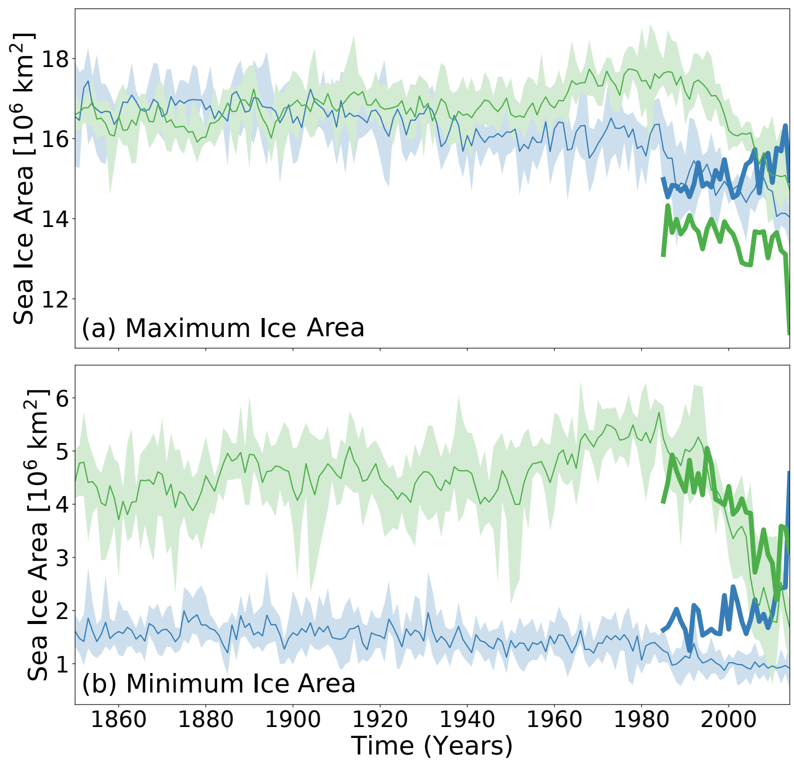

Figure 16. Maximum (a) and Minimum (b) Sea ice area observed during the year for the Northern (green) and Southern hemispheres (blue). The shaded bounds represent the E3SMv1 historical ensemble spread, and the thick colored lines are NASA TEAM observations [*Cavalieri et al.*, 1996]. Model and observational data are monthly averages.

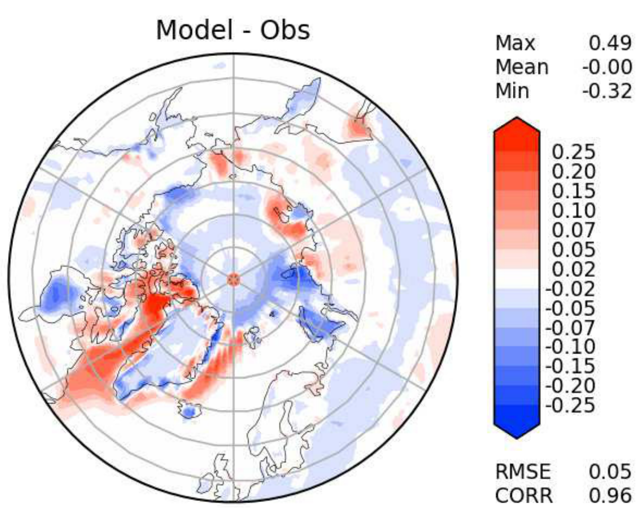

Figure 17. Surface albedo bias (E3SMv1 - CERES-EBAF) for northern hemisphere spring, averaged over 1985-2014

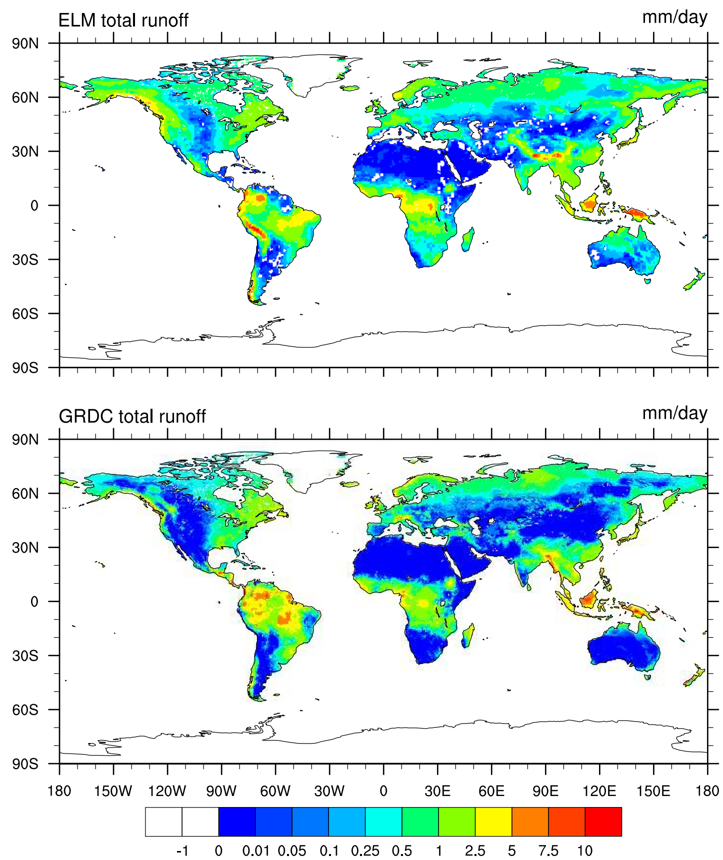

Figure 18. Mean annual total runoff (in mm/day) simulated by ELM (upper panel) and from GRDC (lower panel) averaged between 1986 and 1995.

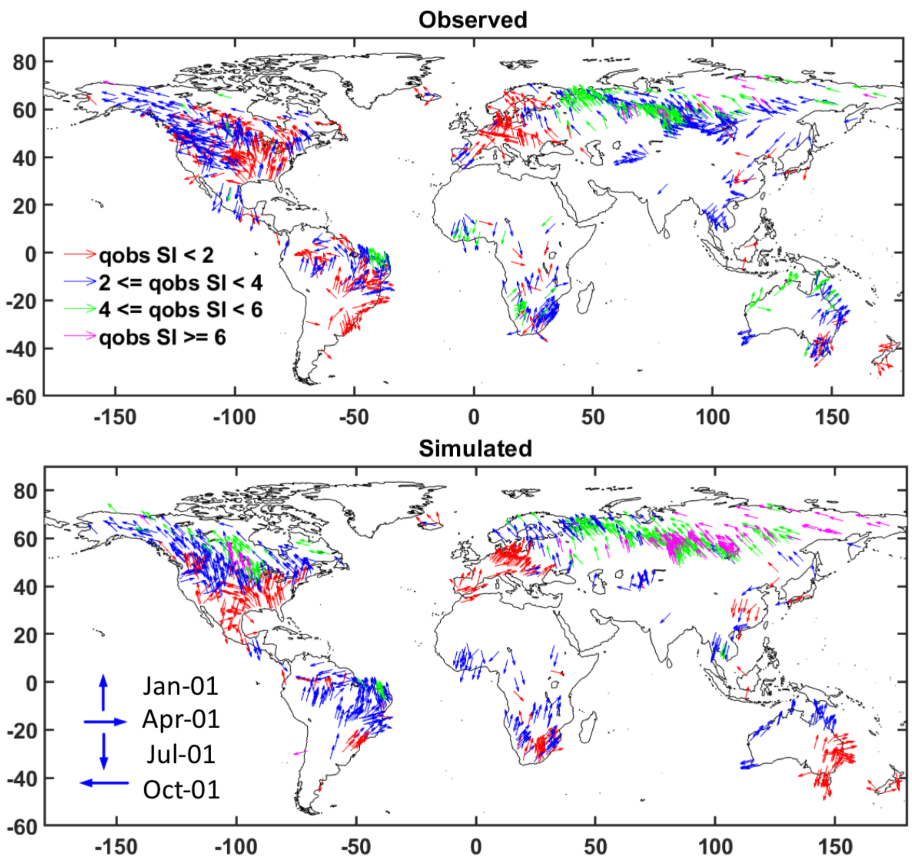

Figure 19. Seasonality of observed (upper) and simulated (lower) streamflow at stream gauge stations in major river basins around the world. The magnitude of seasonality indicated by the seasonality index (SI) is shown in color and the timing of the peak streamflow is shown by the position of the arrows. SI is calculated based on monthly streamflow between 1986 and 1995.

have important implications for energy and water. Figure 19 compares the seasonal cycle of simulated and observed streamflow at stream gauge stations in major river basins around the world. A seasonality index (SI) is defined as follows:

$$Pk_i = \frac{12}{n} \sum_{j=1}^{n} \frac{Q_{ij}}{\sum_{i=1}^{12} Q_{ij}} \tag{1}$$

$$SI = \max_i (Pk_i) \tag{2}$$

Where Q_{ij} is the monthly streamflow for month i and year j and n is the number of years in the simulation or observation. With this definition, SI is equal to 1 if the monthly streamflow is uniformly distributed throughout the year and SI is equal to 12 if streamflow only occurs in one month. The seasonality of the simulated streamflow is generally comparable with that observed in terms of both magnitude and timing. For example, in North America, streamflow seasonality is stronger in the Northwest with a peak timing between November and January but in the central and southeastern U.S., streamflow seasonality is weaker with a peak timing generally in spring. In Asia, streamflow generally peaks in the late summer. Larger biases in seasonality are found in Australia (Murray Darling River) and Central Asia (Yenisey) where biases in the runoff are also more significant (Figure 18).

5.5 Variability simulated by E3SMv1

In this section we present a variety of metrics to assess E3SMv1 variability.

The long term variability of the El Niño Southern Oscillation (ENSO), as simulated in the *piControl* and historical ensemble simulations is examined via wavelet analysis [*Torrence and Compo*, 1998] of Niño 3.4 SST and is shown in Figure 20. In this analysis, the *piControl* simulation is subdivided into five 100-year long sections (as in *Stevenson* [2012]). For reference, we also include the spectrum from HadISST [*Rayner et al.*, 2003] and ERSSTv4 [*Huang et al.*, 2015]. In both the *piControl* and historical ensemble, E3SMv1 ENSO variability is strong with statistically significant peaks near a three-year period. We also see a signature of longer term modulation of ENSO variability (6-9 year period) in the *piControl*. This is consistent with other CMIP models [*e.g.*, *Stevenson et al.*, 2012; *Stevenson*, 2012; *Wittenberg*, 2009] and proxy-data [*e.g.*, *McGregor et al.*, 2013]. However, the modulation is a bit weaker than other models. Relative to the CESMv1 Large Ensemble [*Kay et al.*, 2015], Figure 20b, where the CESMv1 PI control is subdi-

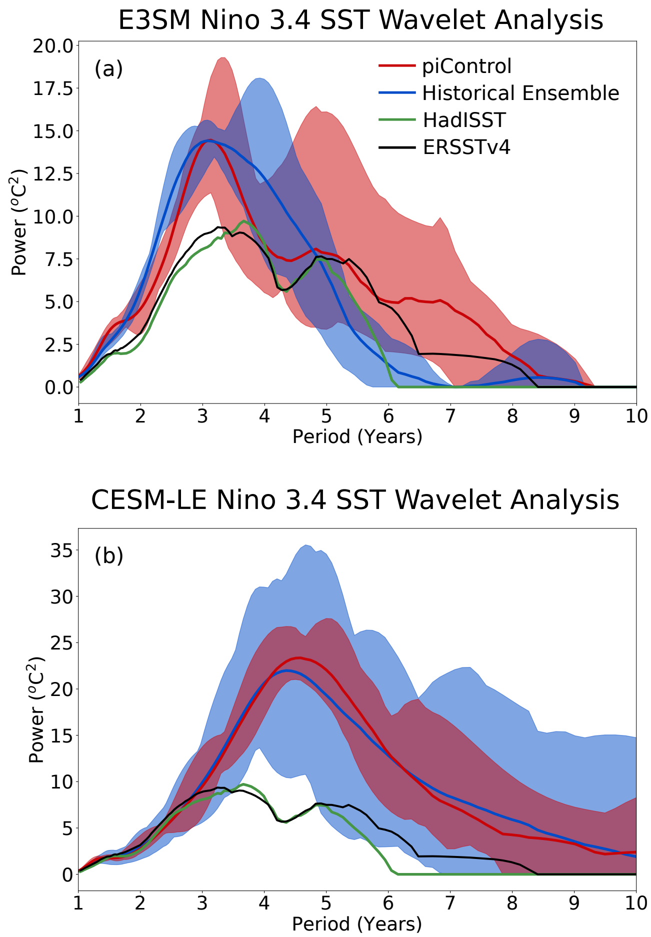

Figure 20. ENSO (Nino3.4) variability of the PI control simulation and historical ensemble. The Morlet wavelet of degree six is used [*e.g.*, *Torrence and Compo*, 1998] and the maximum and minimum wavelet power is used for each period. The PI control is subdivided into 100 year intervals to form a five member ensemble [*e.g.*, *Stevenson*, 2012]. The solid line represents the mean wavelet power for the ensemble. The shading bounds the maximum and minimum power that is above the 90% significance threshold. The black and green lines are two observational data products. (a) E3SMv1 and (b) CESM-LE.

vided as in E3SMv1, E3SMv1 variability is slightly closer to observations, but is shifted strongly to a three year period, whereas CESM-LE is dominant at approximately 4.5 years. In both models, the dominant ENSO peak remains consistent between the PI control and historical ensembles. We also note that the spread of ENSO variability in the E3SMv1 historical simulation is much smaller than in the CESM-LE. This is likely due to the small E3SMv1 ensemble size relative to the 39 member CESM-LE [*Newman et al.*, 2018].

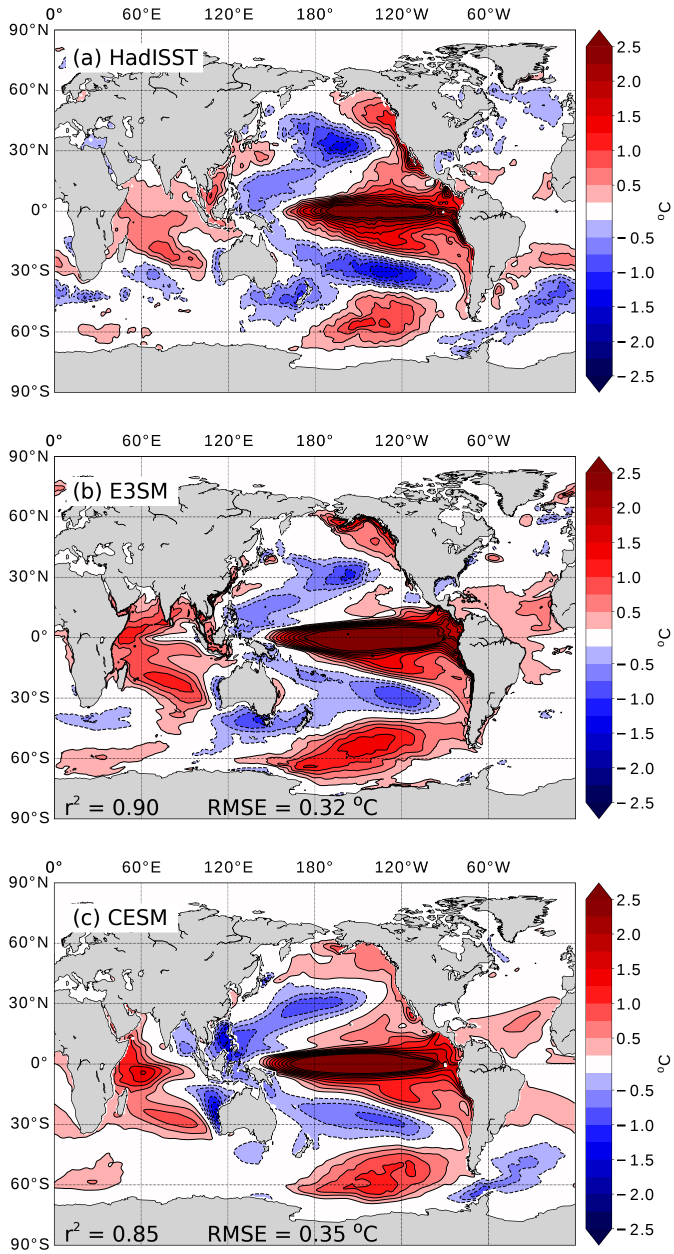

Figure 21. (a) - (c) Difference of composite El Nino events and composite La Nina events (1950-2015) for the HadleyISST dataset, the E3SMv1 historical ensemble, the CESM-LE respectively. El Nino events are defined as periods when the Nino 3.4 SST anomaly exceeds 0.8^{o}C for more than six consecutive months. The La Nina criterion is Nino 3.4 SST anomaly less then -0.8^{o}C for more than six months (these definitions are consistent with *Menary et al.* [2018]). When an ENSO event is identified, the SST is averaged from November - March. For model output, every ensemble member contributes to the mean composite. The Pearson correlation coefficient and RMSE are shown for E3SMv1 and CESM in (b) and (c).

A number of CMIP5 models do not well represent the spatial pattern of ENSO variability, in particular its westward extent [*e.g., Van Oldenborgh et al.*, 2005; *Menary et al.*, 2018]. Figure 21 shows the difference of a composite of the strongest El Niño events and strongest La Niña events (following [*Menary et al.*, 2018]). Broadly, E3SMv1 reproduces the spatial pattern seen in observations well with a few notable differences. E3SMv1 does not capture the signal along the North American coast, suggesting a bias in the coastally trapped kelvin waves. The westward extent is also larger than observed, but better than seen in CESM-LE. Overall, the comparison with observations is good, with low RMSE and a high correlation coefficient.

On sub-seasonal timescales the dominant mode of variability and predictability in the tropics is the Madden Julian Oscillation [MJO *Waliser et al.*, 2003]. The MJO is generally thought to play a role in ENSO initiation [*McPhaden et al.*, 2006], monsoon active break cycles [*Annamalai and Slingo*, 2001], tropical cyclogenesis [*Sobel and Maloney*, 2000] and remote teleconnection effects [*Vitart*, 2017], therefore its accurate simulation is key. The simulation of the MJO in E3SMv1 represents a significant improvement in strength, propagation characteristics and the explained intra-seasonal variance compared to CESM1 (Fig. 22). However, significant biases in Pacific propagation remain. In CESM1, the intra-seasonal propagation is in the wrong direction, westward, in the Indian Ocean. Weak correlations do make it over the Maritime Continent and into the West Pacific, but they are mostly decoupled from the SST signal. In contrast, E3SMv1 has consistent low-level wind propagation coupled in quadrature with the SSTs from the Indian Ocean to the Central Pacific.

5.6 Temperature evolution over the historical record

The 1850-2014 time evolution of the global mean surface air temperature anomaly from the E3SMv1 historical ensemble is compared against three observational products in Figure 23. Observations include NOAA NCDC [*Smith et al.*, 2008; *Zhang et al.*, 2015], NASA GISTEMP [*Hansen et al.*, 2010; *GISTEMP Team*, 2018], and HadCRUT4 [*Morice et al.*, 2012] which are in good agreement with each other. Anomalies are computed with respect to 1880-1909, the earliest 30-year period when data is available from all observational products. The E3SMv1 historical ensemble mean is shown in red and the ensemble minimum and maximum in orange shading. While E3SMv1 captures the bulk of the observed warming between the 1850s and 2010s, the trajectory of the warming is at times

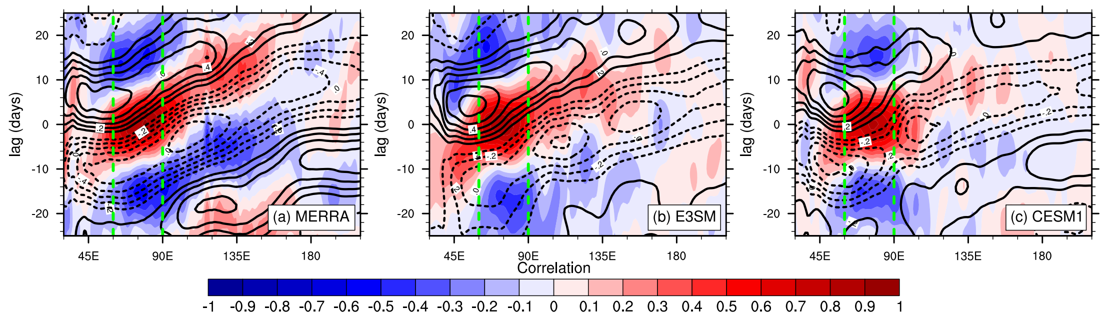

Figure 22. Tropical lag correlation (averaged 10°N-10°S) of precipitation (colors) and 850-mb zonal wind (lines) with precipitation in the Indian Ocean region (60°N-90°E; shown by the vertical dashed green lines) for (a) Observed (TRMM for precipitation MERRA for winds), (b) E3SMv1 pre-industrial control and (c) CESM pre-industrial control. Data used are daily anomalies and band-pass filtered between 20-100 days

inconsistent with observations. The ensemble overlaps with observations until the 1950s, but in the subsequent decades, E3SMv1 departs from observations, first remaining too cold for several decades before warming up too rapidly starting around year 2000. The low anomalies in E3SMv1 before 1960 result from a compensation between a downward trend in the Northern Hemisphere and a positive trend in the Southern Hemisphere (not shown).

We turn to a regional analysis to help elucidate this inconsistency. In Figure 24 we decompose the SST anomalies into two regions: the Northern and Southern Hemisphere. The E3SMv1 ensemble range is shaded (blue) and the CESMv1 Large Ensemble (CESM-LE; [*Kay et al.*, 2015]) mean and range is also plotted (gray). CESM-LE can be regarded as a proxy for E3SMv0. Model results are compared to observations from the Hadley-NOAA/OI merged data product [*Hurrell et al.*, 2008] (red). Note here that, unlike in Figure 23, the anomalies are computed relative to the 1920-1950 period as the CESM data begins at 1920. In the southern basins, E3SMv1 and CESM represent the evolution of observed SST well, where the E3SMv1 SST is slightly closer to data. However, in the northern hemisphere, the E3SMv1 SST anomalies decrease in the 1950s and warm quickly after the 1990s, similar to what is observed in the surface air temperature (Figure 29). Further, the warming effect is strongest in the North Atlantic. This pattern is not seen in the data. We discuss possible causes in the next section.

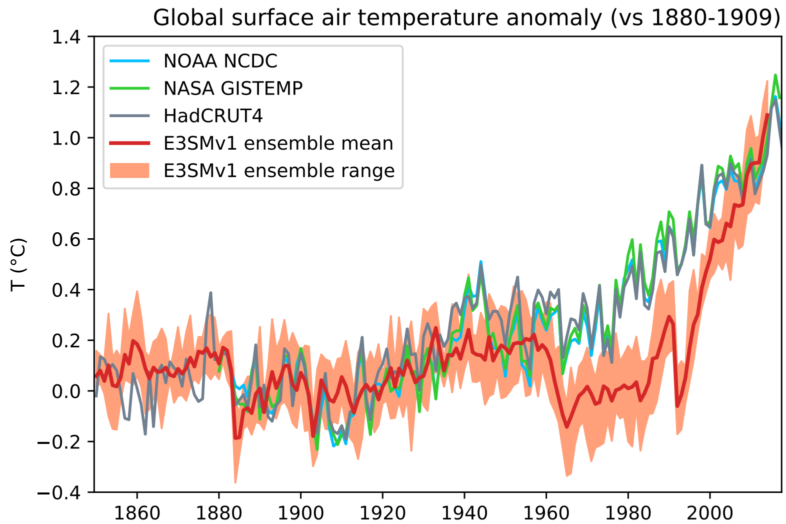

Figure 23. Time evolution of annual global mean surface air temperature anomalies (with respect to 1880-1909). Comparison between observations from NOAA NCDC (blue), NASA GISTEMP (green), HadCRUT4 (grey) and E3SMv1 ensemble mean and range (red and orange).

6 Radiative forcings and sensitivity

We aim to better understand E3SMv1 simulated warming over the historical record by analyzing the model radiative forcings and sensitivity.

6.1 Effective radiative forcing

Effective radiative forcing (ERF) is the change in net downward TOA radiation due to observed changes in forcing agents (such as aerosol and greenhouse gases) but not sea surface temperature (allowing for adjustments in atmospheric temperatures, water vapor and clouds) [*IPCC*, 2013, p. 665]. A common approach to estimate ERF is by differencing net TOA fluxes in a pair of atmosphere-only simulations with identical sea surface temperatures and sea ice concentrations but different radiative forcings [e.g *Hansen*, 2005]. Alternatively, ERF can also be estimated from regression-based approaches [*Gregory et al.*, 2004]. *Forster et al.* [2016] contrast several methodologies to compute ERF and generally recommend fixed SST methodologies.

Total ERF measures the combined effects of GHGs, short-lived gases, aerosols (including interactions with clouds), volcanoes, and land-use and land cover changes (LULCC). We estimate the transient total ERF over the historical record relative to 1850 from pairs

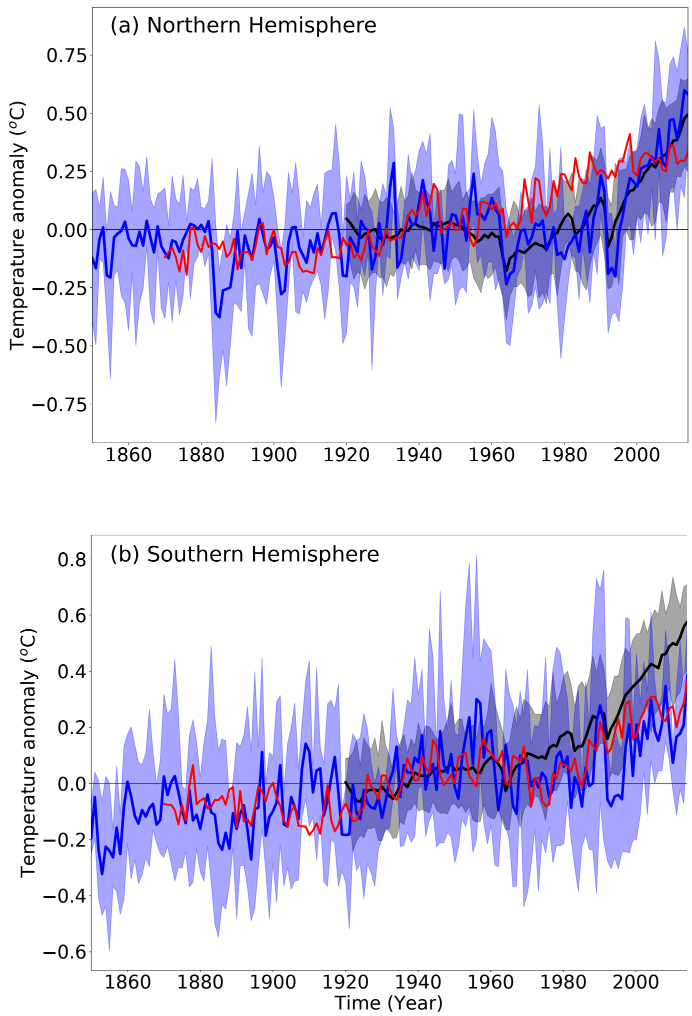

Figure 24. Regionally averaged SST anomalies from 1850-2014 for E3SMv1 historical ensemble (blue), Hadley-NOAA/OI merged SST product (red), and the CESMv1 large ensemble *Kay et al.* [2015] (gray). For the ensemble data, the ensemble maximum and minimum is shown. All anomalies are relative to (1920-1950), which is the beginning of the CESMv1 record. (a) Northern Hemisphere and (b) Southern Hemisphere.

of atmosphere-only simulations. We use the DECK AMIP simulations as reference (*amip_An*) and perform one additional type of simulation with identical sea surface boundary conditions but with all forcing agents held back at their 1850 values (*amip_1850allF_An*). This methodology is referred to as *ERF_trans* in the *Forster et al.* [2016] nomenclature. Separately, we also estimate aerosol-related ERF ($\mathrm{ERF_{ari+aci}}$) which measures total anthropogenic aerosol effects (including aerosol-radiation interactions, aerosol-cloud interactions, and the effect of light-absorbing particles in snow/ice). This requires a third type of simulation in which only aerosols and their precursors are held back at their 1850 values (*amip_1850aeroF_An*). To reduce year-to-year noise in the ERF estimates, we rely on an ensemble of three members.

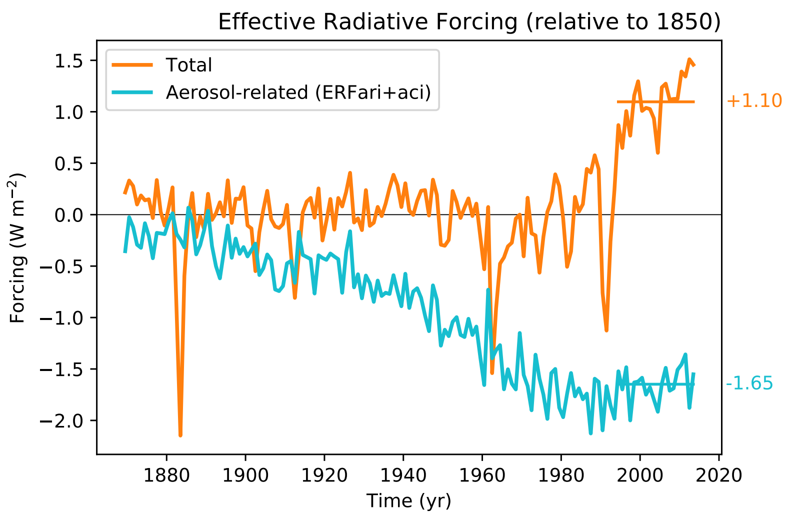

Figure 25. Time evolution of annual global mean total ERF (orange) and aerosol-related ERF (light blue) derived from three ensemble members.

Results are shown in Fig. 25. Aerosol-related ERF (blue) increases in magnitude from the 1920s to the 1970s as anthropogenic aerosol emissions increase. Improved emissions standards in the 1970s cause aerosol-related ERF to stabilize at a value of -1.65 W m^{-2} during the last 20 years (1995-2014). This is substantially larger in magnitude than the IPCC AR5 expert judgment best estimate of -0.9 W m^{-2}[*IPCC*, 2013, p. 620]. It falls within the 5 to 95% uncertainty range of -1.9 to -0.1 W m^{-2}, but outside the likely range of -1.5 to -0.4 W m^{-2}. Strong negative aerosol-related forcing counterbalances warming from greenhouse gases in E3SMv1, with the net effect that total ERF (orange) hovers near zero for the first 100 years (except during volcanic eruptions) and only starts to significantly become positive once aerosol emissions stabilize in the 1970s. Over the last 20 years, the total forcing averages +1.10 W m^{-2}. The IPCC AR5 expert judgment best estimate of the total anthropogenic ERF between 1750 and 2011 is +2.3 W m^{-2} with an uncertainty range of 1.1 to 3.3 W m^{-2} [*IPCC*, 2013, p. 696].

We note that the treatment of planetary boundary layer turbulence, shallow convection, and cloud macrophysics has been unified by a single parameterization (CLUBB) in E3SMv1. As a result, the aerosol-related ERF now includes a contribution from interactions between aerosols and shallow cumulus clouds. In contrast, models whose shallow cumulus is unresponsive to aerosols may be artificially setting part of the aerosol-related ERF to zero.

6.2 Sensitivity

The DECK simulations include two idealized CO_2-forcing simulations designed to estimate climate sensitivity at different time horizons. The equilibrium climate sensitivity (ECS) is defined as the equilibrium surface temperature change resulting from a doubling in CO_2 concentrations [e.g. *IPCC*, 2007]. While it would take thousands of simulated years to run a GCM to equilibrium, ECS is typically approximated from much shorter simulations using the approach of *Gregory et al.* [2004]. This approach takes advantage of the fact that while the responses of global mean surface temperature and TOA energy imbalance to abruptly quadrupling CO_2 are nonlinear in time, the relationship between these variables is usually linear. As a result, ECS can be extrapolated as the surface temperature change associated with zero TOA energy imbalance. This is typically done using 150 year *"abrupt-4xCO2"* simulations as demonstrated for E3SMv1 in Figure 26. Because the surface temperature versus TOA energy imbalance slope weakens with time in most models [*Armour et al.*, 2013; *Andrews et al.*, 2015; *Ceppi and Gregory*, 2017], ECS computed this way is best described as "effective climate sensitivity". Figure 26 shows that E3SMv1 response to abrupt CO_2 quadrupling is relatively linear and produces an ECS of 5.30 K.

Figure 27 illustrates the time evolution of annual-average surface air temperature from the E3SMv1 *abrupt4xCO2* simulation (red). Clearly, 150 years is insufficient to achieve equilibrium. This graphic also includes results from another idealized experiment where CO_2 concentration increases by 1% per year (*1pctCO2*; blue). This second simulation is useful for computing a shorter-timescale measure of warming called the transient

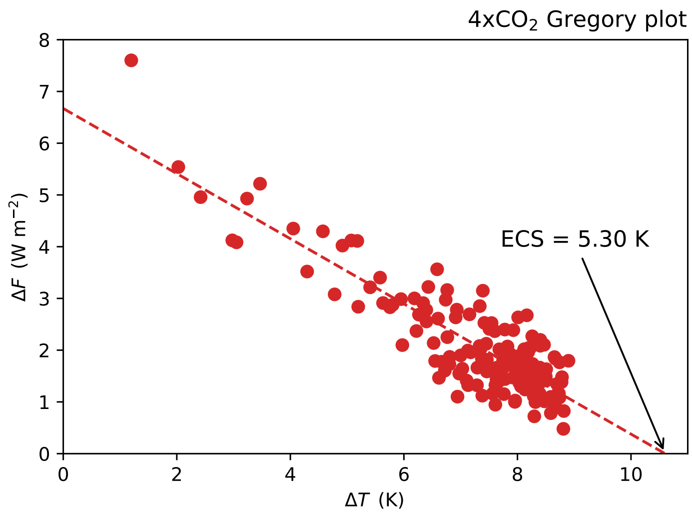

Figure 26. Global annual mean of surface air temperature change vs. TOA net radiation change for 150 years of *abrupt-4xCO2* relative to the underlying control simulation. Linear regression is depicted with a dashed line. Its intersection with the horizontal axis is twice the ECS.

climate response (TCR). TCR is defined as the change in surface temperature averaged for a 20-year period around the time of CO_2 doubling [approximately year 70; *IPCC*, 2007, p. 629] from a *1pctCO2* simulation. As such, it depends on both climate sensitivity and ocean heat uptake rate. For E3SMv1, TCR is 2.93 K from *1pctCO2*.

Both TCR and ECS are on the high side of a compilation of published values [*Knutti et al.*, 2017]. In particular, IPCC AR5 WG1 estimates that ECS is likely (> 66% probability) between 1.5 and 4.5 K, while TCR is likely between 1 and 2.5 K *IPCC* [2013, p. 871]. E3SMv1 ECS and TCR are 17% larger than the likely upper bound from IPCC. While large, these values are below the extremely unlikely (< 5%) upper bounds of 3 K for TCR and 6 K for ECS.

To better understand E3SMv1's high ECS relative to models that took part in CMIP5, we diagnose 2xCO2 effective radiative forcing (ERF_{2xCO2}) and individual radiative feedbacks from the *abrupt-4xCO2* simulation. In this particular case, ERF_{2xCO2} is derived by linear regression (a methodology referred to as *ERF_reg* in the *Forster et al.* [2016] nomenclature). In Figure 28, we show ERFs and radiative feedbacks from 28 CMIP5 models diagnosed in *Caldwell et al.* [2016], along with those diagnosed following the same procedure in E3SMv1. E3SMv1's effective radiative forcing, along with its Planck,

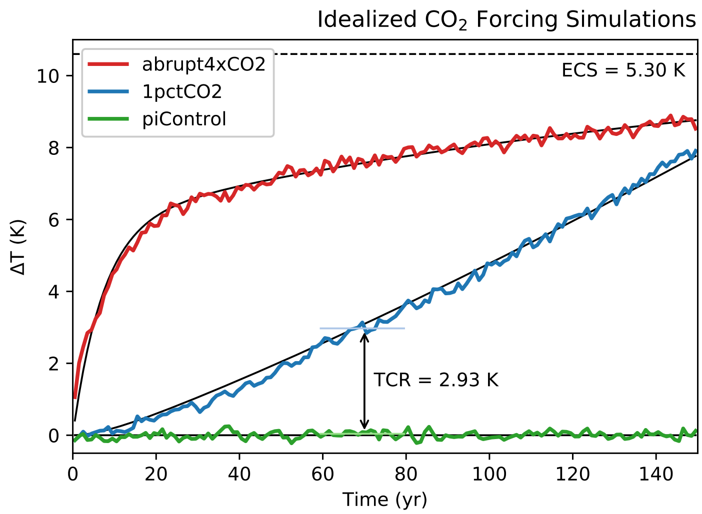

Figure 27. Time evolution of annual global mean air surface temperature anomalies for the idealized CO_2 forcing simulations *abrupt-4xCO2* (red), *1pctCO2* (blue) and the control simulation (*piControl*; green). Solid lines are fits obtained with a two-layer energy balance model (discussed in sub-section 6.3). Also depicted are estimates of ECS and TCR.

lapse rate, water vapor, combined lapse rate plus water vapor, and surface albedo feedbacks are all very close to the CMIP5 multi-model mean values. In contrast, E3SMv1's net cloud feedback is larger than in all but two CMIP5 models. Although its positive LW cloud feedback is slightly smaller than the CMIP5 average, its positive SW cloud feedback is larger than all CMIP5 models. Therefore, E3SMv1âĂŹs high climate sensitivity is solely due to its large positive cloud feedback, which causes its net feedback parameter (which quantifies how strongly the 4xCO_2 forcing is radiatively damped) to be less negative than all but two CMIP5 models ("Total" column of Figure 28). A more detailed diagnosis of the reasons for E3SMv1's large positive cloud feedback will be reported in a subsequent paper.

6.3 Two-layer energy balance model

Having established that E3SMv1 is a high-sensitivity model with a strong aerosol forcing, we now explore the degree to which either the sensitivity or the aerosol forcing can explain the mismatch in the warming trajectory between E3SMv1 and observations (Section 5.6 and Figure 23).

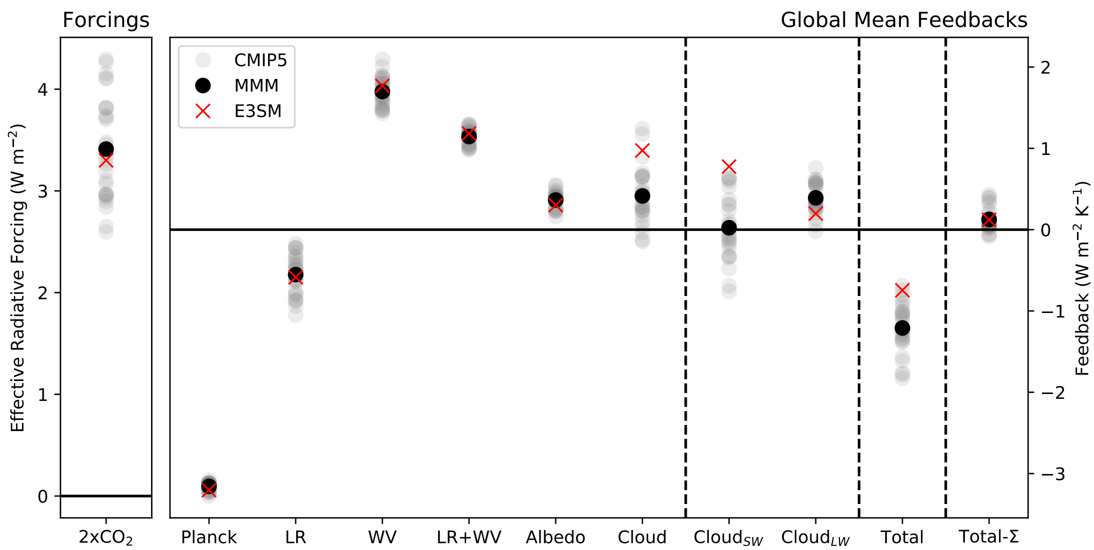

Figure 28. Global and annual mean effective radiative forcings (ERFs) and radiative feedbacks derived as the y-intercepts and slopes, respectively, of the regression line between TOA radiation anomalies and global surface temperature anomalies from 150-year *abrupt-4xCO2* experiments. ERFs are divided by 2 to express them with respect to a doubling of CO_2. The total radiative feedback (Total) is broken down into Planck, lapse rate (LR), water vapor (WV), combined lapse rate plus water vapor (LR+WV), surface albedo (Albedo), and net cloud (Cloud) components using radiative kernels of *Soden et al.* [2008]. The cloud feedback is further broken down into its shortwave (Cloud$_{SW}$) and longwave (Cloud$_{LW}$) components. Individual CMIP5 models are shown in gray circles, the CMIP5 multi-model mean (MMM) is shown as a black circle, and E3SMv1 is shown as a red cross. 'Total' refers to the net radiative feedback computed directly from TOA fluxes. 'Total-Σ' refers to the difference between the directly-calculated net feedback and that estimated by summing kernel-derived components. This value is near zero for E3SMv1, indicating that errors in the overall radiative kernel decomposition of feedbacks are small.

Stevens [2015] uses the historical record to constrain the aerosol forcing. He argues "that an aerosol forcing less than -1.0 W m^{-2} is very unlikely [because] a more negative aerosol forcing would imply that none of the roughly 0.3-K rise in Northern Hemisphere surface temperatures during the 100-yr period from 1850 to 1950 could be attributed to anthropogenic forcing, which seems implausible."

Along similar lines of reasoning, *Zhao et al.* [2018] caution against the often seen "argument that the twentieth century warming does not strongly constrain either climate sensitivity or the strength of aerosol cooling because similar overall warming can result from relatively low sensitivity to CO_2 and weak aerosol cooling, or by high sensitivity and strong aerosol cooling." In their words, this argument holds "only to a limited extent, because of the likelihood of there having been a peak, or at least a plateau, in aerosol forcing in the 1980–1990s. As a result, in order to create the correct overall warming if climate sensitivity is high, one requires large enough aerosol forcing to cancel much of the warming prior to the 1980s, while after the aerosols peak the high sensitivity and reductions in aerosols combine to produce very rapid warming."

Held et al. [2010] demonstrated that the time evolution of GFDL CM2.1 global mean warming could be approximated quite realistically using a simple two-layer box model driven by a time evolving net radiative forcing. Similar approaches have also been used to estimate the climate sensitivity from global mean temperature observations [e.g *Padilla et al.*, 2011; *Aldrin et al.*, 2012]. Within the framework of a two-layer energy-balance model (EBM), *Geoffroy et al.* [2013] derived analytical solutions for the evolution of the global surface temperature in response to idealized forcing scenarios *abrupt-4xCO2* and *1pctCO2*. Furthermore, using 16 AOGCMs from CMIP5, they demonstrated that EBMs calibrated exclusively with *abrupt-4xCO2* data could accurately predict the temperature evolution in *1pctCO2* simulations.

The two-layer EBM is defined by the following system of equations:

$$C\frac{dT}{dt} = \mathcal{F} - \lambda T - \gamma\,(T - T_0) \tag{3}$$

$$C_0\frac{dT_0}{dt} = \gamma\,(T - T_0) \tag{4}$$

Prognostic variables are the temperatures of the upper (T) and deep ocean layers (T_0) with C and C_0 their respective heat capacities. $\mathcal{F}$ is the total radiative forcing, λ the surface feedback parameter and γ the heat exchange coefficient between the upper and deep ocean.

The general solution for the upper (surface) temperature under a time varying forcing is given by Eq. (B8) in *Geoffroy et al.* [2013]:

$$T(t) = \frac{a_f}{\lambda \tau_f} \int_0^t \mathcal{F}(t') e^{-(t-t')/\tau_f}\, dt' + \frac{a_s}{\lambda \tau_s} \int_0^t \mathcal{F}(t') e^{-(t-t')/\tau_s}\, dt' \tag{5}$$

The solution can be interpreted as the sum of a fast and slow convolution of the forcing with exponential decay functions. Table 1 in *Geoffroy et al.* [2013] lists the relationships between the weights (a_f, a_s), time scales (τ_f, τ_s), and the parameters characterizing the model (Eqs 3 and 4).

We calibrate the EBM for E3SMv1 using *abrupt-4xCO2* data following the procedure outlined in *Geoffroy et al.* [2013], except for a small deviation in the second step (p. 1846) when we average over 20 instead of 10 years to estimate the fast time scale as we found that it provides a better fit to *abrupt-4xCO2*. Table 3 lists the parameter values and the fits to *abrupt-4xCO2* and *1pctCO2* are shown with solid black lines in Fig. 27. The fits clearly demonstrate that the EBM calibrated with *abrupt-4xCO2* can accurately predict the behavior of *1pctCO2*. Furthermore, the TCR from the fit (3.07 K) is within 5% of its true value (2.93 K), indicating that for E3SMv1, both ECS and TCR could be estimated from *abrupt-4xCO2* alone.

Table 3. Two-layer EBM parameters calibrated from *abrupt-4xCO2* simulation.

$\mathcal{F}$	6.671	W m^{-2}
λ	0.629	W m^{-2} K^{-1}
a_f	0.558	unitless
τ_f	7.263	year
a_s	0.442	unitless
τ_s	160.093	year

We now explore the EBM's ability to reproduce the predicted E3SMv1 warming over the historical record following the approach of *Held et al.* [2010]. The time varying forcing $\mathcal{F}(t)$ in Eq. (5) is simply the total ERF from Fig. 25 (orange line). The resulting temperature is shown with a thick gray line in Fig. 29a. The simple model predictions agree much better with modeled rather than observed values, lying within the envelope of model ensemble values most of the time. Furthermore, the EBM reproduces – albeit in an exaggerated fashion – the E3SMv1 behavior of a lack of warming during the 1960-1990s followed by an excessive warming trend.

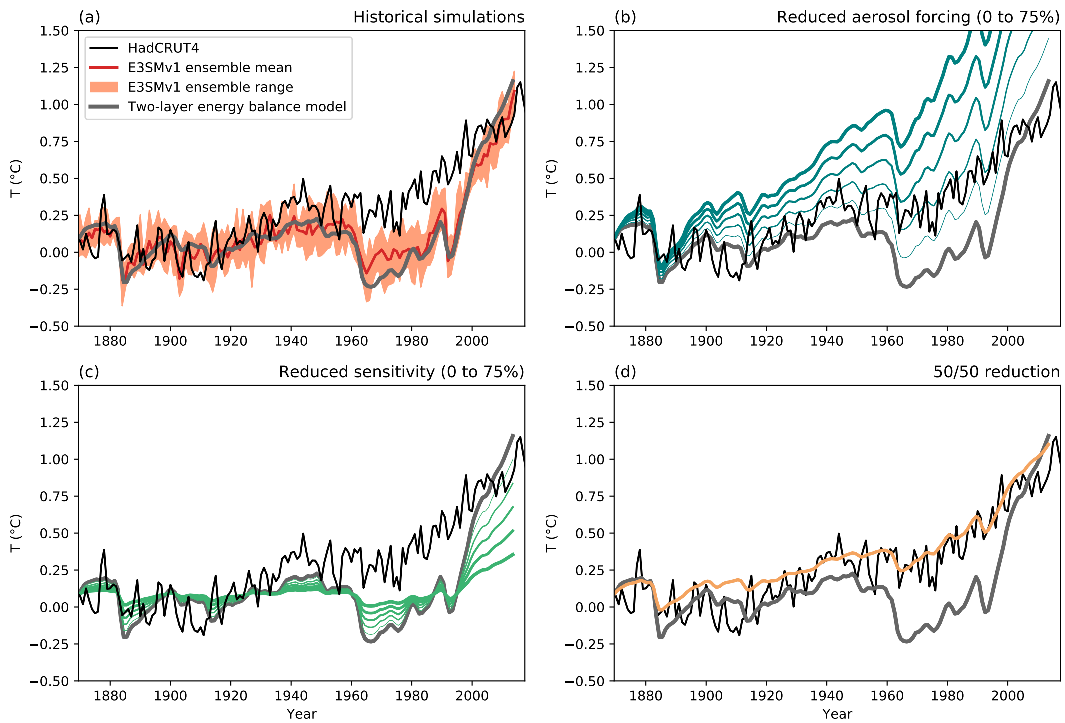

Figure 29. Time evolution of annual global mean surface air temperature anomalies. (a): Observations (HadCRUT4; black), E3SMv1 ensemble mean and range (red and orange), two-layer energy balance model (gray). (b): EBM with reduced aerosol forcing (0% to 75% in 15% increments; blue with increasing line thicknesses). (c): EBM with reduced sensitivity (0% to 75%; green with increasing line thicknesses). (d): EBM with 50% reduction in both aerosol forcing and sensitivity (brown).

With the credibility of the EBM established, the EBM can also be applied to hypothetical scenarios in order to explore the effect of the forcing and sensitivity. New hypothetical total forcing with weaker aerosol forcing can be constructed by linear combinations of the original forcings:

$$\mathcal{F}_{\text{new}} = \mathcal{F}_{\text{tot}} - \alpha_{\text{aero}} \mathcal{F}_{\text{aero}} \tag{6}$$

where $\mathcal{F}_{\text{tot}}$ is the orange line and $\mathcal{F}_{\text{aero}}$ the blue line in Fig. 25. Figure 29b explores reductions in aerosol forcing up to 75% in 15% increments (α_{aero} from 0.0 to 0.75). A 50% reduction corresponds approximately to the median IPCC AR5 value of -0.9 W m^{-2}.

Similarly, we can keep the forcing at its original value and reduce the sensitivity

$$\lambda_{\text{new}} = \frac{\lambda}{\alpha_{\text{sensitivity}}} \tag{7}$$

as illustrated in Fig. 29c for a reduction up to 75% ($\alpha_{\text{sensitivity}}$ from 1.0 to 0.25) with no changes in the fast and slow time scales (τ_f, τ_s) and their corresponding weights (a_f, a_s).

Careful visual inspection of Fig. 29b,c reveals that neither a reduction in aerosol forcing nor a reduction in sensitivity alone is sufficient to improve the match with the historical temperature record. Reducing aerosol forcing alone can improve the match up to the 1980s but not afterwards when the aerosol forcing reaches a plateau and the high sensitivity causes an excessive warming trend (confirming the argument of *Zhao et al.* [2018]). Instead, a substantial reduction in both is needed. For example, a 50% reduction in aerosol forcing and sensitivity (Fig. 29d; brown) matches observations (black) much better than the original EBM calibrated with E3SMv1 (gray). To the extent that the EBM is a good proxy for the behavior of the full model, we conclude that improving the trajectory of the historical warming of E3SMv1 would require a substantial reduction in the magnitude of both aerosol forcing and sensitivity.

7 Conclusion

In this paper, we have described the new E3SMv1 fully-coupled physical model in its standard resolution configuration. This model is designed to serve as a tool to address DOE mission-relevant water cycle questions. We have examined the E3SMv1 simulated climate with a set of experiments from the CMIP6 DECK. Key behaviors and biases are recapitulated below:

- Over the course of the long pre-industrial control simulation, the coupled system has very little model drift, as evidenced in the net TOA flux, global mean surface air temperature, and seasonal range in sea ice area (Figure 2).
- The present-day climate simulated by an ensemble of historical simulations reveals that the atmosphere is credible compared to an ensemble of CMIP5 models (Figure 9) but also subject to biases common to many models, e.g.,
  - stratocumulus coverage (Figure 5),
  - double ITCZ (Figure 6).

- Postively, the atmosphere has a much improved representation of the MJO, in regards to its strength and propagation characteristics (Figure 22).
- The ocean also shows biases consistent with lower resolution ocean models, e.g.,
  - Gulf stream separation (evident in Figure 10),
  - a shallow MLD bias in the SH (Figure 12).
- AMOC is weak (Figure 13) and there is large fresh water bias in the North Atlantic (Figure 11) and accompanying shallow MLD biases (Fig. 12). These biases are certainly related and the subject of ongoing research with E3SMv1.
- The simulated ENSO variability is realistic. It is closer to observations than CESM1 (Figure 20).
- E3SM well simulates the spatial pattern associated with ENSO events and is closer to observations than CESM1 (Figure 21)
- Sea ice concentrations are too high in the Labrador sea (Figure 14) and the seasonal growth of ice is delayed and too rapid, relative to observations.
- Streamflow simulated by E3SMv1 is consistent with observations in magnitude and timing, however, the seasonality is too large in a number of regions (Figure 19).
- E3SMv1's aerosol-related effective radiative forcing ($ERF_{ari+aci}$ = -1.65 W m^{-2}), equilibrium climate sensitivity (ECS = 5.3 K) and transient climate response (TCR = 2.93 K) are larger in magnitude than most CMIP5 models, but fall within previously published uncertainty bounds. Predictions of large future warming are due to unusually large positive shortwave cloud feedback.
- The coupled climate in the historical ensemble doesn't warm as quickly as observations between 1960 and 1990, but warms more rapidly thereafter, with an end result that the E3SMv1 ensemble approaches observations by 2014 (Figure 23).
- An analysis with a simple energy balance model reveals that this mismatch is due to the combination of E3SMv1's strong aerosol-related forcing and high climate sensitivity (Figure 29).

The climate simulated by E3SMv1 has biases broadly consistent with other climate class models, but also has improvements in certain regimes (e.g., tropical variability). These simulations and analysis help to establish the scientific credibility of this new model and set the stage for future additional analysis of these existing simulations as well as new simulations with E3SMv1 (e.g., high resolution coupled, future projections, and regionally refined).

A: Energy correction term

The definition of energy is slightly inconsistent between components of E3SMv1, in particular with respect to the treatment of internal water energy. MPAS-Ocean and sea ice properly account for energy changes due to water temperature changes, but other components currently do not. This inconsistency creates a small spurious energy imbalance between the atmosphere and ocean due to the fact that water evaporates from the ocean surface at a certain temperature and returns to the ocean as precipitation at a different (lower) temperature. Globally averaged, the imbalance is less than 0.5 W m^{-2}.

Kirchhoff's equation [*Glickman*, 2000, p. 432] relates the variation with temperature of the latent heat of a phase change to the difference between the specific heats of the two phases. For water, this is written as:

$$\left(\frac{\partial L_v}{\partial T}\right)_p = c_{pv} - c_w \tag{A.1}$$

where L_v is the latent heat of vaporization, c_{pv} is the specific heat at constant pressure of water vapor, and c_w is the specific heat of liquid water. Like other Earth system models (Isaac Held, personal communication), the E3SMv1 atmosphere component violates Kirchhoff's equation by neglecting variation of L_v with temperature, while at the same time assuming $c_{pv} \neq c_w$.

The ocean experiences a net cooling because it supplies heat to bring the liquid precipitation to the temperature of the sea surface, while solid precipitation is first melted (using heat from the ocean) and then brought to the temperature of the sea surface. However, there is no corresponding warming term in the atmosphere. The net impact is an offset between long term trends in net TOA energy flux and ocean heat content (the largest heat reservoir of the coupled system).

We correct for that imbalance by adding back the missing warming term in the atmosphere with an *ad hoc* correction term. To mimic what is done in the ocean, an energy flux term (IEFLX) is introduced:

$$\mathrm{IEFLX}_i = cp_{sw} * \mathrm{QFLX}_i * T_{surf,i} - cp_{sw} * \mathrm{PRECT}_i * T_{surf,i} \tag{A.2}$$

where i denotes the grid column, cp_{sw} the heat capacity of sea water, QFLX the surface moisture flux, PRECT the precipitation flux, and T_{surf} the surface (skin) temperature. IEFLX is first calculated for each grid box and then globally averaged and later applied as a uniform adjustment to the sensible heat flux at each grid box (Fig. A.1):

$$\mathrm{SHFLX}_i = \mathrm{SHFLX}_i + \frac{\sum_{i=1}^{I}(A_i\ \mathrm{IEFLX}_i)}{\sum_{i=1}^{I}(A_i)}. \tag{A.3}$$

where I denotes the total number of grid columns on the cubed sphere mesh, A_i the grid cell area for column i, and SHFLX the sensible heat flux. The calculated global annual mean IEFLX is about +0.4 W m^{-2}. Sensitivity simulations show that using the IEFLX correction improves energy conservation consistency between net TOA and ocean heat content with minimal impact on the simulated climate.

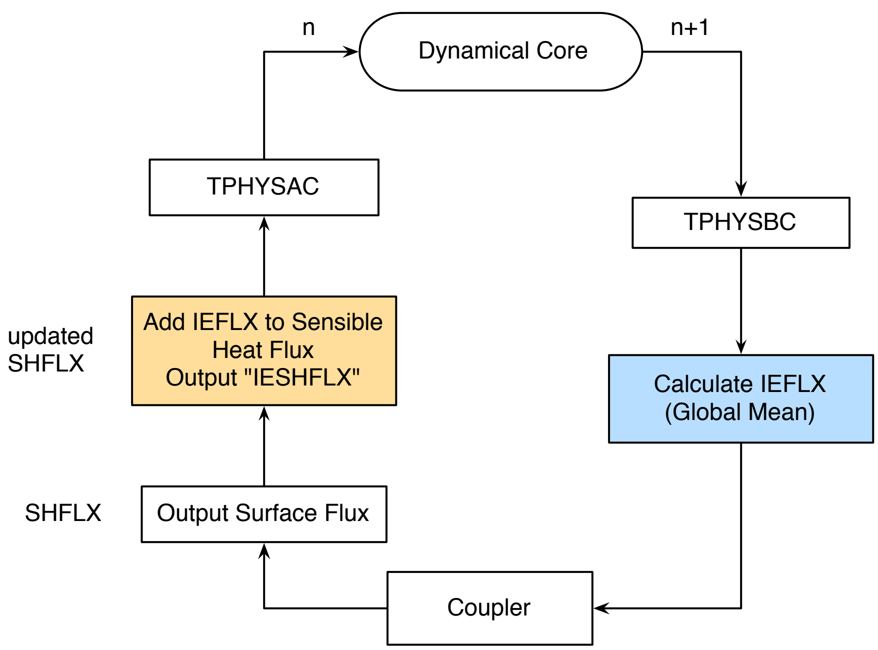

Figure A.1. Flowchart of the IEFLX calculation in E3SMv1. IEFLX shown in this figure is a global mean quantity. TPHYSBC and TPHYSAC indicate the model physics parameterizations before (BC) and after (AC) the coupler calculation. SHFLX indicates the sensible heat flux.

B: Input Data

The E3SMv1 DECK simulations generally followed the input4MIPS datasets, which are described by *Durack et al.* [2018]. The details of the versions used, and any deviations from the input4MIPS data are specified in the sections below.

B.1 Greenhouse Gas Concentrations

Greenhouse gas (GHG) concentrations were specified using v1.2.0 of input4MIPS GHG historical concentrations [*Meinshausen and Vogel*, 2016; *Meinshausen et al.*, 2017] for CO_2, CH_4, N_2O, CFC-12, and CFC-11eq (ie CFC-11 plus all other major halocarbon species converted to give an equivalent amount of CFC-11 forcing). The data was specified annually. The model assumed that the concentration applies to January 1, and interpolated linearly during the year to the next yearâĂŹs value. To enable time interpolation until the end of 2014, concentrations for 2015 and 2016 were added by linear extrapolation from 2013 and 2014. The concentrations were assumed to be uniform throughout the atmosphere (i.e., well mixed).

Ozone concentrations were as specified in sections B.2 and B.3.

B.2 Tropospheric Aerosols & Related Datasets

Aerosol concentrations, sizes, and optical properties were provided by the four-mode Modal Aerosol Module (MAM4, *Liu et al.* [2016]), but modified to include marine organic aerosols (MOA, *Burrows et al.* [2018]), with the coarse mode extended to include carbonaceous aerosols (i.e., BC, POM, MOA and SOA) to treat the resuspension of aerosol particles from evaporated raindrops more appropriately.

Monthly anthropogenic emissions of aerosols and precursor gases for MAM4 were specified as follows. SO_2, sulfate, black carbon (BC), primary organic matter (POM), and second organic aerosol (SOA) gases, were obtained from the CMIP6 (Coupled Model Intercomparison Project Phase 6) emission data sets, as described by *Hoesly et al.* [2017, 2018]. Open fire emissions of SO_2, BC, POM and SOA were from the biomass burning data sets [*van Marle et al.*, 2016, 2017] developed for CMIP6. All the CMIP6 emissions had annual data. Biogenic emissions for SOA precursor sources (e.g., isoprene and monoterpenes) were obtained from the standard MOZART emissions as described by *Em-*

mons et al. [2010]. The vertical distribution of SOA precursor sources was prescribed to mimic the explicit treatment of gas- and particle-phase chemical oxidation of SOA [*Shrivastava et al.*, 2015]. The inject height of fire emissions, as well as industrial and power plant emissions, followed the AeroCom (Aerosol Comparisons between Observations and Models) protocols [*Dentener et al.*, 2006].

The oxidants necessary to calculate secondary aerosol production were read in from a file, which included O_3, OH, H_2O_2, HO_2, and NO_3. The data was provided for each month for one year in each decade (1849, 1855, 1865, . . . , 2015). The ozone values were derived from the input4MIPS Ozone dataset v1.0 [*Hegglin et al.*, 2016]. Concentrations for the other species were not provided by input4MIPS, so the pre-existing specified-oxidant data used by MAM4 was used, for which the provenance is not entirely known, but was probably from a CAM4 based CAM-CHEM transient simulation for IPCC AR5, with an extension to 2015 by copying 2000 values.

B.3 Stratospheric Ozone

We used a prognostic linearized ozone chemistry scheme to calculate stratospheric ozone using a single tracer (Linoz v2, *Hsu and Prather* [2009]). The linearized chemistry coefficients were calculated using the GHG concentrations from v1.2.0 of the input4MIPS GHG historical concentrations with the assistance of Juno Hsu and Michael Prather (private communication), with a 3-year lag as simple way to account for the time surface concentrations take to mix into the stratosphere. The input data was generated for every month in years spaced 5 years apart (1845, 1850, . . . , 2015).

B.4 Stratospheric Aerosols

We modified E3SMv1 to pass the stratospheric aerosol optical properties (extinction, single scattering albedo, asymmetry factor) from input4MIPS directly to the radiation routine (after regridding from the input file to the model grid). We used version 3 of the dataset, which was created to exactly match the E3SMv1 radiation wavelength ranges by one of the dataset creators, Beiping Luo (private communication).

B.5 Sea-Surface Temperature & Sea-Ice

For our AMIP simulations, we used v1.1.3 of the PCMDI sea-surface temperature and sea-ice fractions [*Durack and Taylor*, 2017; *Taylor et al.*, 2000], which cover the years 1870 to 2016. E3SM interpolated ocean temperatures and ice fractions between the mid-month values, hence we used the diddled version of the dataset in which the values were tweaked so that the monthly-mean values in the model matched the monthly-mean values in the original dataset. Since the input dataset used the Gregorian calendar and E3SM uses a 365-day calendar, the model time interpolated on the Gregorian calendar, which caused Feb 29 data to be skipped and will lead to a small discontinuity at the start of March 1 during leap-years.

B.6 Land Use

Land use, and land use change, files were regridded to the E3SM ne30 grid by George Hurtt and Ritvik Sahajpal (private communication) using v2.1h of the input4MIPS land use data [*Hurtt et al.*, 2017].

B.7 Nitrogen Deposition

Nitrogen deposition was not used by E3SM for the DECK simulations.

B.8 Solar Input

Solar irradiances came from v3.2 of the solar irradiance dataset from input4MIPS [*Matthes et al.*, 2017a,b]. The data was specified monthly.

B.9 Orbital Parameters

Earth's orbital parameters were inadvertently fixed to 1990 values for all DECK simulations.

C: Analysis tools

The analysis of this paper was largely enabled through a suite of diagnostic software packages developed in tandem with the model. These packages were designed for the

E3SM development and analysis community to be usable, extensible, and with shareable results, each with a different scientific focus and goal.

New and improved netCDF Operators (NCO) [*Zender*, 2008, 2018] were developed and customized for E3SM analysis, and verified to work on CESM output. These include a climatology generator and a time-series splitter accessed through the new ncclimo operator, and a regridder accessed through the new ncremap operator. Each is a parallelized tool suitable for serial or background-parallel mode execution on personal laptops and workstations, and background-parallel and MPI-parallel operation on high-performance computing nodes. These tools are embedded or used as pre-processing steps for E3SM_Diags, MPAS-Analysis and A-PRIME. Their full documentation is at http://nco.sf.net/nco.html.

E3SM_Diags is a modern, Python-based diagnostics package developed to facilitate evaluating earth system models. The package includes a set of comprehensive toolkits and updated analysis data sets. This software is designed in a flexible, modular, and object-oriented fashion, enabling users to manipulate different processes in a diagnostics workflow. Numerous configuration options for metrics computation (i.e., regridding options) and visualization (i.e., graphical backend, color map, contour levels) are customizable. Built-in functions to generate derived variables and to select diagnostics regions are supported and can be easily expanded to accommodate earth system models with output conventions that are CMIP compliant. Modern computer technologies, such as multiprocessing and containerization are applied in the software development, which enhance the performance and stability of the software. Detailed documentation can be found from https://e3sm.org/resources/tools/diagnostic-tools/e3sm-diagnostics.

MPAS-Analysis (https://github.com/MPAS-Dev/MPAS-Analysis) is a Python-based tool for performing post-processed analysis and plotting of output from E3SMâĂŹs ocean and sea-ice components (MPAS-Ocean and MPAS-Seaice, respectively). MPAS-Analysis uses the NetCDF Operators (NCO) to compute climatologies, extract time series and remap data sets to common reference grids. Comparisons between simulation results and a wide variety of observational data sets are supported on both latitude/longitude and Antarctic stereographic grids. MPAS-Analysis also supports comparisons between E3SM simulations, allowing users to examine the influence of changing meshes, resolution, parameters, model physics, etc. Parallelism has been introduced into MPAS-Analysis by breaking each analysis task into modular subtasks that can be run in parallel to efficiently produce hundreds of plots. MPAS-Analysis is aware of E3SM namelists, meaning that tasks are automatically disabled for runs where the necessary output was not produced. The end result of running MPAS-Analysis is a website with image galleries of all plots, sorted by component and analysis type, as well as a set of NetCDF files containing the post-processed data, available for further analysis.

A-PRIME is a âĂIJpriorityâĂİ metrics package that is designed to provide a quick, broad overview of coupled model behavior [*Evans et al.*, 2018]. The target user would execute A-PRIME on model data as a run is progressing to determine whether the model is on track to produce global level expected behavior. It provides a suite of averaged and time series behavior of the most common variables that drive radiation, dynamical, and hydrological balance. When there are sufficient simulation years available, it also provides ENSO metrics. The top-level directory of the software provides a generic script that targets execution on DOE supercomputers, where E3SM simulations are currently executed and/or postprocessed. These scripts point to Python postprocessing and visualization modules for multiple components in the coupled model. The ocean and sea ice modules load portions of the MPAS-Analysis diagnostics as a submodule.

Acknowledgments

This research was supported as part of the Energy Exascale Earth System Model (E3SM) project, funded by the U.S. Department of Energy, Office of Science, Office of Biological and Environmental Research. SAK and MDZ acknowledge support from the Regional and Global Modeling and Analysis Program of the U. S. Department of Energy, Office of Science, Office of Biological and Environmental Research. JLM was supported by DE-SC0012778. J.-H. Yoon was partially supported by the National Research Foundation grant: NRF_2017R1A2b4007480.

We thank the following for their assistance adapting the input4MIPS CMIP6 datasets to the E3SM model: Michael Prather and Juno Hsu (appendix B.3), Beiping Luo (appendix B.4), George Hurtt and Ritvik Sahajpal (appendix B.6).

Simulations described in this work and most developmental simulations leading up to them relied on computational resources provided by the National Energy Research Scientific Computing Center (NERSC), a DOE Office of Science User Facility supported by the Office of Science of the U.S. Department of Energy under Contract No. DE-AC02-05CH11231. The remaining developmental simulations used a high-performance computing cluster provided by the BER Earth System Modeling program and operated by the Laboratory Computing Resource Center at Argonne National Laboratory as well as resources of the Oak Ridge Leadership Computing Facility, which is a DOE Office of Science User Facility supported under Contract DE-AC05-00OR22725. Work at LLNL was performed under the auspices of the U.S. Department of Energy by Lawrence Livermore National Laboratory under Contract DE-AC52-07NA27344. The Pacific Northwest National Laboratory (PNNL) is operated for DOE by Battelle Memorial Institute under contract DE-AC05-76RLO1830. The National Center for Atmospheric Research is sponsored by the National Science Foundation under Cooperative Agreement No. 1852977.

The E3SM project, code, simulation configurations, model output, and tools to work with the output are described at https://e3sm.org. Instructions on how to get started running E3SM are available at https://e3sm.org/model/running-e3sm/e3sm-quick-start. All model codes may be accessed on the GitHub repository at https://github.com/E3SM-Project/E3SM. Model output data are accessible directly on NERSC or through the DOE Earth System Grid Federation at https://esgf-node.llnl.gov/projects/e3sm.

References

Adcroft, A., and J.-M. Campin (2004), Rescaled height coordinates for accurate representation of free-surface flows in ocean circulation models, *Ocean Modelling*, *7*, 269–284, doi:10.1016/j.ocemod.2003.09.003.

Adler, R. F., G. J. Huffman, A. Chang, R. Ferraro, P.-P. Xie, J. Janowiak, B. Rudolf, U. Schneider, S. Curtis, D. Bolvin, A. Gruber, J. Susskind, P. Arkin, and E. Nelkin (2003), The Version-2 Global Precipitation Climatology Project (GPCP) monthly precipitation analysis (1979–present), *Journal of Hydrometeorology*, *4*(6), 1147–1167, doi: 10.1175/1525-7541(2003)004$<$1147:tvgpcp$>$2.0.co;2.

Aldrin, M., M. Holden, P. Guttorp, R. B. Skeie, G. Myhre, and T. K. Berntsen (2012), Bayesian estimation of climate sensitivity based on a simple climate model fitted to observations of hemispheric temperatures and global ocean heat content, *Environmetrics*, *23*(3), 253–271, doi:10.1002/env.2140.

Andrews, T., J. M. Gregory, and M. J. Webb (2015), The dependence of radiative forcing and feedback on evolving patterns of surface temperature change in climate models, *Journal of Climate*, *28*(4), 1630–1648, doi:10.1175/jcli-d-14-00545.1.

Annamalai, H., and J. M. Slingo (2001), ActiveâĂŁ/âĂŁbreak cycles: diagnosis of the intraseasonal variability of the asian summer monsoon, *Climate Dynamics*, *18*(1), 85–102, doi:10.1007/s003820100161.

Arakawa, A., and V. R. Lamb (1977), Computational design of the basic dynamical processes of the UCLA General Circulation Model, in *General Circulation Models of the Atmosphere*, *Methods in Computational Physics: Advances in Research and Applications*, vol. 17, edited by J. Chang, pp. 173–265, Elsevier, doi:10.1016/B978-0-12-460817-7.50009-4.

Armour, K. C., C. M. Bitz, and G. H. Roe (2013), Time-varying climate sensitivity from regional feedbacks, *J. Climate*, *26*, 4518âĂŞ4534, doi:10.1175/JCLI-D-12-00544.1.

Bader, D., W. Collins, R. Jacob, P. J. P. Rasch, M. Taylor, P. Thornton, and D. Williams (2014), Accelerated Climate Modeling for Energy, U.S. Department of Energy. Retrieved from https://climatemodeling.science.energy.gov/sites/default/files/publications/acme-project-strategy-plan.pdf.

Bourke, R., and A. McLaren (1992), Contour Mapping of Arctic Basin Ice Draft and Roughness Parameters, *Journal of Geophysical Research*, *97*(C11), 17,715–17,728.

Branstetter, M. L., and D. J. Erickson III (2003), Continental runoff dynamics in the Community Climate System Model 2 (CCSM2) control simulation, *Journal of Geophysical Research*, *108*(D17), doi:10.1029/2002jd003212.

Briegleb, B. P., and B. Light (2007), A Delta-Eddington multiple scattering parameterization for solar radiation in the sea ice component of the Community Climate System Model, *Tech. Rep. NCAR/TN-472+STR*, National Center for Atmospheric Research, Boulder, Colorado USA.

Burrows, S. M., R. Easter, X. Liu, P. L. Ma, H. Wang, S. M. Elliott, B. Singh, K. Zhang, and P. J. Rasch (2018), OCEANFILMS sea-spray organic aerosol emissions - Part 1: implementation and impacts on clouds, *Atmos. Chem. Phys. Discuss.*, pp. 1–27, doi:10.5194/acp-2018-70.

Caldwell, P. M., M. D. Zelinka, K. E. Taylor, and K. Marvel (2016), Quantifying the sources of intermodel spread in Equilibrium Climate Sensitivity, *Journal of Climate*, *29*(2), 513–524, doi:10.1175/jcli-d-15-0352.1.

Campin, J.-M., J. Marshall, and D. Ferreira (2008), Sea ice–ocean coupling using a rescaled vertical coordinate zâĹŮ, *Ocean Modelling*, *24*(1-2), 1–14.

Cavalieri, D. J., C. L. Parkinson, P. Gloersen, and H. J. Zwally (1996), Sea ice concentrations from Nimbus-7 SMMR and DMSP SSM/I-SSMIS passive microwave data, version 1, doi:10.5067/8GQ8LZQVL0VL.

Ceppi, P., and J. M. Gregory (2017), Relationship of tropospheric stability to climate sensitivity and earth's observed radiation budget, *Proceedings of the National Academy of Sciences*, *114*(50), 13,126–13,131, doi:10.1073/pnas.1714308114.

Cess, R. D., G. L. Potter, J. P. Blanchet, G. J. Boer, S. J. Ghan, J. T. Kiehl, H. Le Treut, Z.-X. Li, X.-Z. Liang, J. F. B. Mitchell, J.-J. Morcrette, D. A. Randall, M. R. Riches, E. Roeckner, U. Schlese, A. Slingo, K. E. Taylor, W. M. Washington, R. T. Wetherald, and I. Yagai (1989), Interpretation of cloud-climate feedback as produced by 14 atmospheric general circulation models, *Science*, *245*(4917), 513–516, doi:10.1126/science.245.4917.513.

Cheng, W., J. C. Chiang, and D. Zhang (2013), Atlantic meridional overturning circulation (amoc) in cmip5 models: Rcp and historical simulations, *Journal of Climate*, *26*(18), 7187–7197.

Collins, N., G. Theurich, C. Deluca, M. Suarez, A. Trayanov, V. Balaji, P. Li, W. Yang, C. Hill, and A. Da Silva (2005), Design and implementation of components in the earth system modeling framework, *The International Journal of High Performance Computing Applications*, *19*(3), 341–350.

Craig, A. P., M. Vertenstein, and R. Jacob (2012), A new flexible coupler for earth system modeling developed for ccsm4 and cesm1, *The International Journal of High Performance Computing Applications*, *26*(1), 31–42, doi:10.1177/1094342011428141.

Dasgupta, G. (2003), Interpolants within convex polygons: Wachpress' shape functions, *J. Aerospac. Eng.*, *16*, 1–8, doi:10.1061/(ASCE)0893-1321(2003)16:1(1).

Dee, D. P., S. M. Uppala, A. J. Simmons, P. Berrisford, P. Poli, S. Kobayashi, U. Andrae, M. A. Balmaseda, G. Balsamo, P. Bauer, P. Bechtold, A. C. M. Beljaars, L. van de Berg, J. Bidlot, N. Bormann, C. Delsol, R. Dragani, M. Fuentes, A. J. Geer, L. Haimberger, S. B. Healy, H. Hersbach, E. V. Hólm, L. Isaksen, P. Kållberg, M. Köhler, M. Matricardi, A. P. McNally, B. M. Monge-Sanz, J.-J. Morcrette, B.-K. Park, C. Peubey, P. de Rosnay, C. Tavolato, J.-N. Thépaut, and F. Vitart (2011), The ERA-interim reanalysis: configuration and performance of the data assimilation system, *Quar-*

terly Journal of the Royal Meteorological Society, *137*(656), 553–597, doi:10.1002/qj.828.

Dentener, F., S. Kinne, T. Bond, O. Boucher, J. Cofala, S. Generoso, P. Ginoux, S. Gong, J. J. Hoelzemann, A. Ito, L. Marelli, J. E. Penner, J. P. Putaud, C. Textor, M. Schulz, G. R. van der Werf, and J. Wilson (2006), Emissions of primary aerosol and precursor gases in the years 2000 and 1750 prescribed data-sets for AeroCom, *Atmos. Chem. Phys.*, *6*(12), 4321–4344, doi:10.5194/acp-6-4321-2006.

Dukowicz, J. K., and J. R. Baumgardner (2000), Incremental remapping as a transport/advection algorithm, *Journal of Computational Physics*, *160*(1), 318–335, doi:10.1006/jcph.2000.6465.

Dunavant, D. A. (1985), High degree efficient symmetrical Gaussian quadrature rules for the triangle, *International Journal for Numerical Methods in Engineering*, *21*(6), 1129–1148, doi:10.1002/nme.1620210612.

Durack, P. J., and K. E. Taylor (2017), PCMDI AMIP SST and sea-ice boundary conditions version 1.1.3, doi:10.22033/ESGF/input4MIPs.1735.

Durack, P. J., K. E. Taylor, V. Eyring, S. K. Ames, T. Hoang, D. Nadeau, C. Doutriaux, M. Stockhause, and P. J. Gleckler (2018), Toward standardized data sets for climate model experimentation, *Eos*, *99*, doi:10.1029/2018EO101751.

Emmons, L. K., S. Walters, P. G. Hess, J. F. Lamarque, G. G. Pfister, D. Fillmore, C. Granier, A. Guenther, D. Kinnison, T. Laepple, J. Orlando, X. Tie, G. Tyndall, C. Wiedinmyer, S. L. Baughcum, and S. Kloster (2010), Description and evaluation of the model for ozone and related chemical tracers, version 4 (MOZART-4), *Geoscientific Model Development*, *3*(1), 43–67, doi:10.5194/gmd-3-43-2010.

Evans, K. J., S. Mahajan, M. Veneziani, X. S. Asay-Davis, L. P. Van Roekel, M. Branstetter, M. R. Petersen, P. J. Wolfram, C. S. Zender, and S. M. Burrows (2018), ACME Priority Metrics (A-PRIME), doi:10.5281/zenodo.1311053.

Eyring, V., S. Bony, G. A. Meehl, C. A. Senior, B. Stevens, R. J. Stouffer, and K. E. Taylor (2016), Overview of the Coupled Model Intercomparison Project Phase 6 (CMIP6) experimental design and organization, *Geoscientific Model Development*, *9*(5), 1937–1958, doi:10.5194/gmd-9-1937-2016.

Fekete, B. M., and C. J. Vörösmarty (2011), ISLSCP II UNH/GRDC Composite Monthly Runoff, doi:10.3334/ornldaac/994.

Flanner, M. G., X. Liu, C. Zhou, J. E. Penner, and C. Jiao (2012), Enhanced solar energy absorption by internally-mixed black carbon in snow grains, *Atmospheric Chemistry and Physics*, *12*(10), 4699–4721, doi:10.5194/acp-12-4699-2012.

Forster, P. M., T. Richardson, A. C. Maycock, C. J. Smith, B. H. Samset, G. Myhre, T. Andrews, R. Pincus, and M. Schulz (2016), Recommendations for diagnosing effective radiative forcing from climate models for CMIP6, *Journal of Geophysical Research: Atmospheres*, *121*(20), 12,460–12,475, doi:10.1002/2016JD025320.

Gent, P. R., and J. C. McWilliams (1990), Isopycnal mixing in ocean circulation models, *Journal of Physical Oceanography*, *20*(1), 150–155.

Geoffroy, O., D. Saint-Martin, D. J. L. Olivié, A. Voldoire, G. Bellon, and S. Tytéca (2013), Transient climate response in a two-layer energy-balance model. Part i: Analytical solution and parameter calibration using CMIP5 AOGCM experiments, *Journal of Climate*, *26*(6), 1841–1857, doi:10.1175/jcli-d-12-00195.1.

Gettelman, A., H. Morrison, S. Santos, P. Bogenschutz, and P. M. Caldwell (2015), Advanced two-moment bulk microphysics for global models. Part II: Global model solutions and aerosol-cloud interactions, *Journal of Climate*, *28*(3), 1288–1307, doi: 10.1175/jcli-d-14-00103.1.

GISTEMP Team (2018), GISS surface temperature analysis (GISTEMP), NASA Goddard Institute for Space Studies. https://data.giss.nasa.gov/gistemp. Dataset accessed 2018-05-24.

Gleckler, P., C. Doutriaux, P. Durack, K. Taylor, Y. Zhang, D. Williams, E. Mason, and J. Servonnat (2016), A more powerful reality test for climate models, *Eos*, *97*, doi:10.1029/2016eo051663.

Gleckler, P. J., K. E. Taylor, and C. Doutriaux (2008), Performance metrics for climate models, *Journal of Geophysical Research*, *113*(D6), doi:10.1029/2007jd008972.

Glickman, T. S. (2000), *Glossary of Meteorology, Second Edition*, 855 pp., American Meteorological Society.

Golaz, J.-C., V. E. Larson, and W. R. Cotton (2002), A PDF-based model for boundary layer clouds. Part I: Method and model description, *Journal of the Atmospheric Sciences*, *59*(24), 3540–3551, doi:10.1175/1520-0469(2002)059<3540:APBMFB>2.0.CO;2.

Gregory, J. M., W. J. Ingram, M. A. Palmer, G. S. Jones, P. A. Stott, R. B. Thorpe, J. A. Lowe, T. C. Johns, and K. D. Williams (2004), A new method for diagnosing radiative forcing and climate sensitivity, *Geophysical Research Letters*, *31*(3), doi:

10.1029/2003gl018747.

Griffies, S. M., R. C. Pacanowski, and R. W. Hallberg (2000), Spurious diapycnal mixing associated with advection in az-coordinate ocean model, *Monthly Weather Review*, *128*(3), 538–564.

Hansen, J. (2005), Efficacy of climate forcings, *Journal of Geophysical Research*, *110*(D18), doi:10.1029/2005jd005776.

Hansen, J., R. Ruedy, M. Sato, and K. Lo (2010), Global surface temperature change, *Reviews of Geophysics*, *48*(4), doi:10.1029/2010rg000345.

Hawkins, E., and R. Sutton (2016), Connecting climate model projections of global temperature change with the real world, *Bulletin of the American Meteorological Society*, *97*(6), 963–980, doi:10.1175/bams-d-14-00154.1.

Hegglin, M., D. Kinnison, J.-F. Lamarque, and D. Plummer (2016), CCMI ozone in support of CMIP6 - version 1.0, doi:10.22033/ESGF/input4MIPs.1115.

Held, I. M., M. Winton, K. Takahashi, T. Delworth, F. Zeng, and G. K. Vallis (2010), Probing the fast and slow components of global warming by returning abruptly to preindustrial forcing, *Journal of Climate*, *23*(9), 2418–2427, doi:10.1175/2009jcli3466.1.

Hibler, W., A. Roberts, P. Heil, A. Y. Proshutinsky, H. Simmons, and J. Lovick (2006), Modeling m2 tidal variability in arctic sea-ice drift and deformation, *Annals of Glaciology*, *44*, 418–428.

Hibler III, W. D. (1979), A dynamic thermodynamic sea ice model, *Journal of Physical Oceanography*, *9*(4), 815–846, doi:10.1175/1520-0485(1979)009$<$0815:ADTSIM$>$2.0.CO;2.

Hoesly, R., S. Smith, L. Feng, Z. Klimont, G. Janssens-Maenhout, T. Pitkanen, J. J. Seibert, L. Vu, R. J. Andres, R. M. Bolt, T. C. Bond, L. Dawidowski, N. Kholod, J.-i. Kurokawa, M. Li, L. Liu, Z. Lu, M. C. P. Moura, P. R. O'Rourke, and Q. Zhang (2017), Historical emissions (1750 - 2014) - CEDS - v2017-05-18, doi:10.22033/ESGF/input4MIPs.1241.

Hoesly, R. M., S. J. Smith, L. Feng, Z. Klimont, G. Janssens-Maenhout, T. Pitkanen, J. J. Seibert, L. Vu, R. J. Andres, R. M. Bolt, T. C. Bond, L. Dawidowski, N. Kholod, J. I. Kurokawa, M. Li, L. Liu, Z. Lu, M. C. P. Moura, P. R. O'Rourke, and Q. Zhang (2018), Historical (1750-2014) anthropogenic emissions of reactive gases and aerosols from the community emissions data system (CEDS), *Geosci. Model Dev.*, *11*(1), 369–408, doi:10.5194/gmd-11-369-2018.

Holland, M. M., D. A. Bailey, B. P. Briegleb, B. Light, and E. Hunke (2012), Improved sea ice shortwave radiation physics in CCSM4: The impact of melt ponds and aerosols on arctic sea ice, *Journal of Climate*, *25*(5), 1413–1430, doi:10.1175/JCLI-D-11-00078.1.

Holte, J., L. D. Talley, J. Gilson, and D. Roemmich (2017), An Argo mixed layer climatology and database, *Geophysical Research Letters*, *44*(11), 5618–5626.

Hourdin, F., T. Mauritsen, A. Gettelman, J.-C. Golaz, V. Balaji, Q. Duan, D. Folini, D. Ji, D. Klocke, Y. Qian, F. Rauser, C. Rio, L. Tomassini, M. Watanabe, and D. Williamson (2017), The art and science of climate model tuning, *Bulletin of the American Meteorological Society*, *98*(3), 589–602, doi:10.1175/bams-d-15-00135.1.

Hsu, J., and M. J. Prather (2009), Stratospheric variability and tropospheric ozone, *Journal of Geophysical Research-Atmospheres*, *114*, 15, doi:10.1029/2008jd010942.

Huang, B., V. F. Banzon, E. Freeman, J. Lawrimore, W. Liu, T. C. Peterson, T. M. Smith, P. W. Thorne, S. D. Woodruff, and H.-M. Zhang (2015), Extended Reconstructed Sea Surface Temperature (ERSST), Version 4., NOAA National Centers for Environmental Information, doi:10.7289/V5KD1VVF.

Huffman, G. J., R. F. Adler, D. T. Bolvin, and G. Gu (2009), Improving the global precipitation record: GPCP version 2.1, *Geophysical Research Letters*, *36*(17), doi:10.1029/2009gl040000.

Hunke, E., R. Allard, D. Bailey, A. Craig, A. Damsgaard, F. Dupont, A. DuVivier, M. Holland, N. Jeffery, J.-F. Lemieux, C. Newman, A. Roberts, A. Turner, M. Turner, and M. Winton (2018), CICE-Consortium/Icepack version 1.0.2, doi:10.5281/zenodo.1213463.

Hunke, E. C., and J. K. Dukowicz (1997), An elastic-viscous-plastic model for sea ice dynamics, *Journal of Physical Oceanography*, *27*(9), 1849–1867, doi:10.1175/1520-0485(1997)027$<$1849:AEVPMF$>$2.0.CO;2.

Hunke, E. C., and J. K. Dukowicz (2002), The elastic-viscous-plastic sea ice dynamics model in general orthogonal curvilinear coordinates on a sphere – Incorporation of metric terms, *Monthly Weather Review*, *130*(7), 1848–1865, doi:10.1175/1520-0493(2002)130$<$1848:TEVPSI$>$2.0.CO;2.

Hunke, E. C., D. A. Hebert, and O. Lecomte (2013), Level-ice melt ponds in the Los Alamos sea ice model, CICE, *Ocean Modelling*, *71*, 26–42, doi:10.1016/j.ocemod.2012.11.008.

Hunke, E. C., W. H. Lipscomb, A. K. Turner, N. Jeffery, and S. Elliott (2015), CICE: the Los Alamos sea ice model documentation and software user's manual version 5.1, *Tech. rep.*, Los Alamos National Laboratory.

Hurrell, J. W., J. J. Hack, D. Shea, J. M. Caron, and J. Rosinski (2008), A new sea surface temperature and sea ice boundary dataset for the community atmosphere model, *Journal of Climate*, *21*(19), 5145–5153.

Hurrell, J. W., M. M. Holland, P. R. Gent, S. Ghan, J. E. Kay, P. J. Kushner, J.-F. Lamarque, W. G. Large, D. Lawrence, K. Lindsay, W. H. Lipscomb, M. C. Long, N. Mahowald, D. R. Marsh, R. B. Neale, P. Rasch, S. Vavrus, M. Vertenstein, D. Bader, W. D. Collins, J. J. Hack, J. Kiehl, and S. Marshall (2013), The community earth system model: A framework for collaborative research, *Bulletin of the American Meteorological Society*, *94*(9), 1339–1360, doi:10.1175/bams-d-12-00121.1.

Hurtt, G., L. Chini, R. Sahajpal, and S. Frolking (2017), input4MIPs.UofMD.landState.CMIP.UofMD-landState-2-1-h, doi:10.22033/ESGF/input4MIPs.1127.

IPCC (2007), Climate change 2007: The physical science basis, in *Contribution of Working Group I to the Fourth Assessment Report of the Intergovernmental Panel on Climate Change*, edited by S. Solomon, D. Qin, M. Manning, Z. Chen, M. Marquis, K. Acertyt, M. Tignor, and H. L. Miller, p. 996pp, Cambridge University Press, Cambridge, United Kingdom and New York, NY, USA.

IPCC (2013), *Climate Change 2013: The Physical Science Basis. Contribution of Working Group I to the Fifth Assessment Report of the Intergovernmental Panel on Climate Change*, 1535 pp., Cambridge University Press, Cambridge, United Kingdom and New York, NY, USA, doi:10.1017/CBO9781107415324.

Jacob, R., J. Larson, and E. Ong (2005), M× n communication and parallel interpolation in community climate system model version 3 using the model coupling toolkit, *The International Journal of High Performance Computing Applications*, *19*(3), 293–307.

Jochum, M., G. Danabasoglu, M. Holland, Y.-O. Kwon, and W. Large (2008), Ocean viscosity and climate, *Journal of Geophysical Research: Oceans*, *113*(C6).

Jones, P. D., M. New, D. E. Parker, S. Martin, and I. G. Rigor (1999), Surface air temperature and its changes over the past 150 years, *Reviews of Geophysics*, *37*(2), 173–199, doi:10.1029/1999rg900002.

Kay, J., C. Deser, A. Phillips, A. Mai, C. Hannay, G. Strand, J. Arblaster, S. Bates, G. Danabasoglu, J. Edwards, et al. (2015), The Community Earth System Model (CESM) large ensemble project: A community resource for studying climate change in the presence of internal climate variability, *Bulletin of the American Meteorological Society*, *96*(8), 1333–1349.

Knutti, R., M. A. A. Rugenstein, and G. C. Hegerl (2017), Beyond equilibrium climate sensitivity, *Nature Geoscience*, *10*(10), 727–736, doi:10.1038/ngeo3017.

Kwok, R., and G. F. Cunningham (2008), ICESat over Arctic sea ice: Estimation of snow depth and ice thickness, *Journal of Geophysical Research-Oceans*, *113*(C8), doi:10.1029/2008jc004753.

Kwok, R., and D. A. Rothrock (2009), Decline in Arctic sea ice thickness from submarine and ICESat records: 1958? @ S2008, *Geophysical Research Letters*, *36*(15), doi:10.1029/2009gl039035.

Lagerloef, G., H.-Y. Kao, T. Meissner, and J. Vazquez (2015), Aquarius salinity validation analysis; data version 4.0, Aquarius Science Team Technology Document, ftp://podaac.jpl.nasa.gov/SalinityDensity/aquarius/docs/v4/AQ-014-PS-0016_AquariusSalinityDataValidationAnalysis_DatasetVersion4.0and3.0.pdf.

Large, W., and S. Yeager (2009), The global climatology of an interannually varying air–sea flux data set, *Clim. Dynam.*, *33*(2-3), 341–364, doi:10.1007/s00382-008-0441-3.

Larson, J., R. Jacob, and E. Ong (2005), The model coupling toolkit: a new Fortran90 toolkit for building multiphysics parallel coupled models, *The International Journal of High Performance Computing Applications*, *19*(3), 277–292.

Larson, V. E. (2017), CLUBB-SILHS: A parameterization of subgrid variability in the atmosphere, arXiv:1711.03675.

Larson, V. E., and J.-C. Golaz (2005), Using probability density functions to derive consistent closure relationships among higher-order moments, *Monthly Weather Review*, *133*(4), 1023–1042, doi:10.1175/MWR2902.1.

Lawrence, P. J., and T. N. Chase (2007), Representing a new MODIS consistent land surface in the Community Land Model (CLM 3.0), *Journal of Geophysical Research*, *112*(G1), doi:10.1029/2006jg000168.

Leung, L. R., D. Bader, M. Taylor, M. R, and D. Koch (2019), An introduction to the Energy Exascale Earth System Model (E3SM) special collection, *Journal of Advances in Modeling Earth Systems*, joint submission to AGU Special Collection on E3SM.

Li, H., M. S. Wigmosta, H. Wu, M. Huang, Y. Ke, A. M. Coleman, and L. R. Leung (2013), A physically based runoff routing model for land surface and earth system models, *Journal of Hydrometeorology*, *14*(3), 808–828, doi:10.1175/jhm-d-12-015.1.

Li, H.-Y., L. R. Leung, A. Getirana, M. Huang, H. Wu, Y. Xu, J. Guo, and N. Voisin (2015), Evaluating global streamflow simulations by a physically based routing model coupled with the Community Land Model, *Journal of Hydrometeorology*, *16*(2), 948–971, doi:10.1175/jhm-d-14-0079.1.

Lipscomb, W. H. (2001), Remapping the thickness distribution in sea ice models, *Journal of Geophysical Research: Oceans*, *106*(C7), 13,989–14,000, doi:10.1029/2000JC000518.

Lipscomb, W. H., and E. C. Hunke (2004), Modeling sea ice transport using incremental remapping, *Monthly Weather Review*, *132*(6), 1341–1354, doi:10.1175/1520-0493(2004)132$<$1341:MSITUI$>$2.0.CO;2.

Lipscomb, W. H., and T. D. Ringler (2005), An incremental remapping transport scheme on a spherical geodesic grid, *Monthly Weather Review*, *133*(8), 2335–2350, doi:10.1175/MWR2983.1.

Lipscomb, W. H., E. C. Hunke, W. Maslowski, and J. Jakacki (2007), Ridging, strength, and stability in high-resolution sea ice models, *Journal of Geophysical Research: Oceans*, *112*(C3), doi:10.1029/2005JC003355, C03S91.

Lique, C., M. M. Holland, Y. B. Dibike, D. M. Lawrence, and J. A. Screen (2016), Modeling the arctic freshwater system and its integration in the global system: Lessons learned and future challenges, *Journal of Geophysical Research: Biogeosciences*, *121*(3), 540–566.

Liu, X., R. C. Easter, S. J. Ghan, R. Zaveri, P. Rasch, X. Shi, J.-F. Lamarque, A. Gettelman, H. Morrison, F. Vitt, A. Conley, S. Park, R. Neale, C. Hannay, A. M. L. Ekman, P. Hess, N. Mahowald, W. Collins, M. J. Iacono, C. S. Bretherton, M. G. Flanner, and D. Mitchell (2012), Toward a minimal representation of aerosols in climate models: description and evaluation in the Community Atmosphere Model CAM5, *Geoscientific Model Development*, *5*(3), 709–739, doi:10.5194/gmd-5-709-2012.

Liu, X., P. L. Ma, H. Wang, S. Tilmes, B. Singh, R. C. Easter, S. J. Ghan, and P. J. Rasch (2016), Description and evaluation of a new four-mode version of the modal aerosol module (MAM4) within version 5.3 of the community atmosphere model, *Geosci. Model Dev.*, *9*(2), 505–522, doi:10.5194/gmd-9-505-2016.

Loeb, N. G., B. A. Wielicki, D. R. Doelling, G. L. Smith, D. F. Keyes, S. Kato, N. Manalo-Smith, and T. Wong (2009), Toward optimal closure of the earth's top-of-atmosphere radiation budget, *Journal of Climate*, *22*(3), 748–766, doi:10.1175/2008jcli2637.1.

Matthes, K., B. Funke, T. Kruschke, and S. Wahl (2017a), input4MIPs.SOLARIS-HEPPA.solar.CMIP.SOLARIS-HEPPA-3-2, doi:10.22033/ESGF/input4MIPs.1122.

Matthes, K., B. Funke, M. E. Andersson, L. Barnard, J. Beer, P. Charbonneau, M. A. Clilverd, T. Dudok de Wit, M. Haberreiter, A. Hendry, C. H. Jackman, M. Kretzschmar, T. Kruschke, M. Kunze, U. Langematz, D. R. Marsh, A. C. Maycock, S. Misios, C. J. Rodger, A. A. Scaife, A. SeppÃďlÃď, M. Shangguan, M. Sinnhuber, K. Tourpali, I. Usoskin, M. van de Kamp, P. T. Verronen, and S. Versick (2017b), Solar forcing for CMIP6 (v3.2), *Geosci. Model Dev.*, *10*(6), 2247–2302, doi:10.5194/gmd-10-2247-2017.

McGregor, H., M. J. Fischer, M. Gagan, D. Fink, S. J. Phipps, H. Wong, and C. Woodroffe (2013), A weak El Niño/Southern Oscillation with delayed seasonal growth around 4,300 years ago, *Nature Geoscience*, *6*(11), 949.

McPhaden, M. J., X. Zhang, H. H. Hendon, and M. C. Wheeler (2006), Large scale dynamics and MJO forcing of ENSO variability, *Geophysical Research Letters*, *33*(16), doi:10.1029/2006GL026786.

Meier, W., F. Fetterer, M. Savoie, S. Mallory, R. Duerr, and J. Stroeve (2017), NOAA/NSIDC Climate Data Record of Passive Microwave Sea Ice Concentration, Version 3, *Electronic Media*, doi:10.7265/N59P2ZTG.

Meinshausen, M., and E. Vogel (2016), input4MIPs.UoM.GHGConcentrations.CMIP.UoM-CMIP-1-2-0, doi:10.22033/ESGF/input4MIPs.1118.

Meinshausen, M., E. Vogel, A. Nauels, K. Lorbacher, N. Meinshausen, D. M. Etheridge, P. J. Fraser, S. A. Montzka, P. J. Rayner, C. M. Trudinger, P. B. Krummel, U. Beyerle, J. G. Canadell, J. S. Daniel, I. G. Enting, R. M. Law, C. R. Lunder, S. O'Doherty, R. G. Prinn, S. Reimann, M. Rubino, G. J. M. Velders, M. K. Vollmer, R. H. J. Wang, and R. Weiss (2017), Historical greenhouse gas concentrations for climate modelling (CMIP6), *Geosci. Model Dev.*, *10*(5), 2057–2116, doi:10.5194/gmd-10-2057-2017.

Menary, M. B., T. Kuhlbrodt, J. Ridley, M. B. Andrews, O. B. Dimdore-Miles, J. Deshayes, R. Eade, L. Gray, S. Ineson, J. Mignot, et al. (2018), Preindustrial control simulations with HadGEM3-GC3. 1 for cmip6, *Journal of Advances in Modeling Earth Systems*.

Morice, C. P., J. J. Kennedy, N. A. Rayner, and P. D. Jones (2012), Quantifying uncertainties in global and regional temperature change using an ensemble of observational estimates: The HadCRUT4 data set, *Journal of Geophysical Research: Atmospheres*, *117*(D8), n/a–n/a, doi:10.1029/2011jd017187.

Morrison, H., and A. Gettelman (2008), A new two-moment bulk stratiform cloud microphysics scheme in the Community Atmosphere Model, version 3 (CAM3). Part I: Description and numerical tests, *Journal of Climate*, *21*, 3642–3659, doi:10.1175/2008JCLI2105.1.

Naughten, K. A., B. K. Galton-Fenzi, K. J. Meissner, M. H. England, G. B. Brassington, F. Colberg, T. Hattermann, and J. B. Debernard (2017), Spurious sea ice formation caused by oscillatory ocean tracer advection schemes, *Ocean Modelling*, *116*, 108–117, doi:10.1016/j.ocemod.2017.06.010.

Newman, M., A. T. Wittenberg, L. Cheng, G. P. Compo, and C. A. Smith (2018), The extreme 2015/16 el niño, in the context of historical climate variability and change, *Bulletin of the American Meteorological Society*, *99*(1), S16–S20.

Oleson, K. W., D. M. Lawrence, G. B. Bonan, B. Drewniak, M. Huang, C. D. Koven, S. Levis, F. Li, W. J. Riley, Z. M. Subin, S. C. Swenson, P. E. Thornton, A. Bozbiyik, R. Fisher, C. L. Heald, E. Kluzek, J.-F. Lamarque, P. J. Lawrence, L. R. Leung, W. Lipscomb, S. Muszala, D. M. Ricciuto, W. Sacks, Y. Sun, J. Tang, and Z.-L. Yang (2013), Technical description of version 4.5 of the community land model (clm), *Tech. Rep. NCAR/TN-503+STR*, National Center for Atmospheric Research, Boulder, Colorado, USA.

Padilla, L. E., G. K. Vallis, and C. W. Rowley (2011), Probabilistic estimates of transient climate sensitivity subject to uncertainty in forcing and natural variability, *Journal of Climate*, *24*(21), 5521–5537, doi:10.1175/2011jcli3989.1.

Petersen, M. R., D. W. Jacobsen, T. D. Ringler, M. W. Hecht, and M. E. Maltrud (2015), Evaluation of the arbitrary Lagrangian–Eulerian vertical coordinate method in the MPAS-Ocean model, *Ocean Modelling*, *86*, 93–113, doi:10.1016/j.ocemod.2014.12.004.

Qian, Y., H. Wan, B. Yang, J.-C. Golaz, B. Harrop, Z. Hou, V. E. Larson, L. R. Leung, G. Lin, W. Lin, P.-L. Ma, H.-Y. Ma, P. Rasch, B. Singh, H. Wang, S. Xie, and K. Zhang (2018), Parametric sensitivity and uncertainty quantification in the version 1 of E3SM Atmosphere Model based on short Perturbed Parameters Ensemble simulations, *Journal of Geophysical Research: Atmospheres*, doi:10.1029/2018jd028927.

Rasch, P. J., S. Xie, P.-L. Ma, W. Lin, H. Wang, Q. Tang, S. M. Burrows, P. Caldwell, K. Zhang, R. C. Easter, P. Cameron-Smith, B. Singh, H. Wan, J.-C. Golaz, B. E. Harrop, E. Roesler, J. Bacmeister, V. E. Larson, K. J. Evans, Y. Qian, M. Taylor, L. Leung, Y. Zhang, L. Brent, M. Branstetter, C. Hannay, S. Mahajan, A. Mametjanov, R. Neale, J. H. Richter, J.-H. Yoon, C. S. Zender, D. Bader, M. Flanner, J. G. Foucar, R. Jacob, N.Keen, S. A. Klein, X. Liu, A. G. Salinger, M. Shrivastava, and Y. Yang (2019), An Overview of the Atmospheric Component of the Energy Exascale Earth System Model, *Journal of Advances in Modeling Earth Systems*, joint submission to AGU Special Collection on E3SM.

Rayner, N., D. Parker, C. Folland, E. Horton, L. Alexander, and D. Rowell (2003), The global sea-ice and sea surface temperature (HadISST) data sets, *J. Geophys. Res.*

Reckinger, S. M., M. R. Petersen, and S. J. Reckinger (2015), A study of overflow simulations using MPAS-Ocean: Vertical grids, resolution, and viscosity, *Ocean Modelling*, *96*, 291–313, doi:10.1016/j.ocemod.2015.09.006.

Ringler, T., J. Thuburn, J. Klemp, and W. Skamarock (2010), A unified approach to energy conservation and potential vorticity dynamics for arbitrarily-structured C-grids, *Journal of Computational Physics*, *229*(9), 3065–3090, doi:10.1016/j.jcp.2009.12.007.

Ringler, T., M. Petersen, R. L. Higdon, D. Jacobsen, P. W. Jones, and M. Maltrud (2013), A multi-resolution approach to global ocean modeling, *Ocean Modelling*, *69*, 211–232, doi:10.1016/j.ocemod.2013.04.010.

Sallée, J.-B., E. Shuckburgh, N. Bruneau, A. J. Meijers, T. J. Bracegirdle, and Z. Wang (2013), Assessment of southern ocean mixed-layer depths in cmip5 models: Historical bias and forcing response, *Journal of Geophysical Research: Oceans*, *118*(4), 1845–1862.

Schmidt, G. A., C. M. Bitz, U. Mikolajewicz, and L.-B. Tremblay (2004), Ice–ocean boundary conditions for coupled models, *Ocean Modelling*, *7*(1-2), 59–74.

Schmidt, G. A., D. Bader, L. J. Donner, G. S. Elsaesser, J.-C. Golaz, C. Hannay, A. Molod, R. B. Neale, and S. Saha (2017), Practice and philosophy of climate model tuning across six US modeling centers, *Geoscientific Model Development*, *10*(9), 3207–3223, doi:10.5194/gmd-10-3207-2017.

Shrivastava, M., R. C. Easter, X. Liu, A. Zelenyuk, B. Singh, K. Zhang, P.-L. Ma, D. Chand, S. Ghan, J. L. Jimenez, Q. Zhang, J. Fast, P. J. Rasch, and P. Tiitta (2015), Global transformation and fate of SOA: Implications of low-volatility SOA and gas-phase fragmentation reactions, *Journal of Geophysical Research: Atmospheres*, *120*(9), 4169–4195, doi:10.1002/2014JD022563.

Skamarock, W. C., and A. Gassmann (2011), Conservative transport schemes for spherical geodesic grids: High-order flux operators for ODE-based time integration, *Mon. Weather Rev.*, *139*, 2962–2975, doi:10.1175/MWR-D-10-05056.1.

Smeed, D., G. McCarth, B. Moat, W. Johns, M. Baringer, and C. Meinen (2017), Atlantic meridional overturning circulation observed by the RAPID-MOCHA-WBTS (RAPID-Meridional Overturning Circulation and Heatflux Array-Western Boundary Time Series) array at 26N from 2004 to 2017, British Oceanographic Data Centre - Natural Environment Research Council, UK, doi:10.5285/5acfd143-1104-7b58-e053-6c86abc0d94b.

Smith, T. M., R. W. Reynolds, T. C. Peterson, and J. Lawrimore (2008), Improvements to NOAA's historical merged land–ocean surface temperature analysis (1880–2006), *Journal of Climate*, *21*(10), 2283–2296, doi:10.1175/2007jcli2100.1.

Sobel, A. H., and E. D. Maloney (2000), Effect of enso and the mjo on western north pacific tropical cyclones, *Geophysical Research Letters*, *27*(12), 1739–1742, doi:10.1029/1999GL011043.

Soden, B. J., I. M. Held, R. Colman, K. M. Shell, J. T. Kiehl, and C. A. Shields (2008), Quantifying climate feedbacks using radiative kernels, *Journal of Climate*, *21*(14), 3504–3520, doi:10.1175/2007jcli2110.1.

Steele, M., R. Morley, and W. Ermold (2001), Phc: A global ocean hydrography with a high-quality arctic ocean, *Journal of Climate*, *14*(9), 2079–2087.

Stephens, G. L., J. Li, M. Wild, C. A. Clayson, N. Loeb, S. Kato, T. L'Ecuyer, P. W. Stackhouse, M. Lebsock, and T. Andrews (2012), An update on earth's energy balance in light of the latest global observations, *Nature Geoscience*, *5*(10), 691–696, doi:10.1038/ngeo1580.

Stevens, B. (2015), Rethinking the lower bound on aerosol radiative forcing, *Journal of Climate*, *28*(12), 4794–4819, doi:10.1175/jcli-d-14-00656.1.

Stevenson, S. (2012), Significant changes to ENSO strength and impacts in the twenty-first century: Results from CMIP5, *Geophysical Research Letters*, *39*(17).

Stevenson, S., B. Fox-Kemper, M. Jochum, R. Neale, C. Deser, and G. Meehl (2012), Will there be a significant change to el niño in the twenty-first century?, *Journal of Climate*, *25*(6), 2129–2145.

Sun, Q., C. Miao, Q. Duan, H. Ashouri, S. Sorooshian, and K.-L. Hsu (2018), A review of global precipitation data sets: Data sources, estimation, and intercomparisons, *Reviews of Geophysics*, *56*(1), 79–107, doi:10.1002/2017rg000574.

Taylor, K. E., D. Williamson, and F. Zwiers (2000), The sea surface temperature and sea ice concentration boundary conditions for AMIP II simulations, *PCMDI Report 60,* https://pcmdi.llnl.gov/report/pdf/60.pdf, Program for Climate Model Diagnosis and Intercomparison, Lawrence Livermore National Laboratory.

Thuburn, J., T. D. Ringler, W. C. Skamarock, and J. B. Klemp (2009), Numerical representation of geostrophic modes on arbitrarily structured C-grids, *Journal of Computational Physics*, *228*(22), 8321–8335, doi:10.1016/j.jcp.2009.08.006.

Tilling, R. L., A. Ridout, A. Shepherd, and D. J. Wingham (2015), Increased Arctic sea ice volume after anomalously low melting in 2013, *Nature Geoscience*, *8*(8), 643–646, doi:10.1038/ngeo2489.

Torrence, C., and G. P. Compo (1998), A practical guide to wavelet analysis, *Bulletin of the American Meteorological society*, *79*(1), 61–78.

Trenberth, K. E., J. T. Fasullo, and J. Kiehl (2009), Earth's global energy budget, *Bulletin of the American Meteorological Society*, *90*(3), 311–324, doi:10.1175/2008bams2634.1.

Turner, A. K., and E. C. Hunke (2015), Impacts of a mushy-layer thermodynamic approach in global sea-ice simulations using the CICE sea-ice model, *Journal of Geophysical Research: Oceans*, *120*(2), 1253–1275, doi:10.1002/2014JC010358.

Turner, A. K., E. C. Hunke, and C. M. Bitz (2013), Two modes of sea-ice gravity drainage: A parameterization for large-scale modeling, *Journal of Geophysical Research: Oceans*, *118*(5), 2279–2294, doi:10.1002/jgrc.20171.

Ullrich, P. A., and M. A. Taylor (2015), Arbitrary-order conservative and consistent remapping and a theory of linear maps: Part i, *Monthly Weather Review*, *143*(6), 2419–2440.

U.S. Department of Energy (2013), U.S. Energy Sector Vulnerabilities to Climate Change and Extreme Weather, *Tech. Rep. DOE/PI-0013,* https://www.energy.gov/sites/prod/files/2013/07/f2/20130710-Energy-Sector-Vulnerabilities-Report.pdf, U.S. Department of Energy.

van Marle, M. J., S. Kloster, B. I. Magi, J. R. Marlon, A.-L. Daniau, R. D. Field, A. Arneth, M. Forrest, S. Hantson, N. M. Kehrwald, W. Knorr, G. Lasslop, F. Li, S. Mangeon, C. Yue, J. W. Kaiser, and G. R. van der Werf (2016), Biomass burning emissions for cmip6 (v1.2), doi:10.22033/ESGF/input4MIPs.1117.

van Marle, M. J. E., S. Kloster, B. I. Magi, J. R. Marlon, A. L. Daniau, R. D. Field, A. Arneth, M. Forrest, S. Hantson, N. M. Kehrwald, W. Knorr, G. Lasslop, F. Li, S. Mangeon, C. Yue, J. W. Kaiser, and G. R. van der Werf (2017), Historic global biomass burning emissions for CMIP6 (BB4CMIP) based on merging satellite observations with proxies and fire models (1750-2015), *Geosci. Model Dev.*, *10*(9), 3329–3357, doi:10.5194/gmd-10-3329-2017.

Van Oldenborgh, G. J., S. Philip, and M. Collins (2005), El niño in a changing climate: a multi-model study, *Ocean Science*, *1*(2), 81–95.

Van Roekel, L., A. J. Adcroft, G. Danabasoglu, S. M. Griffies, B. Kauffman, W. Large, M. Levy, B. G. Reichl, T. Ringler, and M. Schmidt (2018), The kpp boundary layer scheme for the ocean: Revisiting its formulation and benchmarking one-dimensional simulations relative to les, *Journal of Advances in Modeling Earth Systems*, *0*(0), doi: 10.1029/2018MS001336.

Vitart, F. (2017), Madden-Julian oscillation prediction and teleconnections in the s2s database, *Quarterly Journal of the Royal Meteorological Society*, *143*(706), 2210–2220, doi:10.1002/qj.3079.

Waliser, D. E., K. M. Lau, W. Stern, and C. Jones (2003), Potential predictability of the maddenâĂŞjulian oscillation, *Bulletin of the American Meteorological Society*, *84*(1), 33–50, doi:10.1175/BAMS-84-1-33.

Wang, H., S. A. Legg, and R. W. Hallberg (2015), Representations of the nordic seas overflows and their large scale climate impact in coupled models, *Ocean Modelling*, *86*, 76–92.

Wang, H., S. Legg, and R. Hallberg (2018), The effect of arctic freshwater pathways on north atlantic convection and the atlantic meridional overturning circulation, *Journal of Climate*, *31*(13), 5165–5188.

Wild, M., D. Folini, C. Schär, N. Loeb, E. G. Dutton, and G. König-Langlo (2012), The global energy balance from a surface perspective, *Climate Dynamics*, *40*(11-12), 3107–3134, doi:10.1007/s00382-012-1569-8.

Wittenberg, A. T. (2009), Are historical records sufficient to constrain enso simulations?, *Geophysical Research Letters*, *36*(12).

Xie, S., W. Lin, P. J. Rasch, P.-L. Ma, R. Neale, V. E. Larson, Y. Qian, P. A. Bogenschutz, P. Caldwell, P. Cameron-Smith, J.-C. Golaz, S. Mahajan, B. Singh, Q. Tang, H. Wang, J.-H. Yoon, K. Zhang, and Y. Zhang (2018), Understanding cloud and convective characteristics in version 1 of the E3SM Atmosphere Model, *Journal of Advances in Modeling Earth Systems*, doi:10.1029/2018ms001350.

Zender, C. S. (2008), Analysis of self-describing gridded geoscience data with netCDF operators (NCO), *Environmental Modelling & Software*, *23*(10-11), 1338–1342, doi:10.1016/j.envsoft.2008.03.004.

Zender, C. S. (2018), netCDF Operators (NCO) version 4.7.8, doi:10.5281/zenodo.595745.

Zhang, G., and N. A. McFarlane (1995), Sensitivity of climate simulations to the parameterization of cumulus convection in the Canadian climate centre general circulation model, *Atmosphere-Ocean*, *33*(3), 407–446, doi:10.1080/07055900.1995.9649539.

Zhang, H.-M., B. Huang, J. Lawrimore, M. Menne, and T. M. Smith (2015), NOAA global surface temperature dataset, version 4.0, doi:10.7289/v5fn144h.

Zhang, K., P. J. Rasch, M. A. Taylor, H. Wan, R. Leung, P.-L. Ma, J.-C. Golaz, J. Wolfe, W. Lin, B. Singh, S. Burrows, J.-H. Yoon, H. Wang, Y. Qian, Q. Tang, P. Caldwell, and S. Xie (2018), Impact of numerical choices on water conservation in the E3SM Atmosphere Model version 1 (EAMv1), *Geoscientific Model Development*, *11*(5), 1971–1988, doi:10.5194/gmd-11-1971-2018.

Zhao, M., J.-C. Golaz, I. M. Held, H. Guo, V. Balaji, R. Benson, J.-H. Chen, X. Chen, L. J. Donner, J. P. Dunne, K. Dunne, J. Durachta, S.-M. Fan, S. M. Freidenreich, S. T. Garner, P. Ginoux, L. M. Harris, L. W. Horowitz, J. P. Krasting, A. R. Langenhorst, Z. Liang, P. Lin, S.-J. Lin, S. L. Malyshev, E. Mason, P. C. D. Milly, Y. Ming, V. Naik, F. Paulot, D. Paynter, P. Phillipps, A. Radhakrishnan, V. Ramaswamy, T. Robinson, D. Schwarzkopf, C. J. Seman, E. Shevliakova, Z. Shen, H. Shin, L. G. Silvers, J. R. Wilson, M. Winton, A. T. Wittenberg, B. Wyman, and B. Xiang (2018), The GFDL global atmosphere and land model AM4.0/LM4.0: 2. model description, sensitivity studies, and tuning strategies, *Journal of Advances in Modeling Earth Systems*, *10*(3), 735–769, doi:10.1002/2017ms001209.

Figure 1.

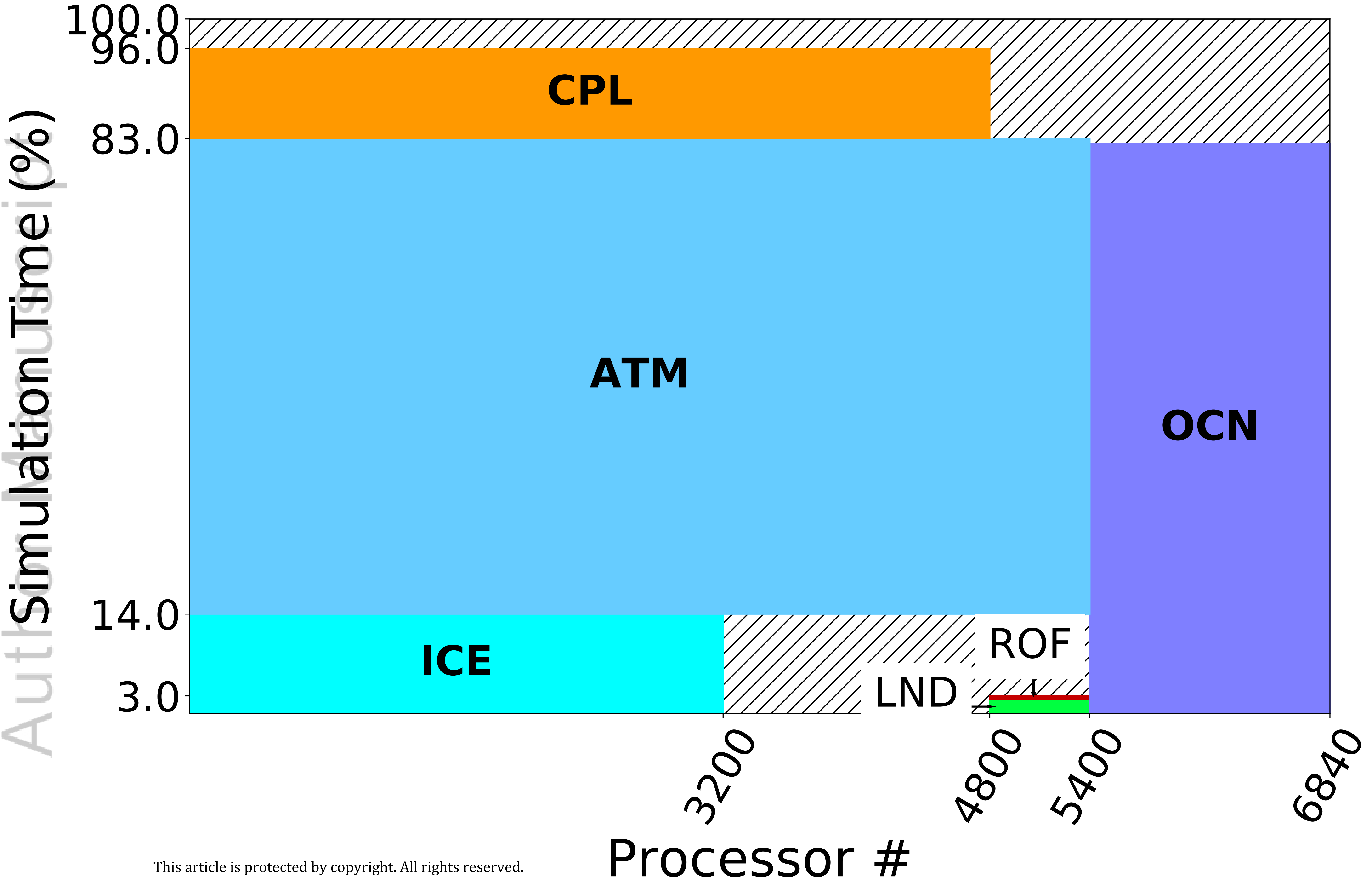

100.0
96.0
83.0
14.0
3.0
CPL
ATM
OCN
ICE
ROF
LND
3200
4800
5400
6840
Simulation Time (%)
Processor #

Figure 2.

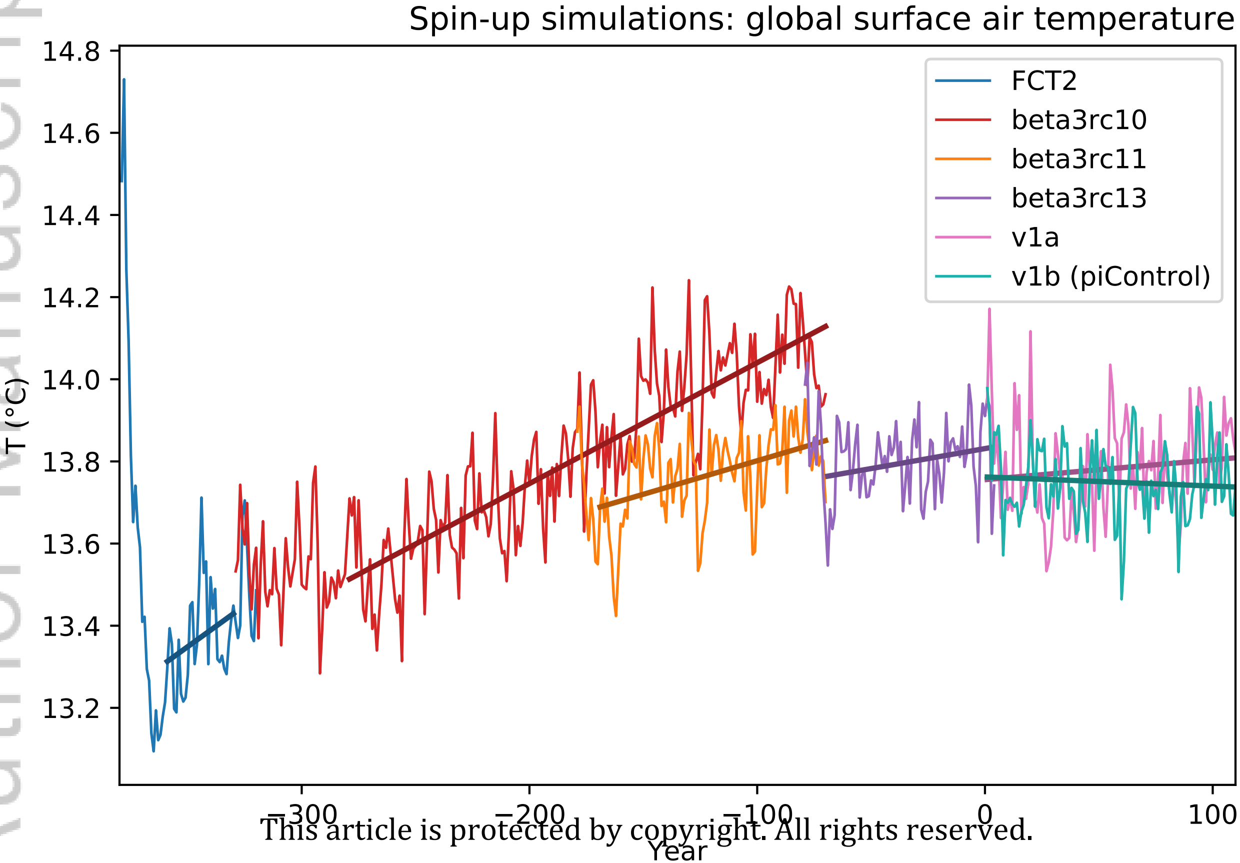
Spin-up simulations: global surface air temperature
T (°C)
14.8
14.6
14.4
14.2
14.0
13.8
13.6
13.4
13.2
−300
−200
−100
0
100
Year
FCT2
beta3rc10
beta3rc11
beta3rc13
v1a
v1b (piControl)

Figure 3.

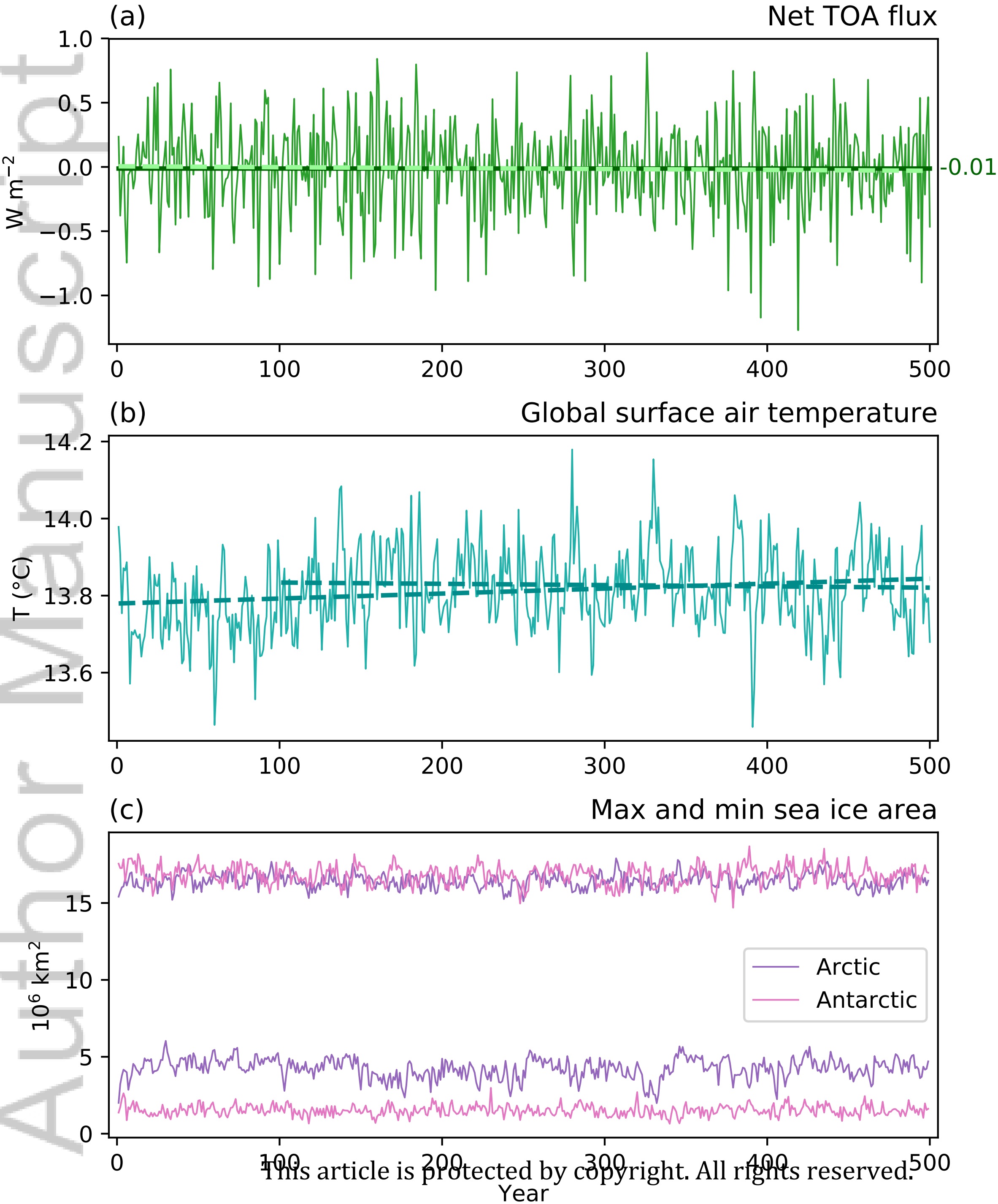
(a)
Net TOA flux
W m^{-2}
1.0
0.5
0.0
−0.5
−1.0
-0.01
0
100
200
300
400
500
(b)
Global surface air temperature
T (°C)
14.2
14.0
13.8
13.6
0
100
200
300
400
500
(c)
Max and min sea ice area
10^6 km^2
15
10
5
0
Arctic
Antarctic
0
100
200
300
400
500
Year

Figure 4.

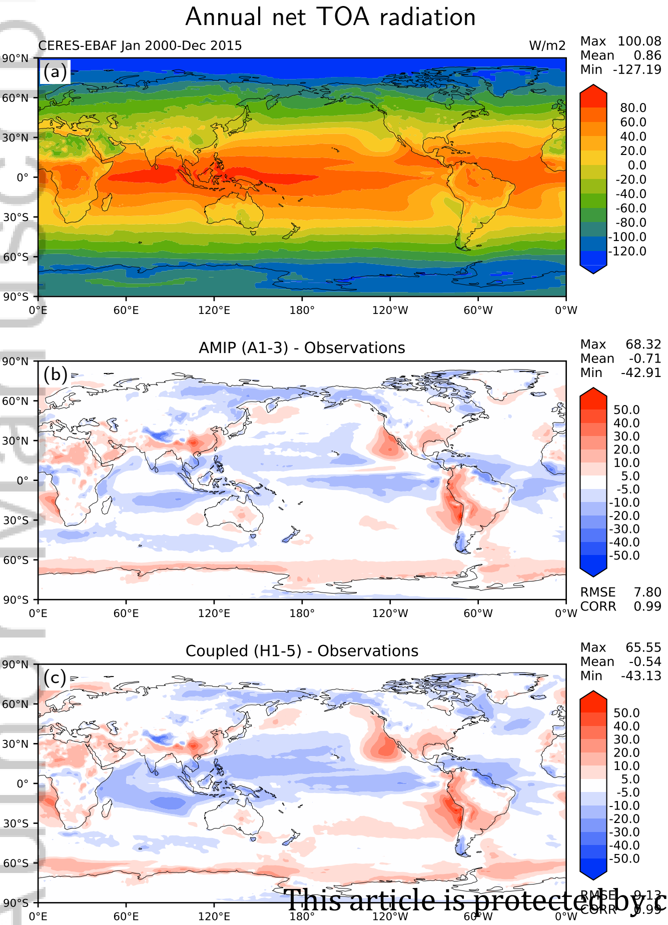
Annual net TOA radiation
CERES-EBAF Jan 2000-Dec 2015
W/m2
(a)
Max 100.08
Mean 0.86
Min -127.19
80.0
60.0
40.0
20.0
0.0
-20.0
-40.0
-60.0
-80.0
-100.0
-120.0
AMIP (A1-3) - Observations
(b)
Max 68.32
Mean -0.71
Min -42.91
50.0
40.0
30.0
20.0
10.0
5.0
-5.0
-10.0
-20.0
-30.0
-40.0
-50.0
RMSE 7.80
CORR 0.99
Coupled (H1-5) - Observations
(c)
Max 65.55
Mean -0.54
Min -43.13
50.0
40.0
30.0
20.0
10.0
5.0
-5.0
-10.0
-20.0
-30.0
-40.0
-50.0
90°N
60°N
30°N
0°
30°S
60°S
90°S
0°E
60°E
120°E
180°
120°W
60°W
0°W

Figure 5.

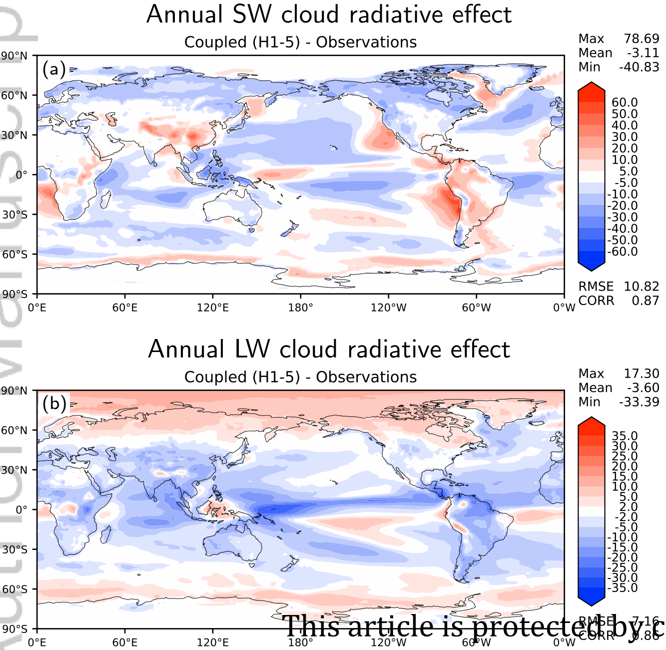
Annual SW cloud radiative effect
Coupled (H1-5) - Observations
(a)
Max 78.69
Mean -3.11
Min -40.83
60.0 50.0 40.0 30.0 20.0 10.0 5.0 -5.0 -10.0 -20.0 -30.0 -40.0 -50.0 -60.0
RMSE 10.82
CORR 0.87
90°N 60°N 30°N 0° 30°S 60°S 90°S
0°E 60°E 120°E 180° 120°W 60°W 0°W
Annual LW cloud radiative effect
Coupled (H1-5) - Observations
(b)
Max 17.30
Mean -3.60
Min -33.39
35.0 30.0 25.0 20.0 15.0 10.0 5.0 2.0 -2.0 -5.0 -10.0 -15.0 -20.0 -25.0 -30.0 -35.0
90°N 60°N 30°N 0° 30°S 60°S 90°S
0°E 60°E 120°E 180° 120°W 60°W 0°W

Figure 6.

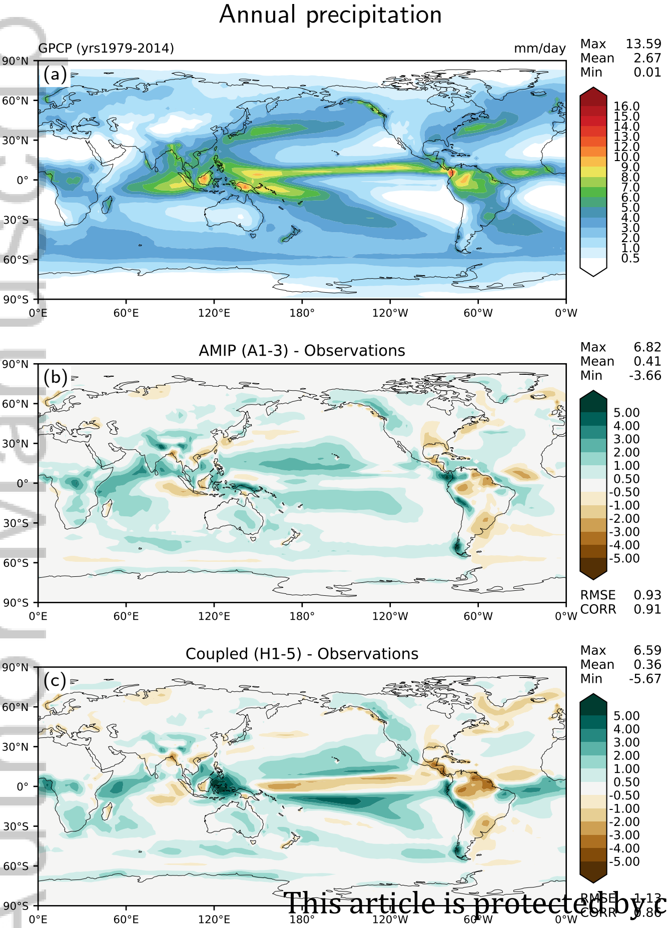
Annual precipitation
GPCP (yrs1979-2014)
mm/day
(a)
Max 13.59
Mean 2.67
Min 0.01
16.0
15.0
14.0
13.0
12.0
10.0
9.0
8.0
7.0
6.0
5.0
4.0
3.0
2.0
1.0
0.5
AMIP (A1-3) - Observations
(b)
Max 6.82
Mean 0.41
Min -3.66
5.00
4.00
3.00
2.00
1.00
0.50
-0.50
-1.00
-2.00
-3.00
-4.00
-5.00
RMSE 0.93
CORR 0.91
Coupled (H1-5) - Observations
(c)
Max 6.59
Mean 0.36
Min -5.67
5.00
4.00
3.00
2.00
1.00
0.50
-0.50
-1.00
-2.00
-3.00
-4.00
-5.00
RMSE 1.13
CORR 0.86
90°N
60°N
30°N
0°
30°S
60°S
90°S
0°E
60°E
120°E
180°
120°W
60°W
0°W

Figure 7.

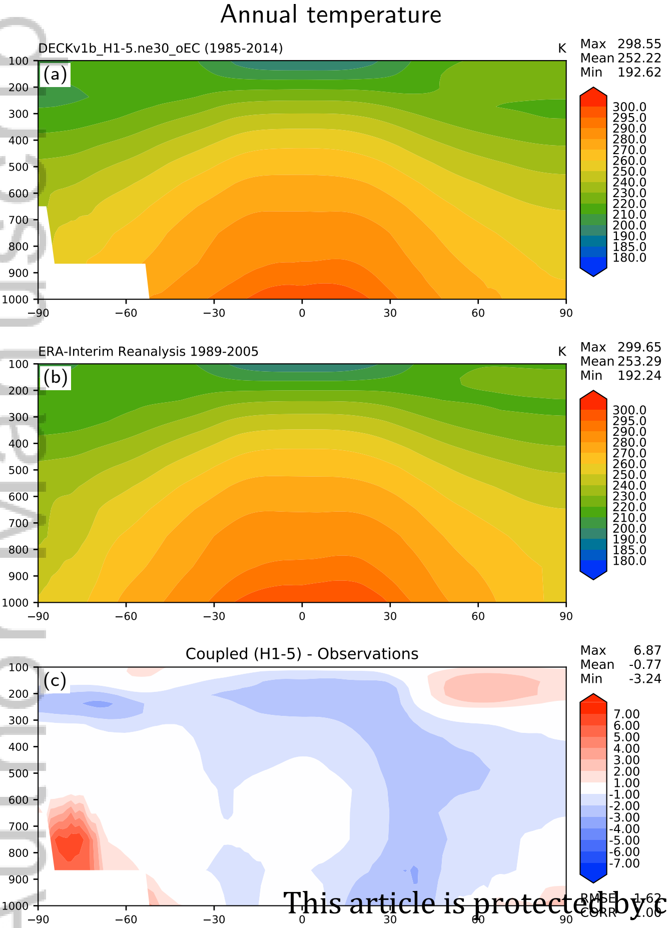
Annual temperature
DECKv1b_H1-5.ne30_oEC (1985-2014)
K
Max 298.55
Mean 252.22
Min 192.62
(a)
ERA-Interim Reanalysis 1989-2005
K
Max 299.65
Mean 253.29
Min 192.24
(b)
Coupled (H1-5) - Observations
Max 6.87
Mean -0.77
Min -3.24
(c)
RMSE 1.62
CORR 1.00

Figure 8.

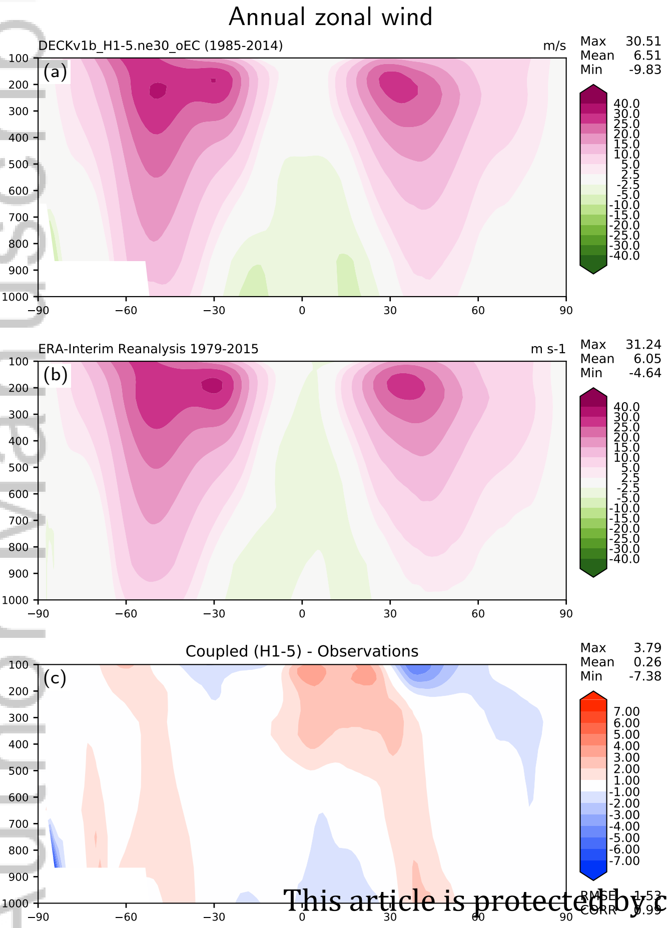

Annual zonal wind
DECKv1b_H1-5.ne30_oEC (1985-2014)
m/s
Max 30.51
Mean 6.51
Min -9.83
(a)
ERA-Interim Reanalysis 1979-2015
m s-1
Max 31.24
Mean 6.05
Min -4.64
(b)
Coupled (H1-5) - Observations
Max 3.79
Mean 0.26
Min -7.38
(c)
RMSE 1.53
CORR 0.99
40.0
30.0
25.0
20.0
15.0
10.0
5.0
2.5
-2.5
-5.0
-10.0
-15.0
-20.0
-25.0
-30.0
-40.0
7.00
6.00
5.00
4.00
3.00
2.00
1.00
-1.00
-2.00
-3.00
-4.00
-5.00
-6.00
-7.00
100
200
300
400
500
600
700
800
900
1000
−90
−60
−30
0
30
60
90

Figure 9.

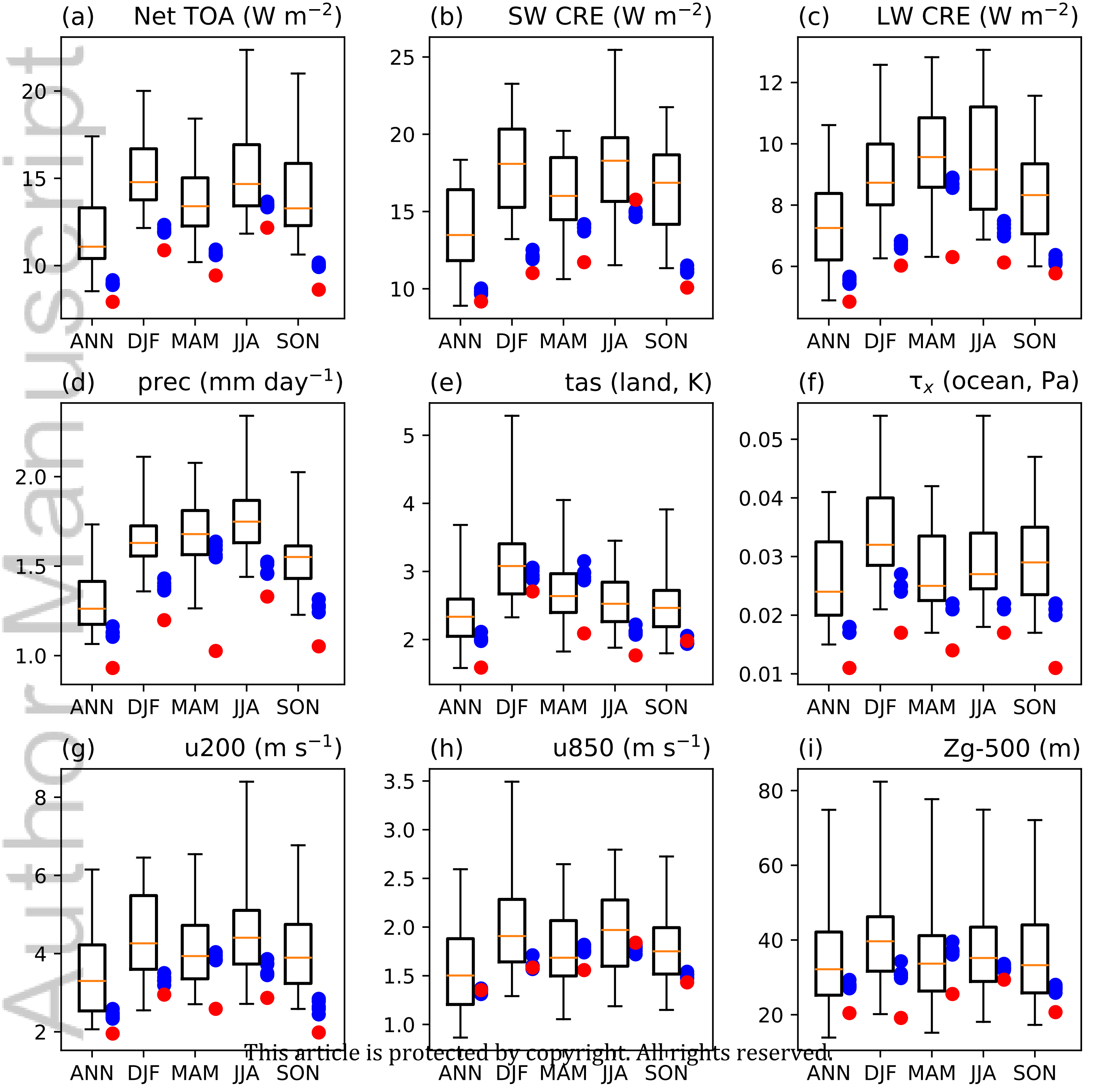

(a) Net TOA (W m^{-2})
(b) SW CRE (W m^{-2})
(c) LW CRE (W m^{-2})
(d) prec (mm day^{-1})
(e) tas (land, K)
(f) τ_x (ocean, Pa)
(g) u200 (m s^{-1})
(h) u850 (m s^{-1})
(i) Zg-500 (m)
ANN DJF MAM JJA SON

Figure 10.

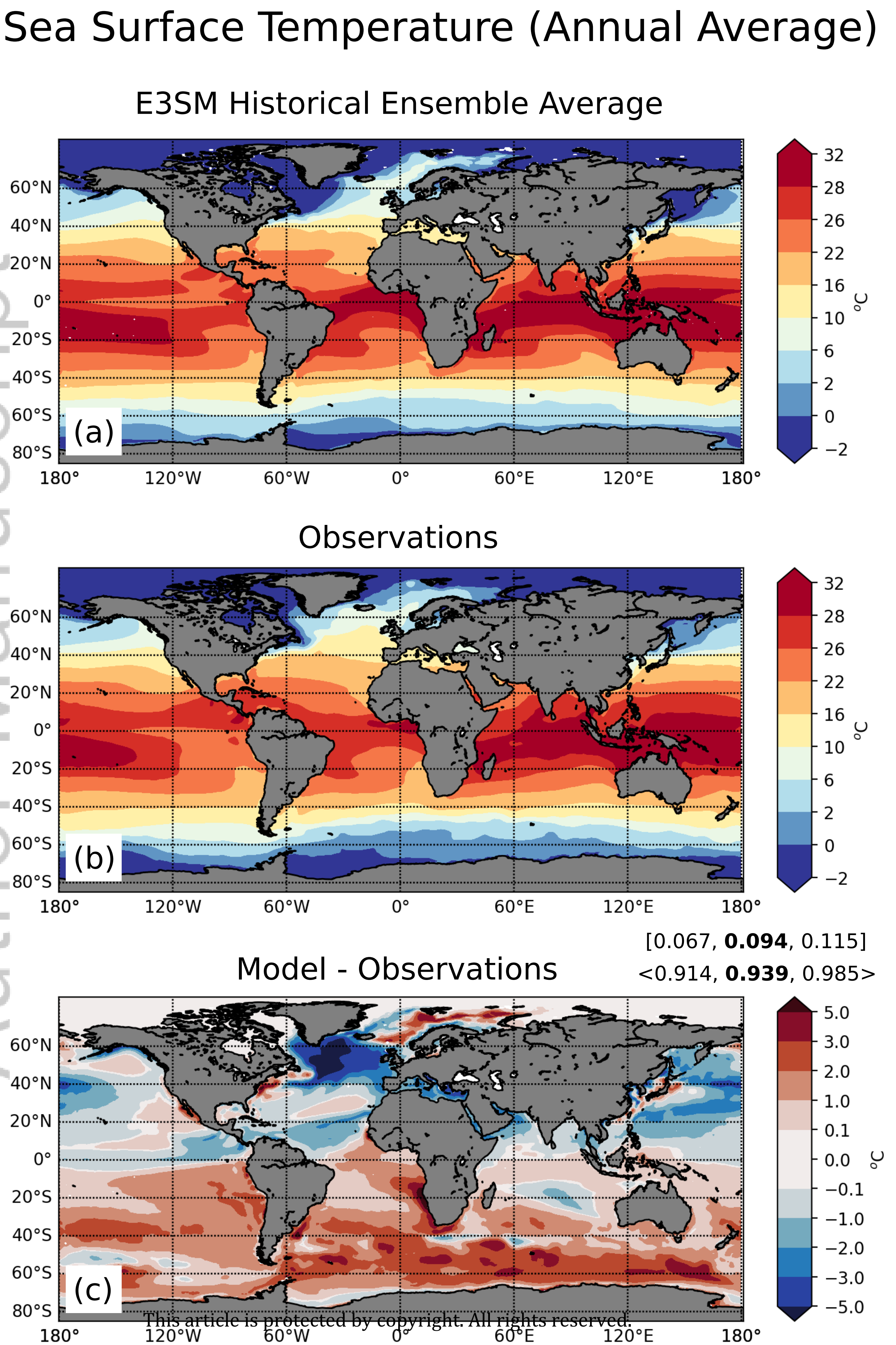
Sea Surface Temperature (Annual Average)
E3SM Historical Ensemble Average
(a)
Observations
(b)
[0.067, **0.094**, 0.115]
<0.914, **0.939**, 0.985>
Model - Observations
(c)
60°N
40°N
20°N
0°
20°S
40°S
60°S
80°S
180°
120°W
60°W
0°
60°E
120°E
180°
32
28
26
22
16
10
6
2
0
−2
°C
5.0
3.0
2.0
1.0
0.1
0.0
−0.1
−1.0
−2.0
−3.0
−5.0

Figure 11.

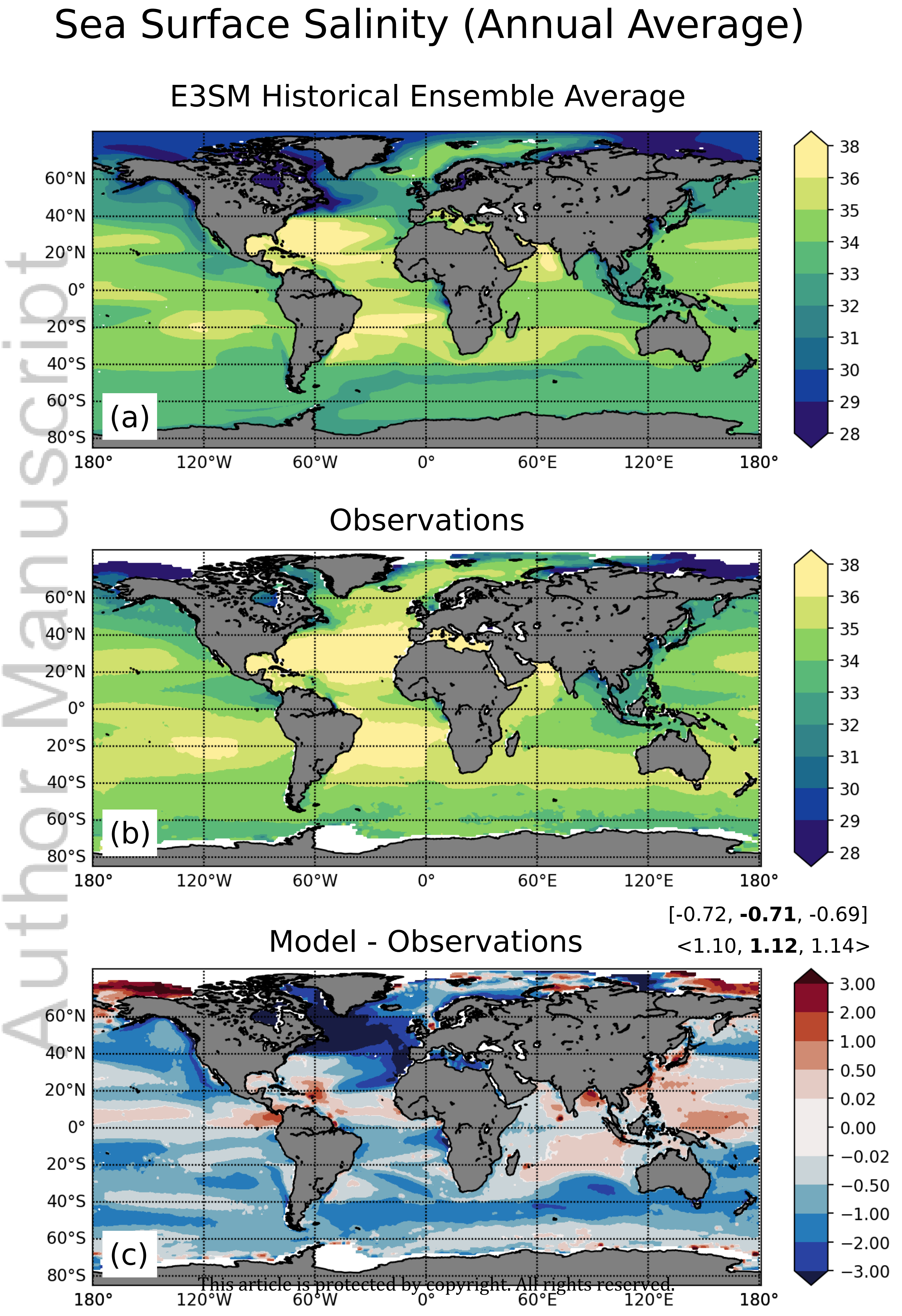
Sea Surface Salinity (Annual Average)
E3SM Historical Ensemble Average
(a)
Observations
(b)
[-0.72, **-0.71**, -0.69]
<1.10, **1.12**, 1.14>
Model - Observations
(c)
60°N
40°N
20°N
0°
20°S
40°S
60°S
80°S
180°
120°W
60°W
0°
60°E
120°E
180°
38
36
35
34
33
32
31
30
29
28
3.00
2.00
1.00
0.50
0.02
0.00
−0.02
−0.50
−1.00
−2.00
−3.00

Figure 12.

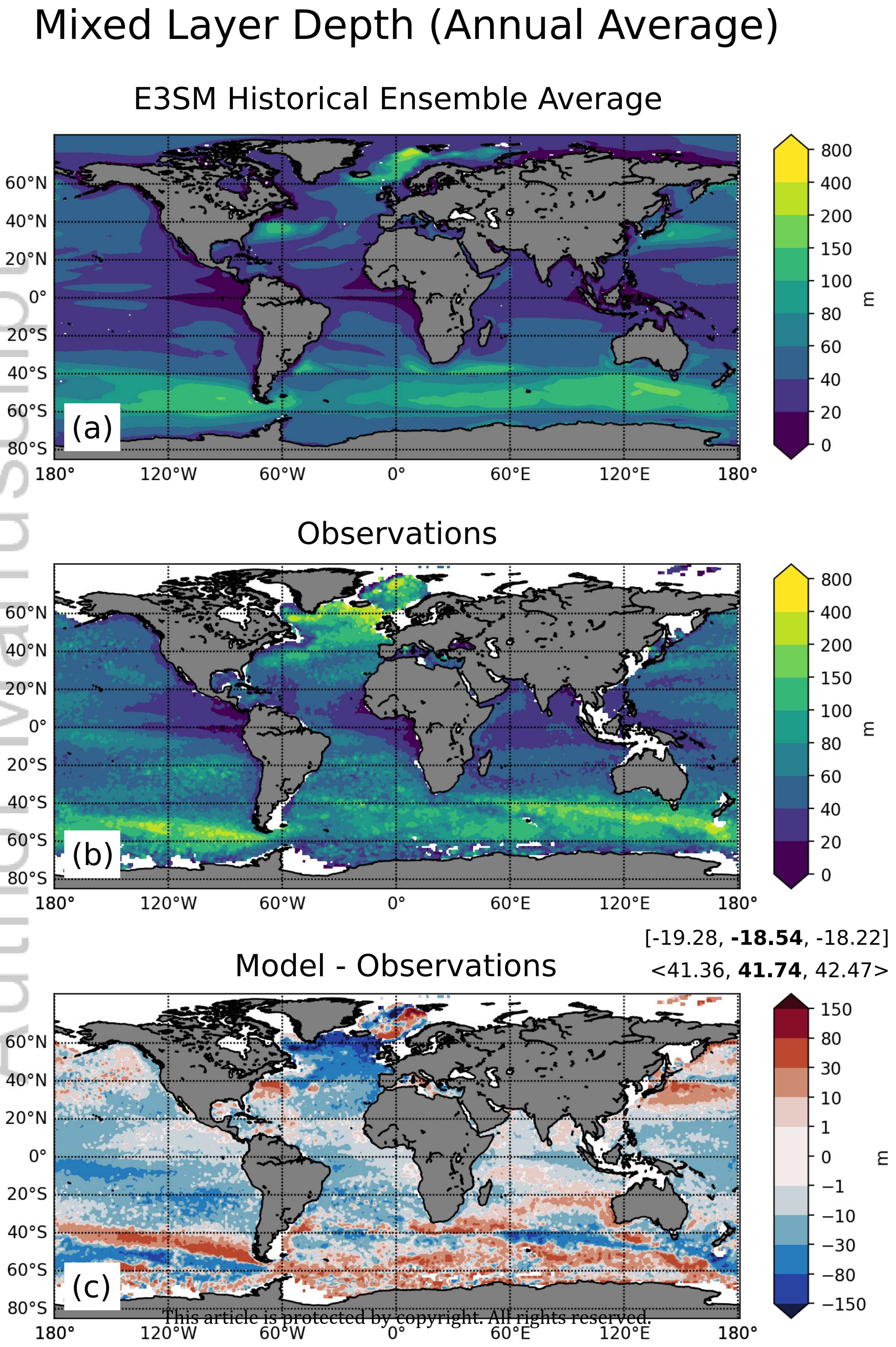

Mixed Layer Depth (Annual Average)
E3SM Historical Ensemble Average
(a)
Observations
(b)
Model - Observations
(c)
[-19.28, **-18.54**, -18.22]
<41.36, **41.74**, 42.47>
60°N
40°N
20°N
0°
20°S
40°S
60°S
80°S
180°
120°W
60°W
0°
60°E
120°E
180°
800
400
200
150
100
80
60
40
20
0
m
150
80
30
10
1
0
−1
−10
−30
−80
−150

Figure 13.

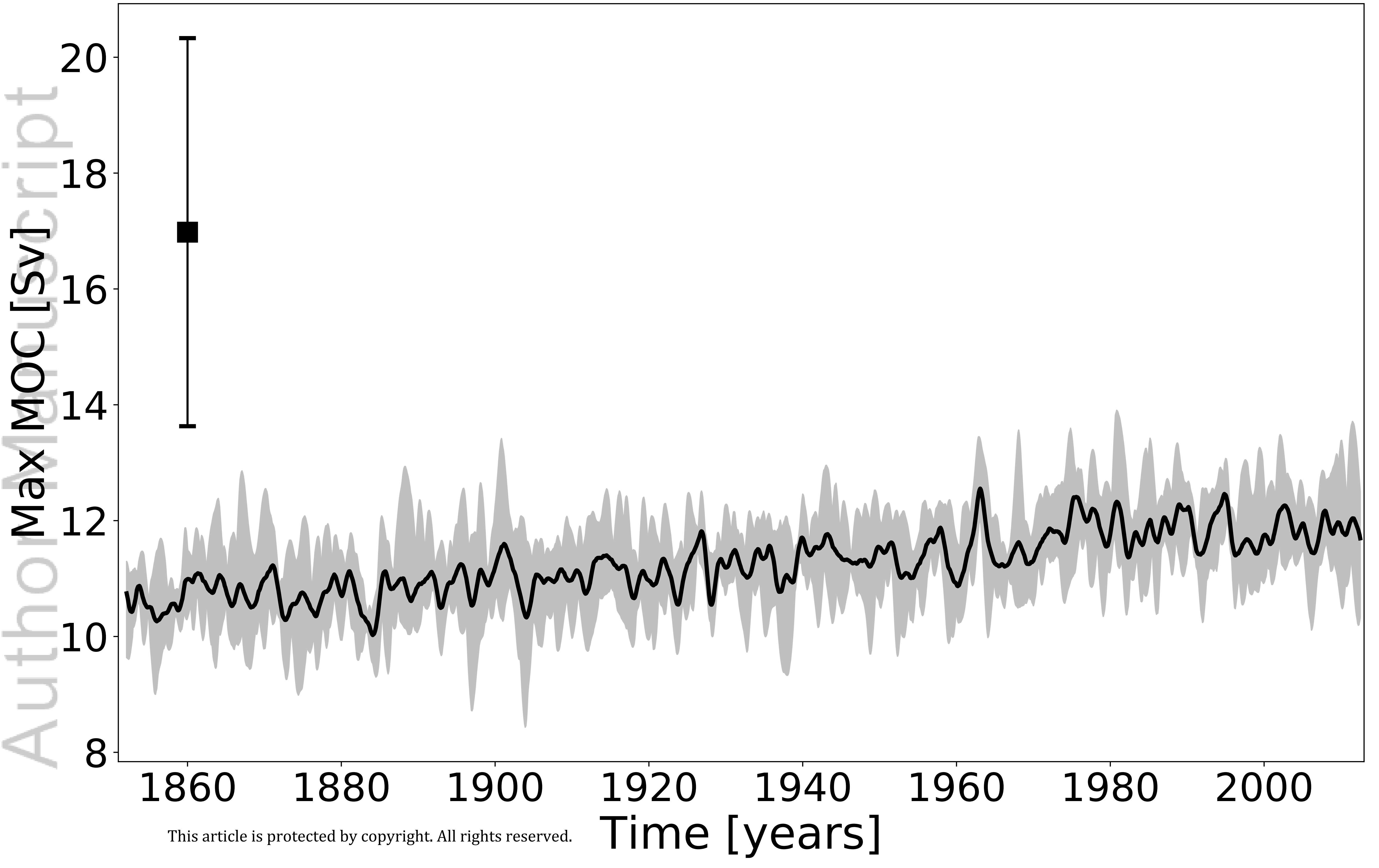
Max MOC [Sv]
20
18
16
14
12
10
8
1860
1880
1900
1920
1940
1960
1980
2000
Time [years]

Figure 14.

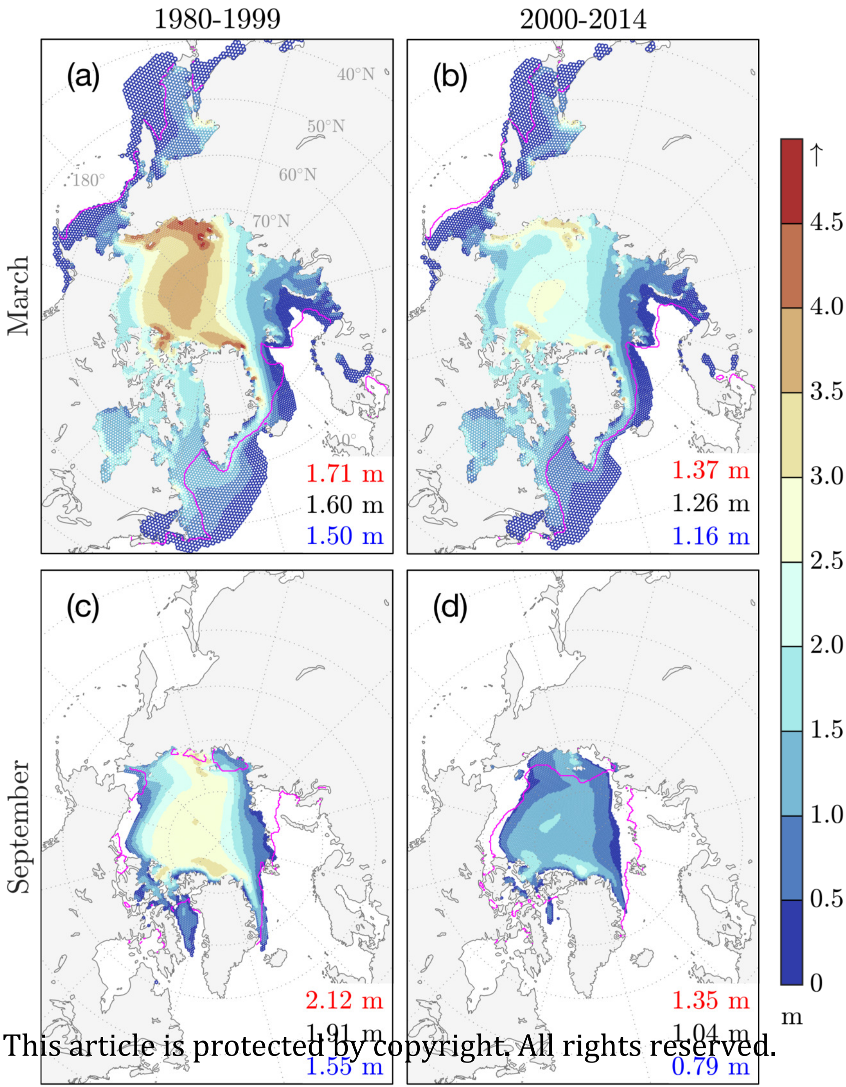
1980-1999
2000-2014
March
September
(a)
(b)
(c)
(d)
40°N
50°N
60°N
70°N
180°
1.71 m
1.60 m
1.50 m
1.37 m
1.26 m
1.16 m
2.12 m
1.91 m
1.55 m
1.35 m
1.04 m
0.79 m
↑
4.5
4.0
3.5
3.0
2.5
2.0
1.5
1.0
0.5
0
m

Figure 15.

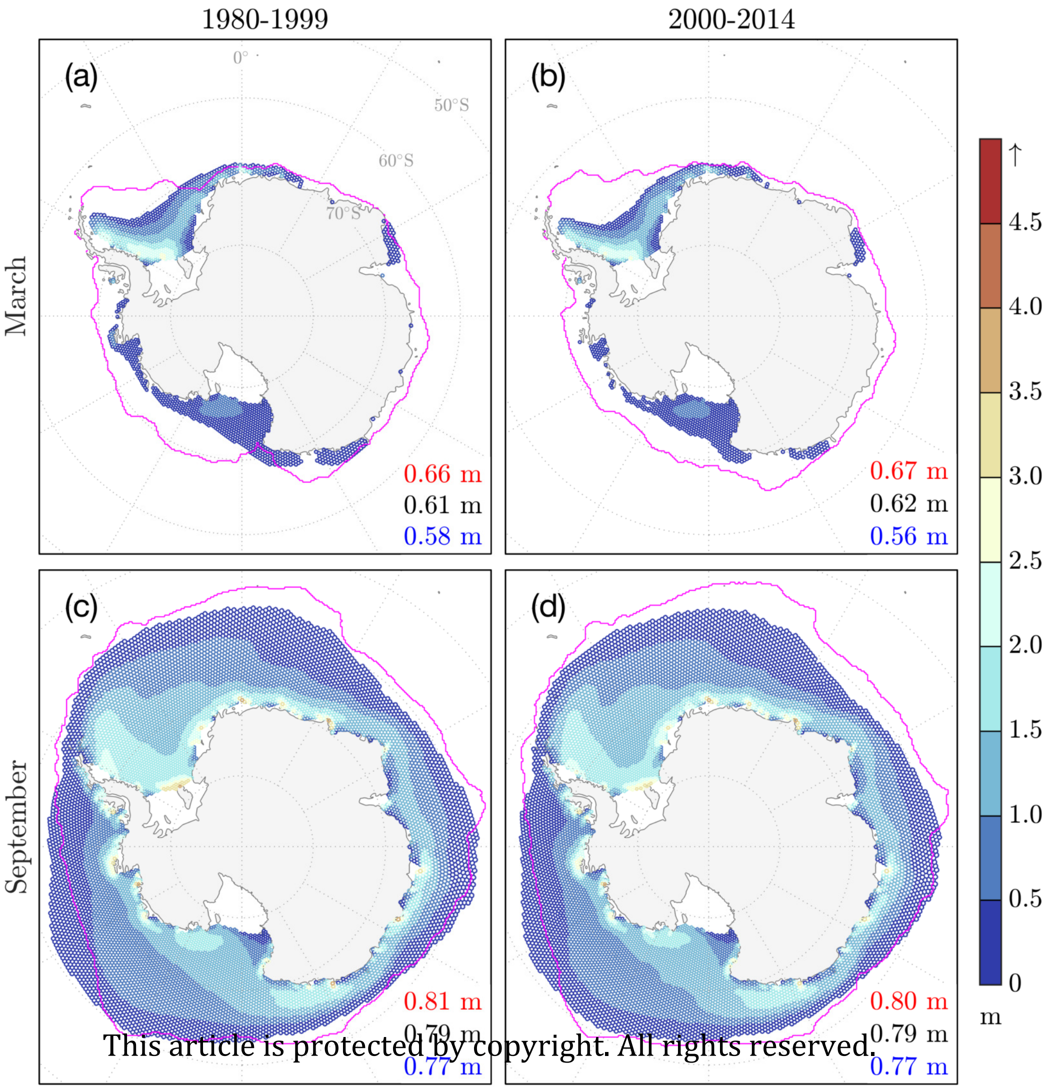
1980-1999
2000-2014
March
September
(a)
(b)
(c)
(d)
0°
50°S
60°S
70°S
0.66 m
0.61 m
0.58 m
0.67 m
0.62 m
0.56 m
0.81 m
0.79 m
0.77 m
0.80 m
0.79 m
0.77 m
4.5
4.0
3.5
3.0
2.5
2.0
1.5
1.0
0.5
0
m

Figure 16.

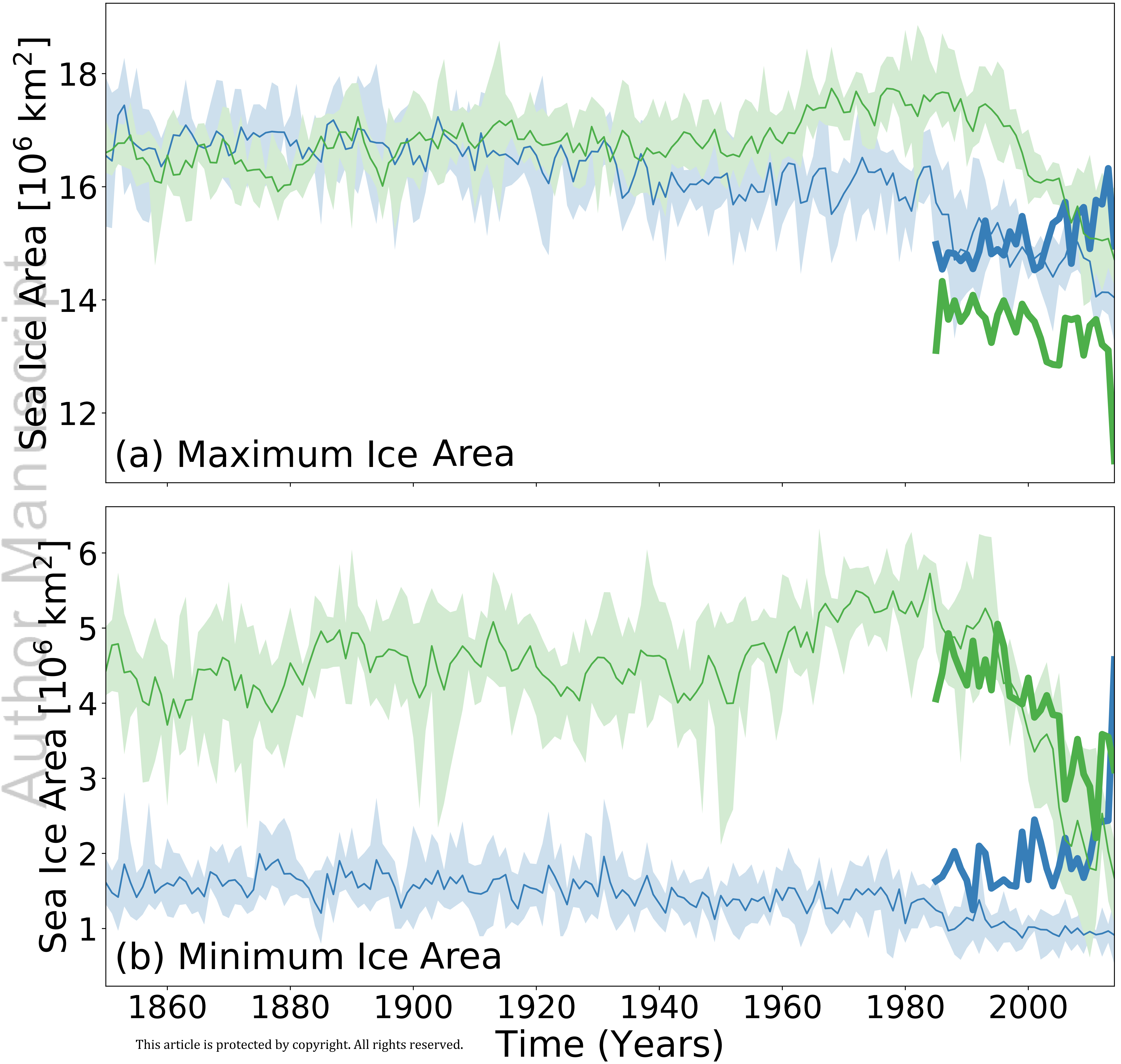

Sea Ice Area [10^6 km^2]
18
16
14
12
(a) Maximum Ice Area
Sea Ice Area [10^6 km^2]
6
5
4
3
2
1
(b) Minimum Ice Area
1860
1880
1900
1920
1940
1960
1980
2000
Time (Years)

Figure 17.

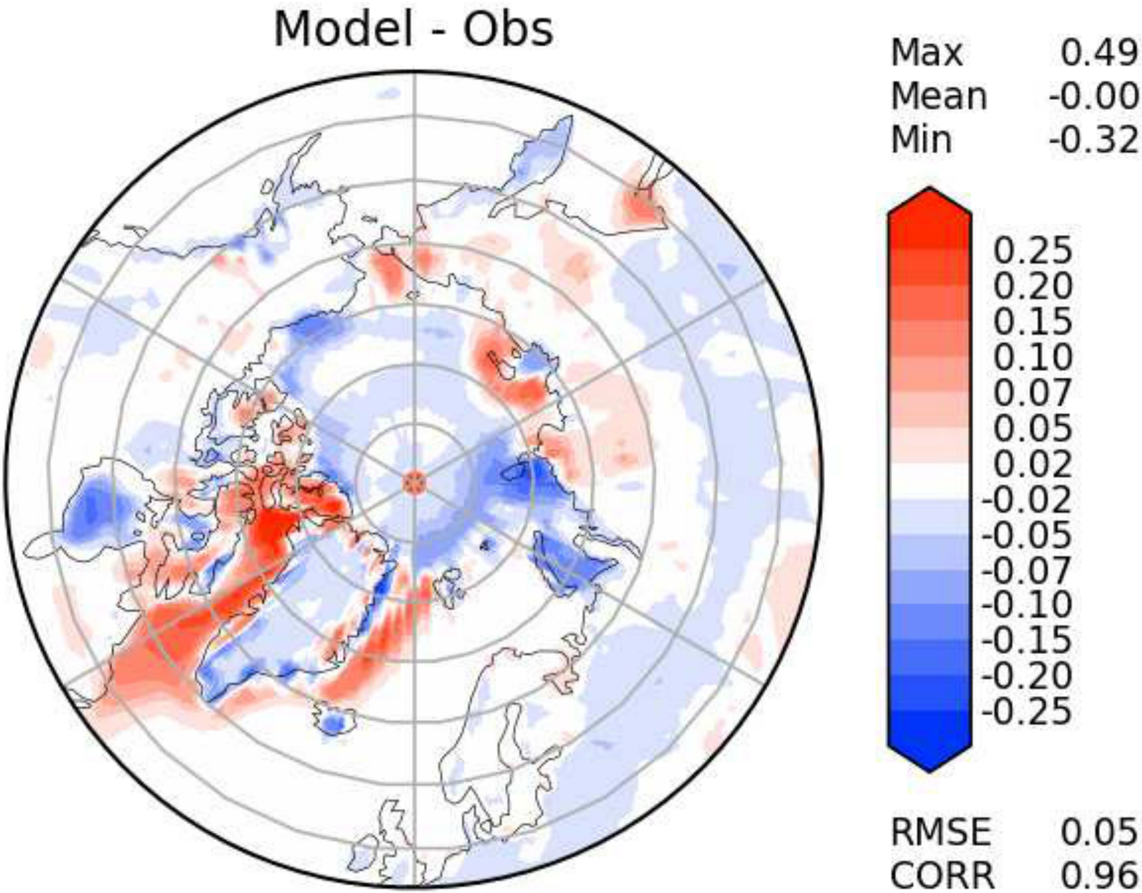
Model - Obs
Max 0.49
Mean -0.00
Min -0.32
0.25
0.20
0.15
0.10
0.07
0.05
0.02
-0.02
-0.05
-0.07
-0.10
-0.15
-0.20
-0.25
RMSE 0.05
CORR 0.96

Figure 18.

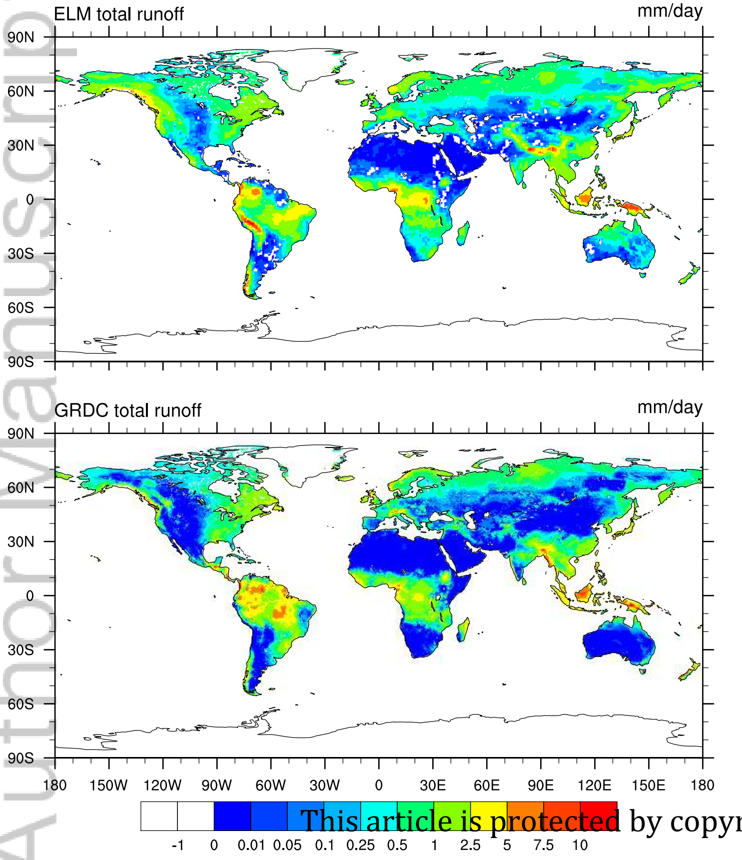
ELM total runoff
mm/day
GRDC total runoff
mm/day
90N
60N
30N
0
30S
60S
90S
180
150W
120W
90W
60W
30W
0
30E
60E
90E
120E
150E
180
-1
0
0.01
0.05
0.1
0.25
0.5
1
2.5
5
7.5
10

Figure 19.

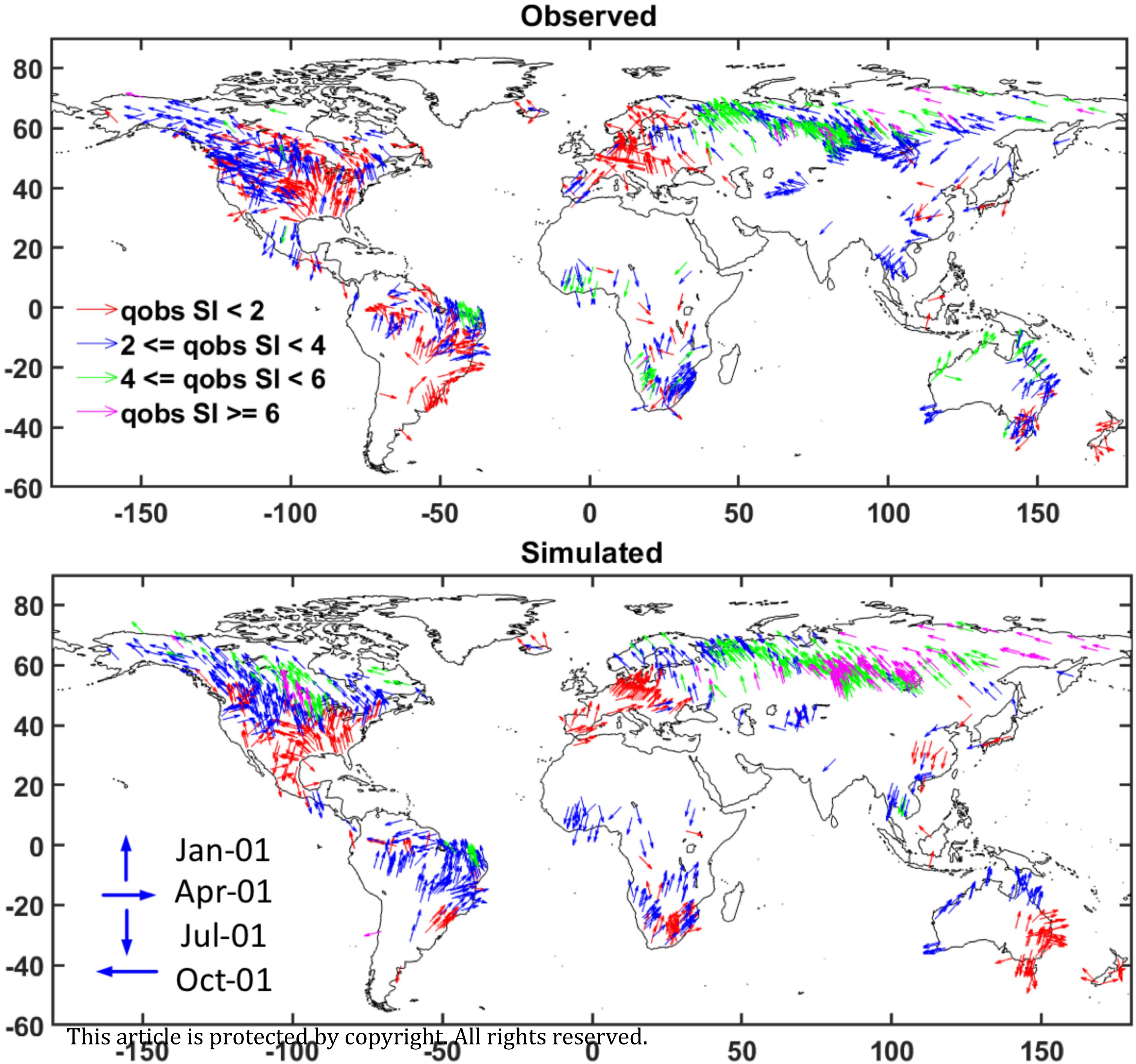
Observed
qobs SI < 2
2 <= qobs SI < 4
4 <= qobs SI < 6
qobs SI >= 6
80
60
40
20
0
-20
-40
-60
-150
-100
-50
0
50
100
150
Simulated
Jan-01
Apr-01
Jul-01
Oct-01

Figure 20.

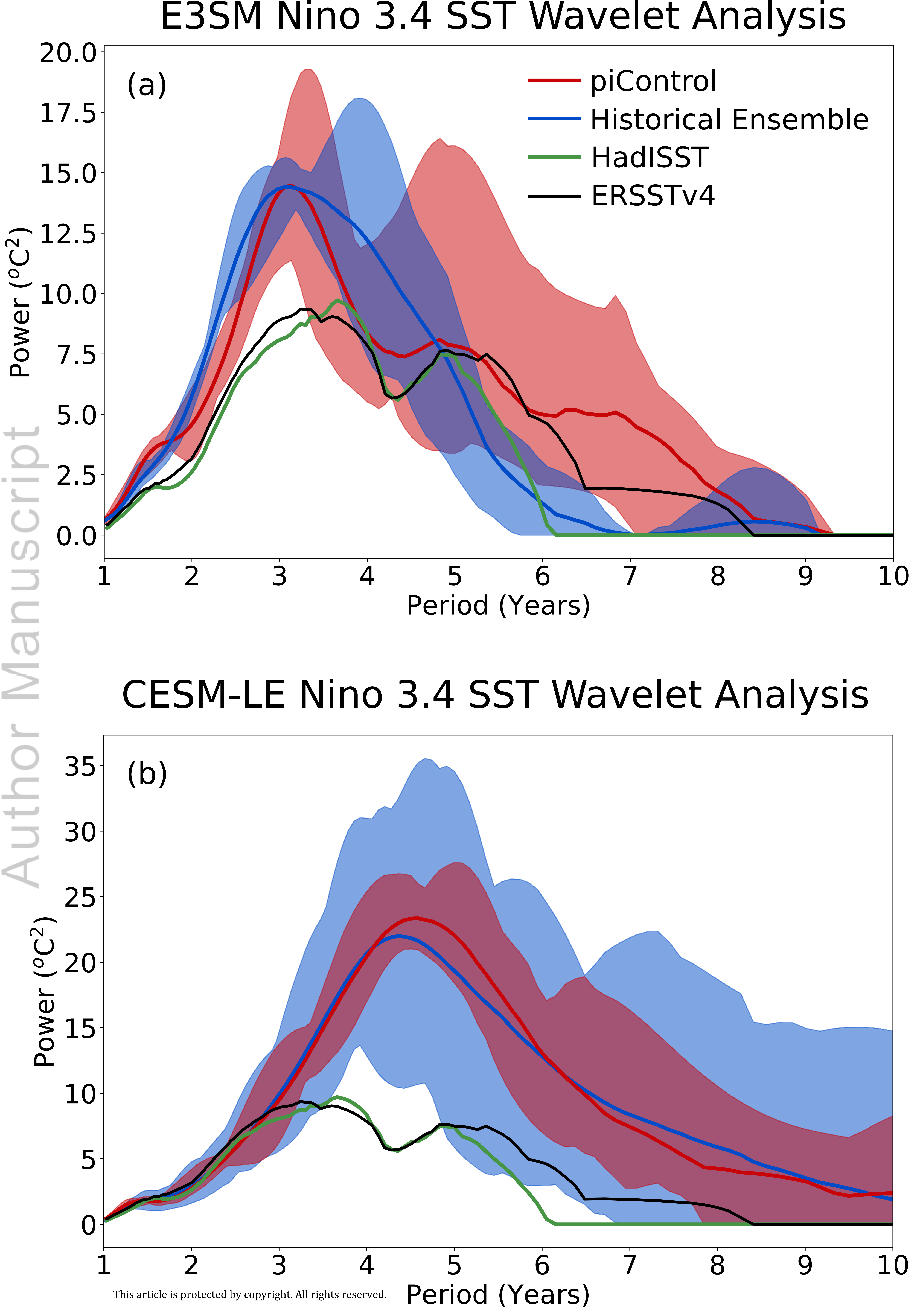

E3SM Nino 3.4 SST Wavelet Analysis
(a)
piControl
Historical Ensemble
HadISST
ERSSTv4
Power ($^oC^2$)
Period (Years)
CESM-LE Nino 3.4 SST Wavelet Analysis
(b)
Power ($^oC^2$)
Period (Years)

Figure 21.

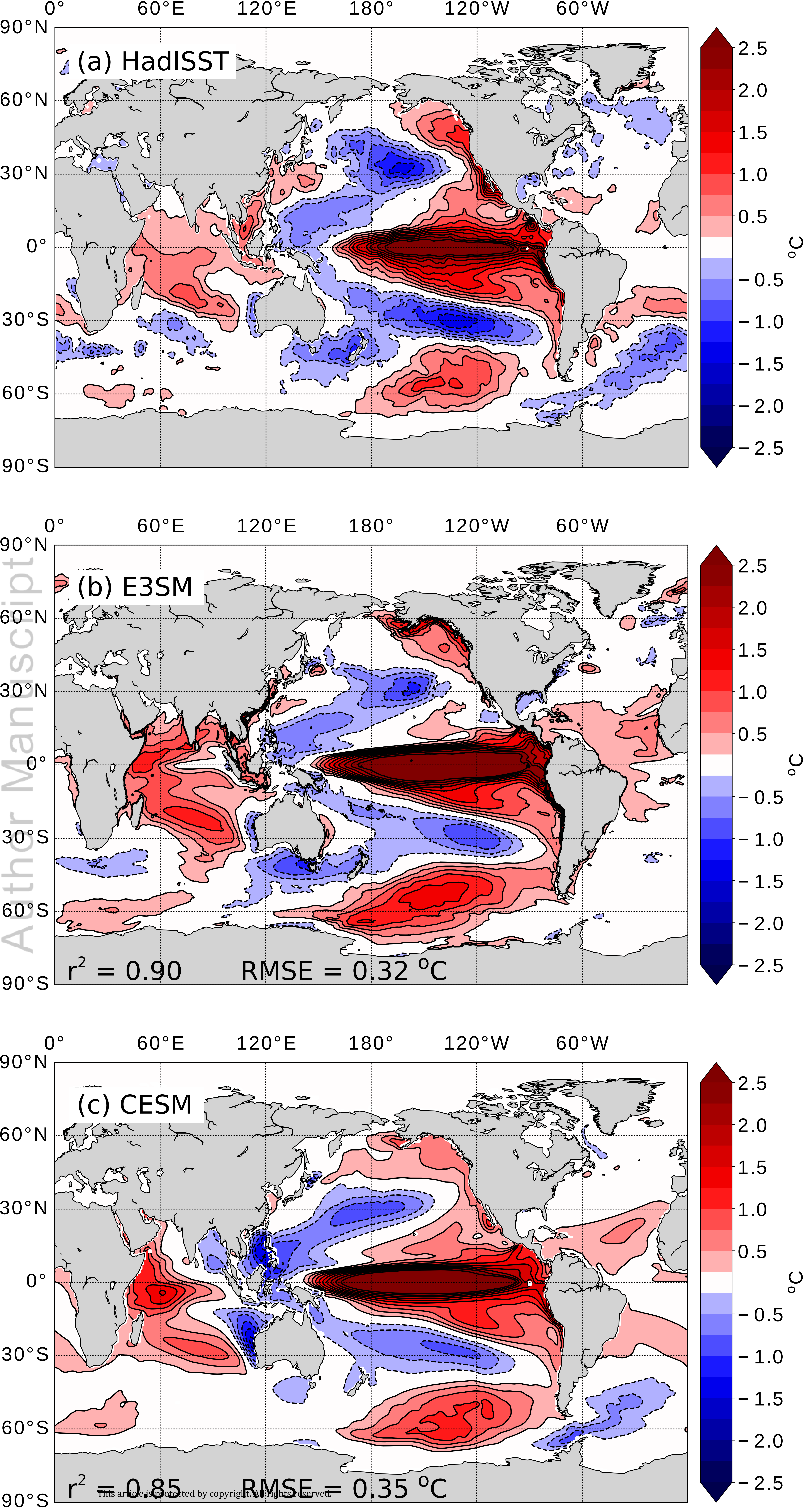
(a) HadISST
(b) E3SM
r^2 = 0.90
RMSE = 0.32 ^{o}C
(c) CESM
r^2 = 0.85
RMSE = 0.35 ^{o}C
0°
60°E
120°E
180°
120°W
60°W
90°N
60°N
30°N
0°
30°S
60°S
90°S
2.5
2.0
1.5
1.0
0.5
−0.5
−1.0
−1.5
−2.0
−2.5
^{o}C

Figure 22.

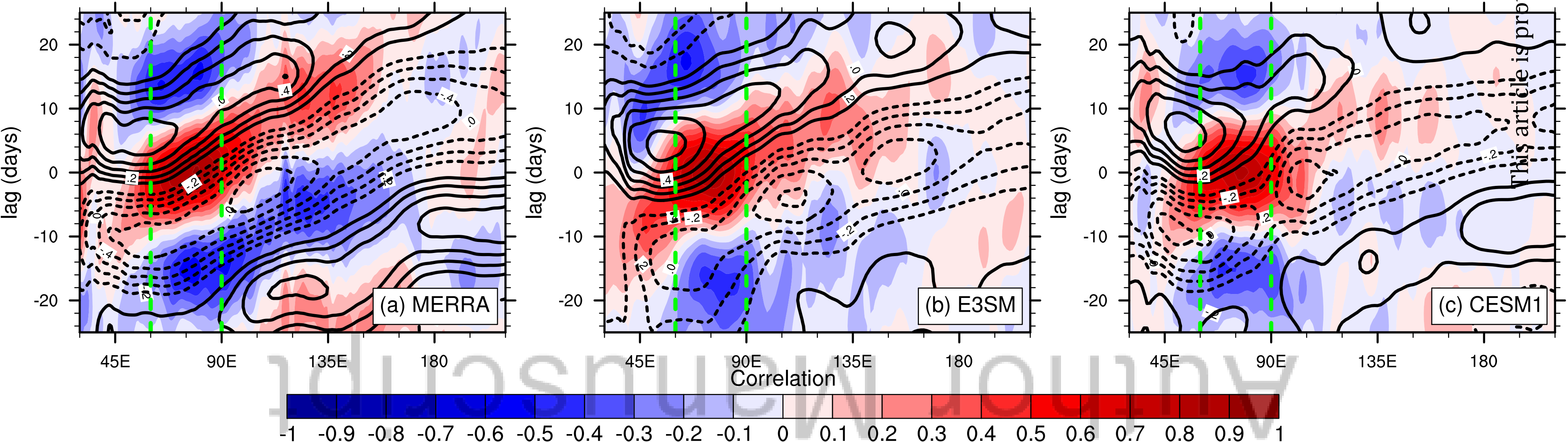
(a) MERRA
(b) E3SM
(c) CESM1
lag (days)
-20
-10
0
10
20
45E
90E
135E
180
Correlation
-1 -0.9 -0.8 -0.7 -0.6 -0.5 -0.4 -0.3 -0.2 -0.1 0 0.1 0.2 0.3 0.4 0.5 0.6 0.7 0.8 0.9 1

Figure 23.

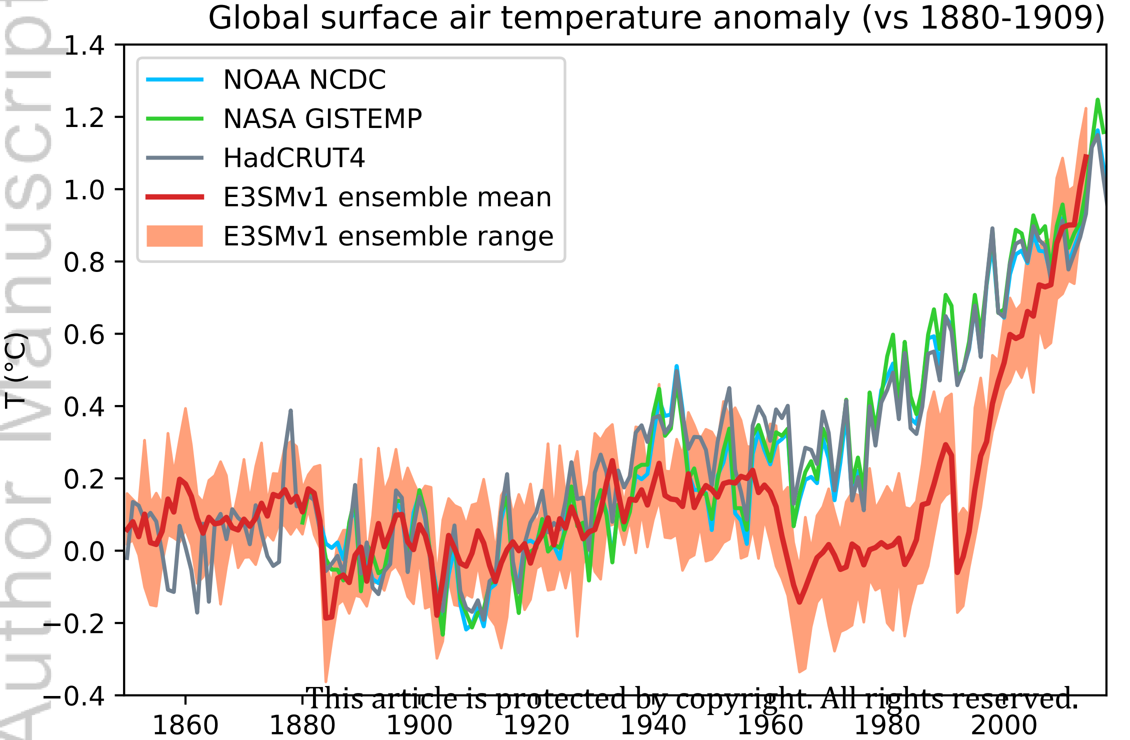
Global surface air temperature anomaly (vs 1880-1909)
T (°C)
1.4
1.2
1.0
0.8
0.6
0.4
0.2
0.0
−0.2
−0.4
1860
1880
1900
1920
1940
1960
1980
2000
NOAA NCDC
NASA GISTEMP
HadCRUT4
E3SMv1 ensemble mean
E3SMv1 ensemble range

Figure 24.

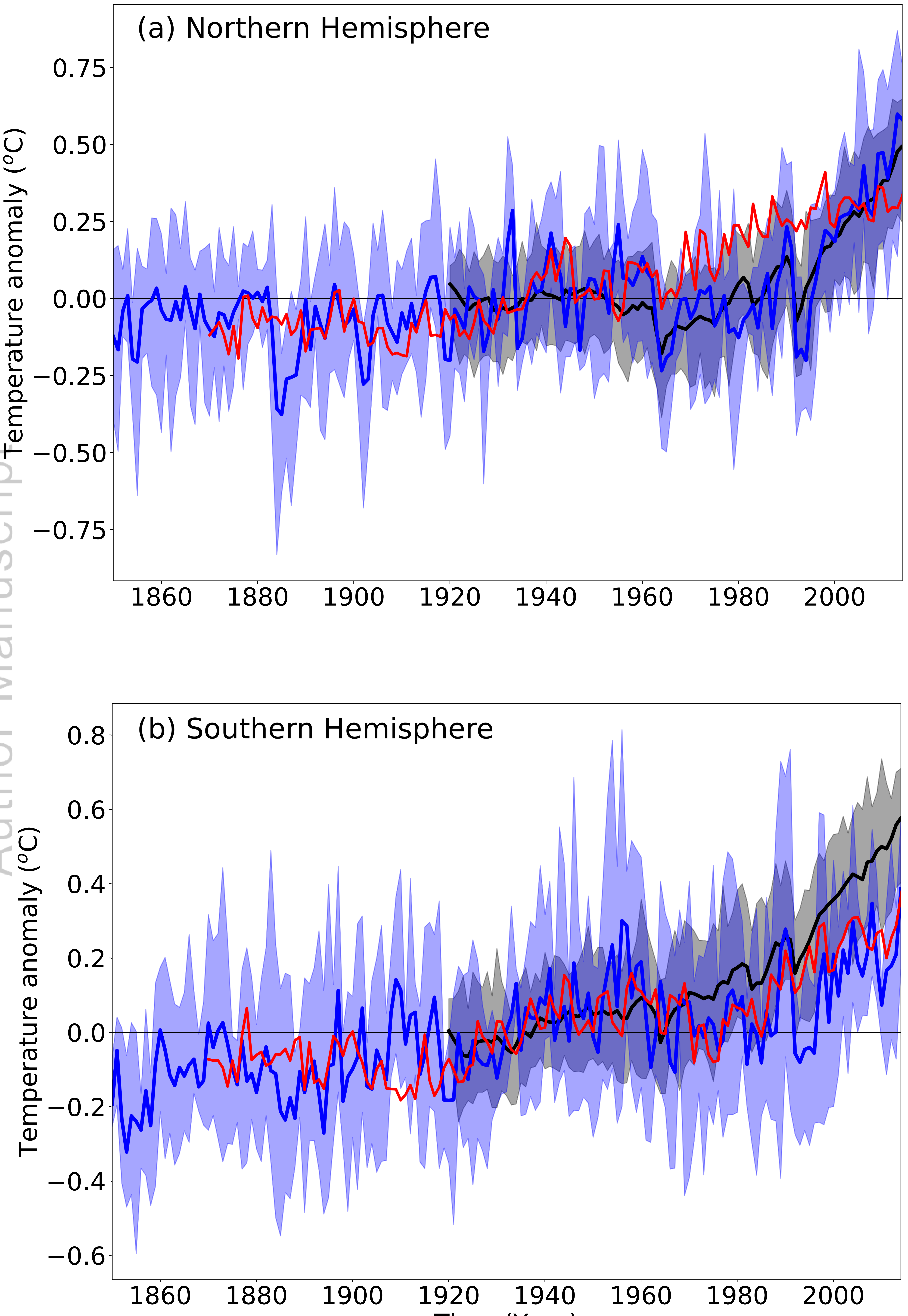
(a) Northern Hemisphere
Temperature anomaly (^oC)
0.75
0.50
0.25
0.00
−0.25
−0.50
−0.75
1860
1880
1900
1920
1940
1960
1980
2000
(b) Southern Hemisphere
Temperature anomaly (^oC)
0.8
0.6
0.4
0.2
0.0
−0.2
−0.4
−0.6
1860
1880
1900
1920
1940
1960
1980
2000
Time (Year)

Figure 25.

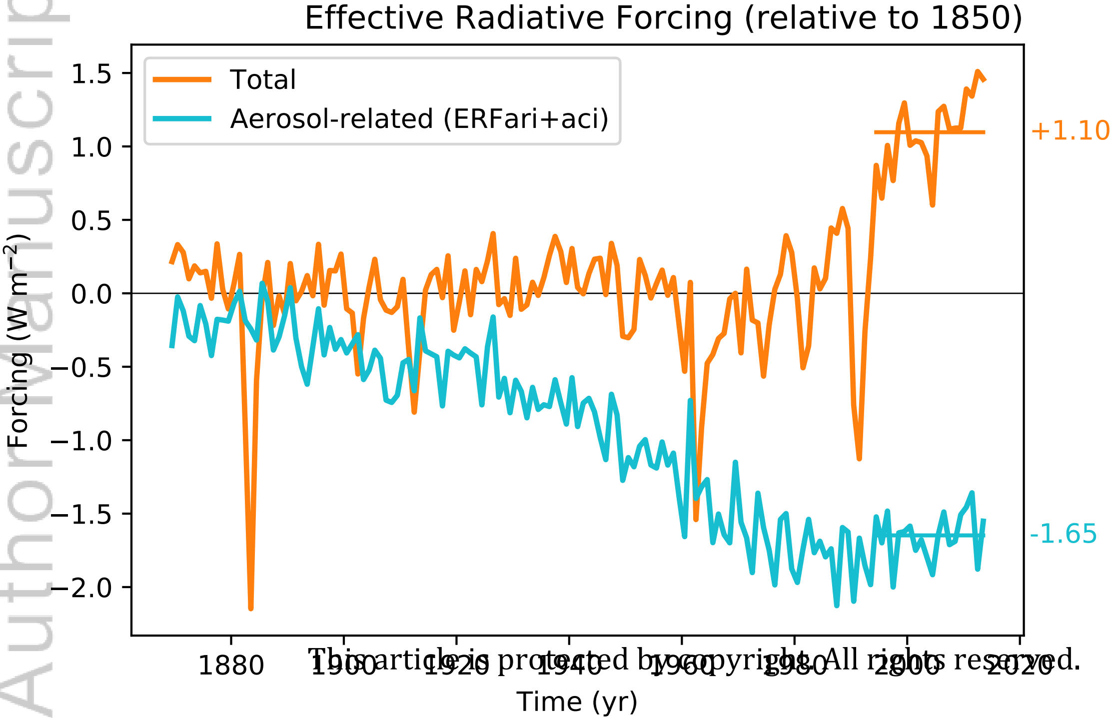

Effective Radiative Forcing (relative to 1850)
Total
Aerosol-related (ERFari+aci)
+1.10
-1.65
Forcing (W m^{-2})
1.5
1.0
0.5
0.0
−0.5
−1.0
−1.5
−2.0
1880
1900
1920
1940
1960
1980
2000
2020
Time (yr)

Figure 26.

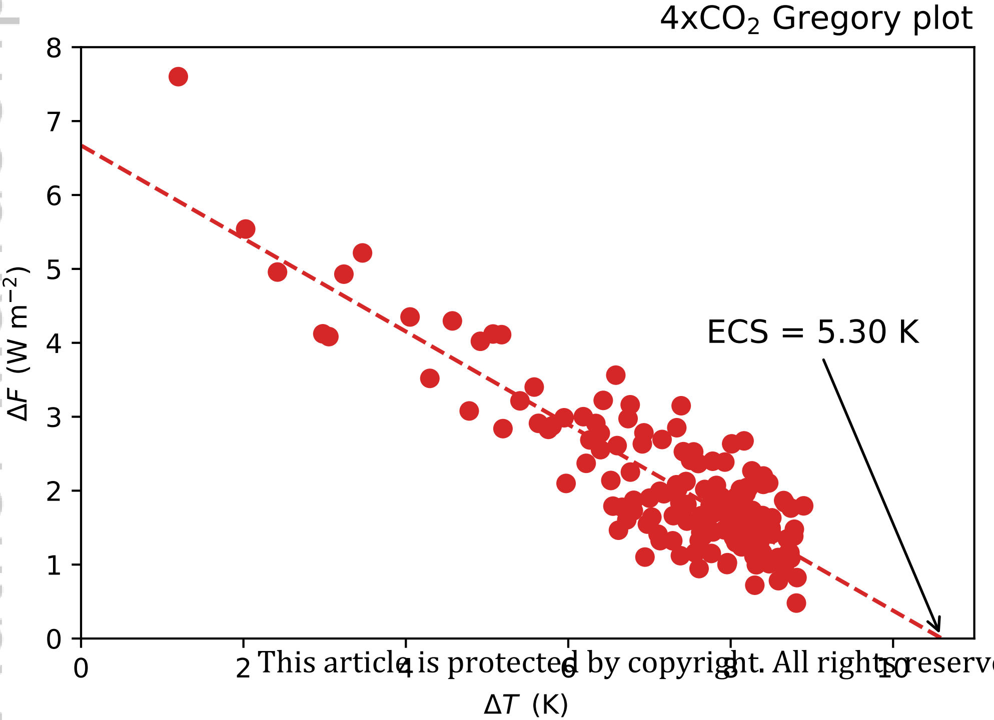
4xCO2 Gregory plot
ECS = 5.30 K
ΔF (W m−2)
ΔT (K)
0
1
2
3
4
5
6
7
8
0
2
4
6
8
10

Figure 27.

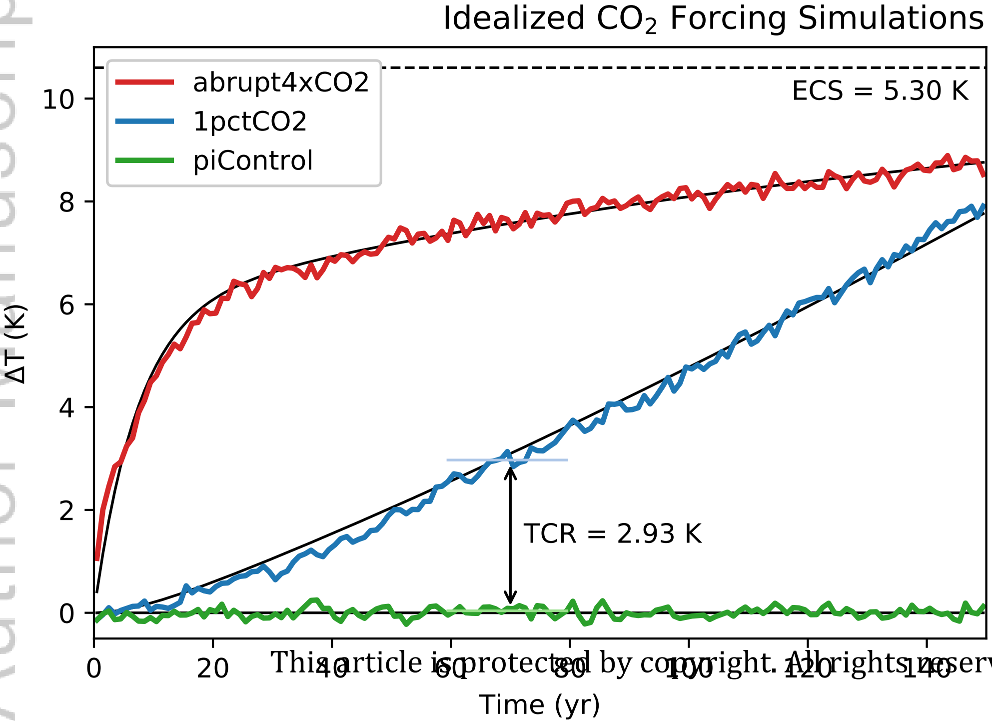

Idealized CO_2 Forcing Simulations
abrupt4xCO2
1pctCO2
piControl
ECS = 5.30 K
TCR = 2.93 K
ΔT (K)
10
8
6
4
2
0
0
20
40
60
80
100
120
140
Time (yr)

Figure 28.

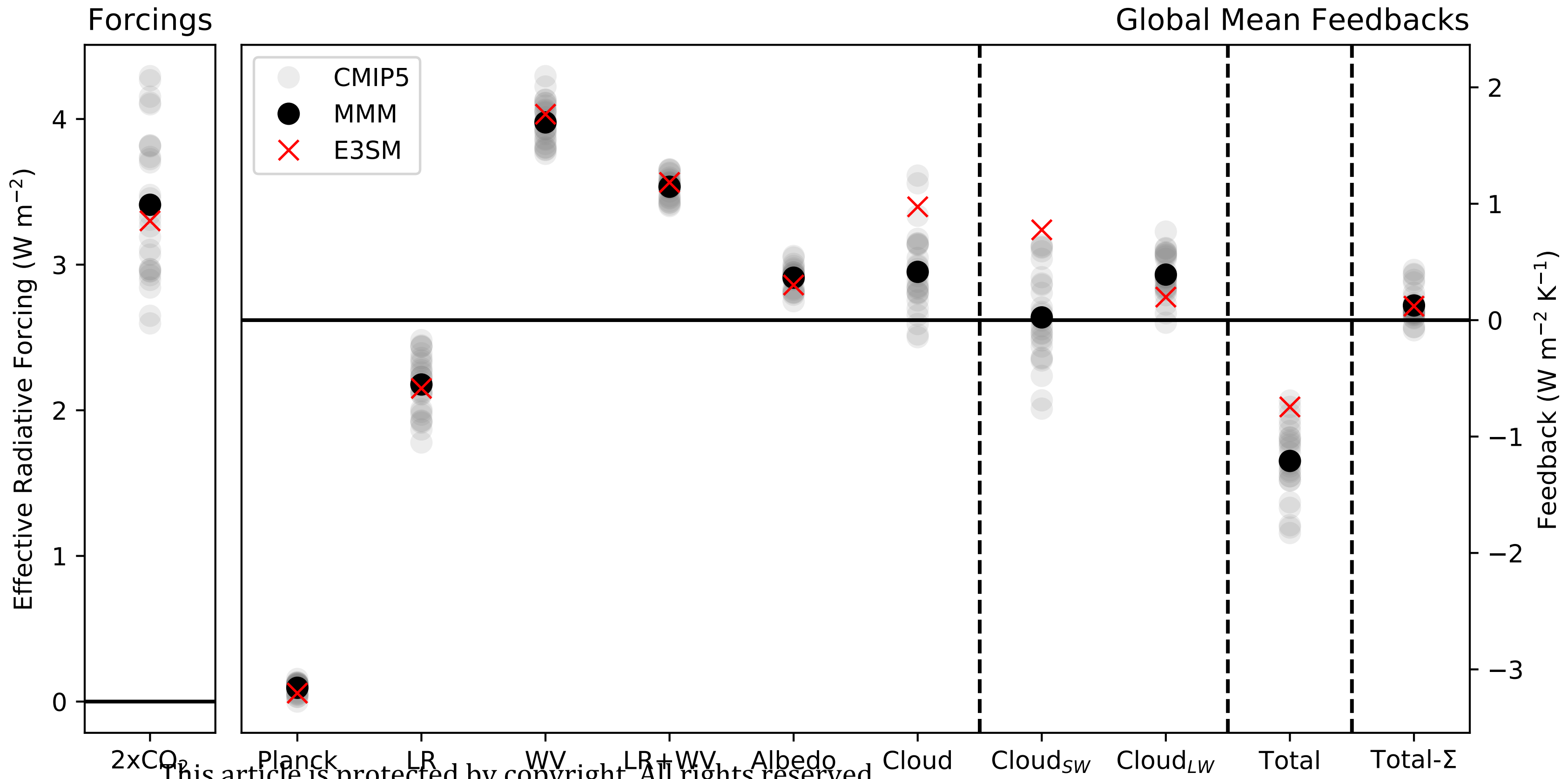
Forcings
Global Mean Feedbacks
CMIP5
MMM
E3SM
Effective Radiative Forcing (W m^{-2})
Feedback (W m^{-2} K^{-1})
4
3
2
1
0
2
1
0
−1
−2
−3
2xCO$_2$
Planck
LR
WV
LR+WV
Albedo
Cloud
Cloud$_{SW}$
Cloud$_{LW}$
Total
Total-Σ

Figure 29.

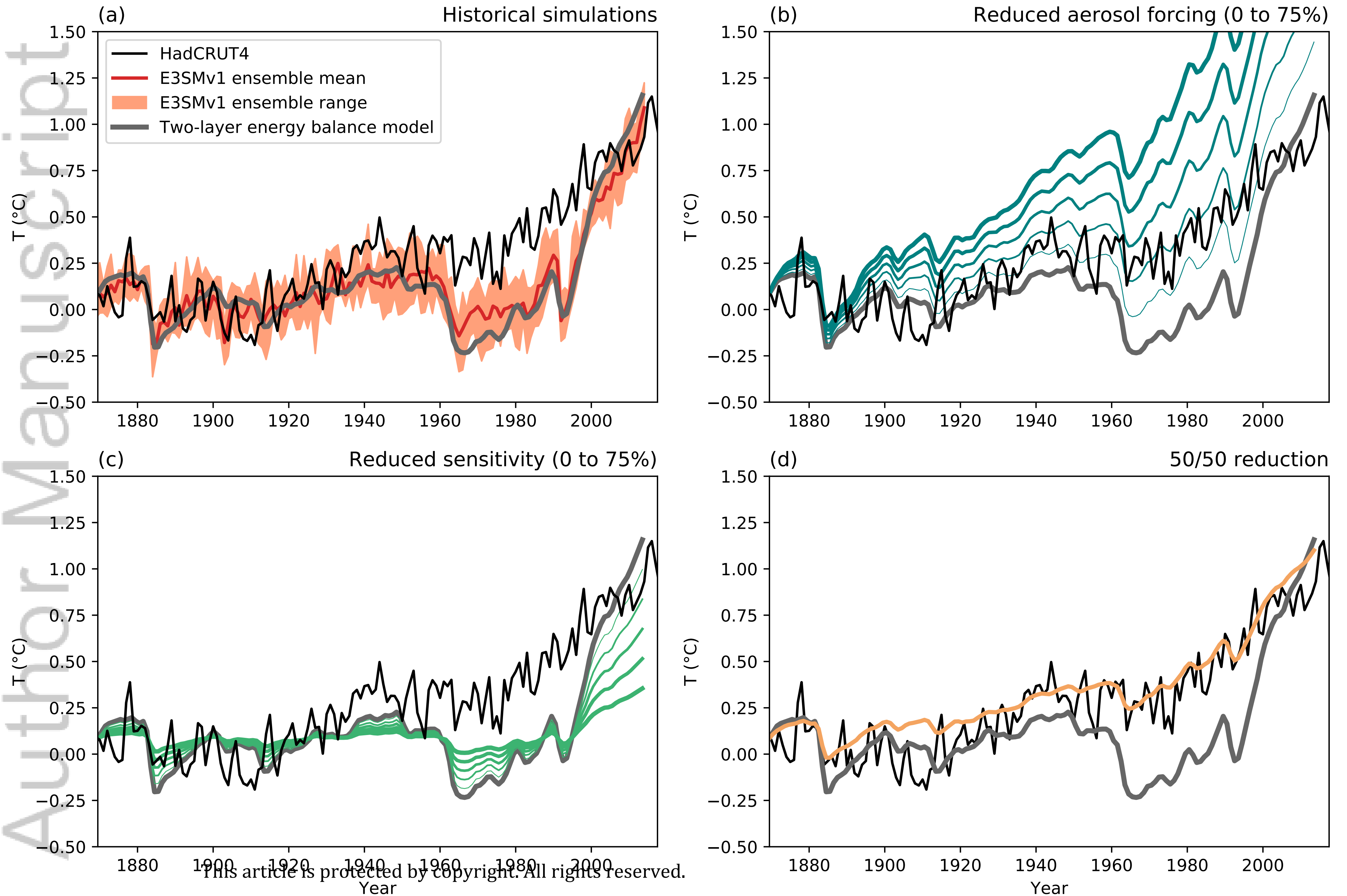
(a)
Historical simulations
HadCRUT4
E3SMv1 ensemble mean
E3SMv1 ensemble range
Two-layer energy balance model
(b)
Reduced aerosol forcing (0 to 75%)
(c)
Reduced sensitivity (0 to 75%)
(d)
50/50 reduction
T (°C)
Year
1.50
1.25
1.00
0.75
0.50
0.25
0.00
−0.25
−0.50
1880
1900
1920
1940
1960
1980
2000

Figure A1.

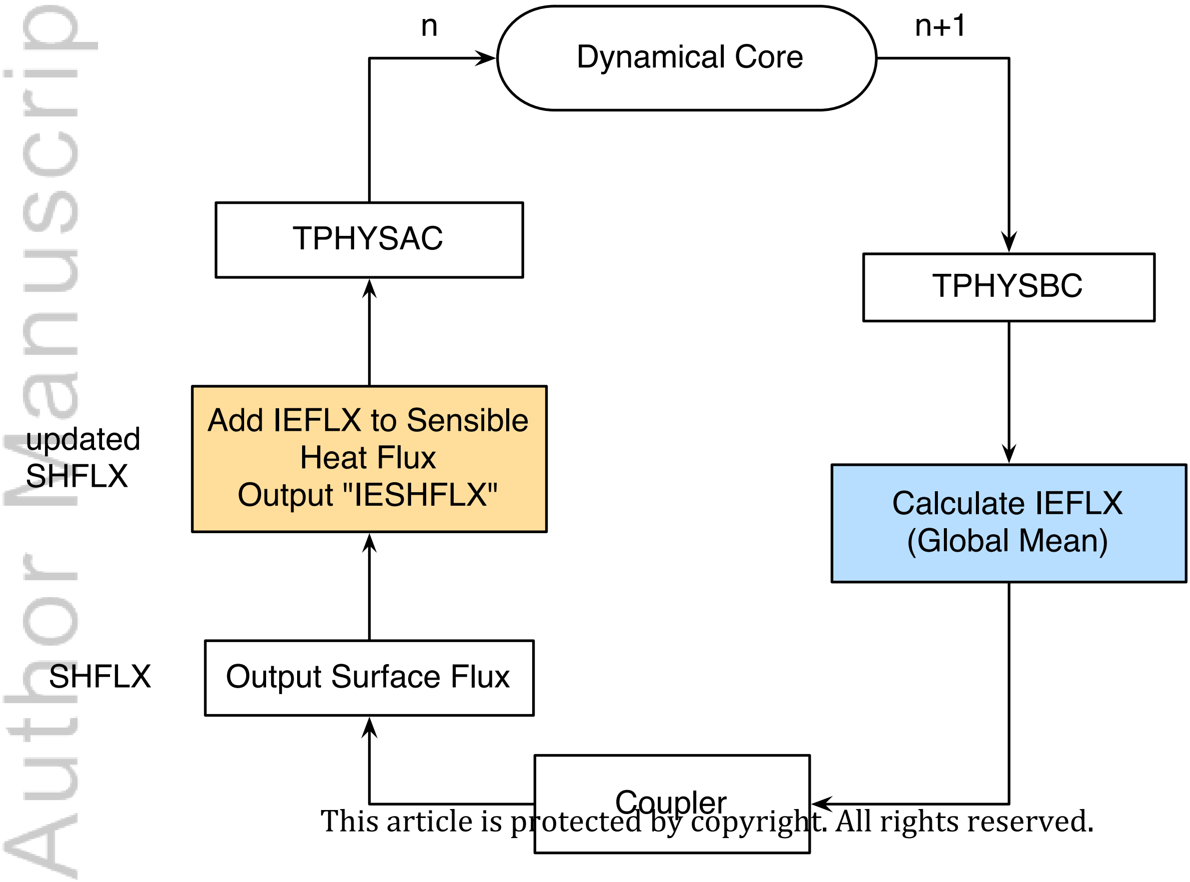
n
Dynamical Core
n+1
TPHYSAC
TPHYSBC
updated
SHFLX
Add IEFLX to Sensible
Heat Flux
Output "IESHFLX"
Calculate IEFLX
(Global Mean)
SHFLX
Output Surface Flux
Coupler

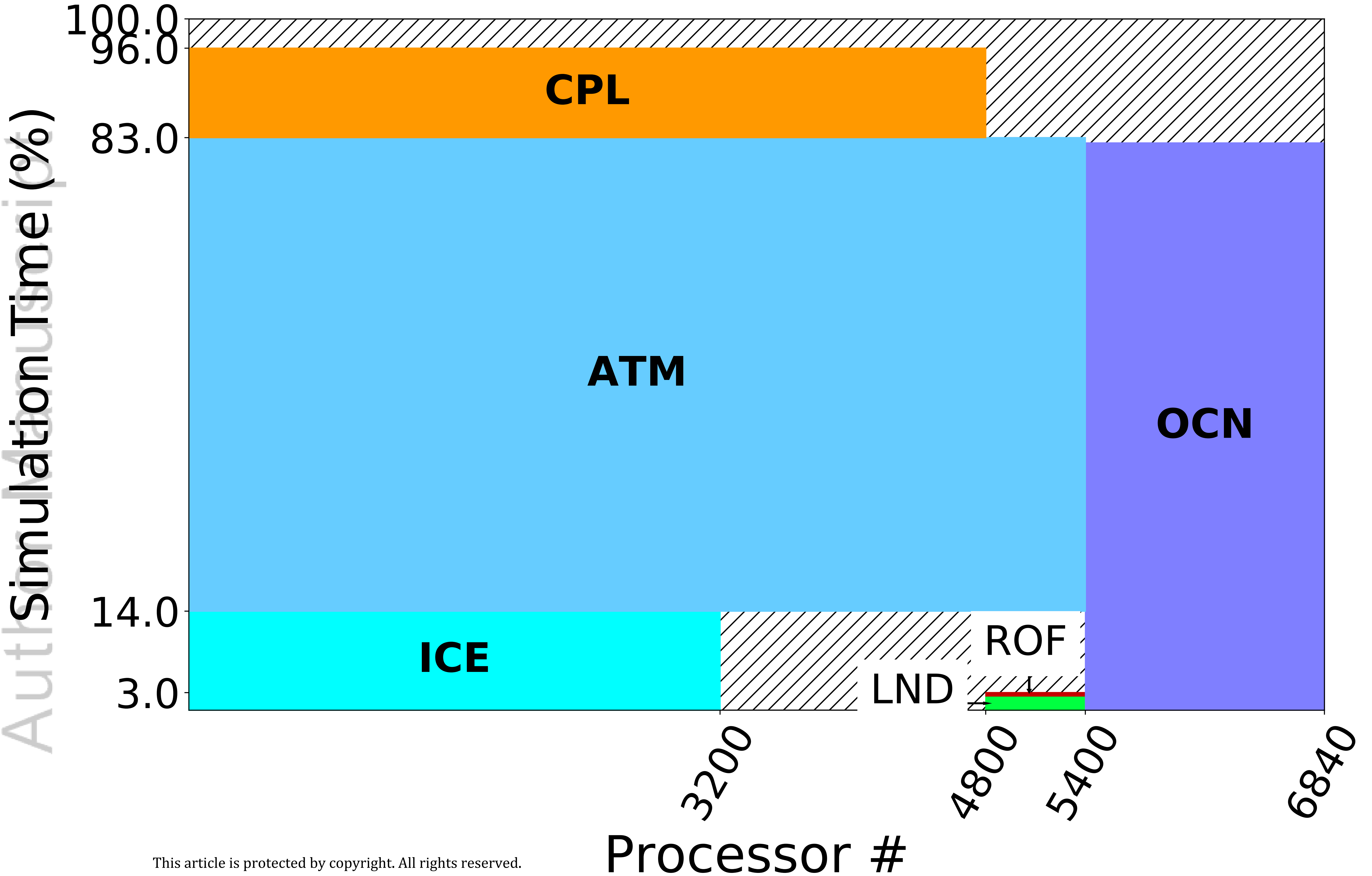

Simulation Time (%)
100.0
96.0
83.0
14.0
3.0
CPL
ATM
OCN
ICE
ROF
LND
3200
4800
5400
6840
Processor #

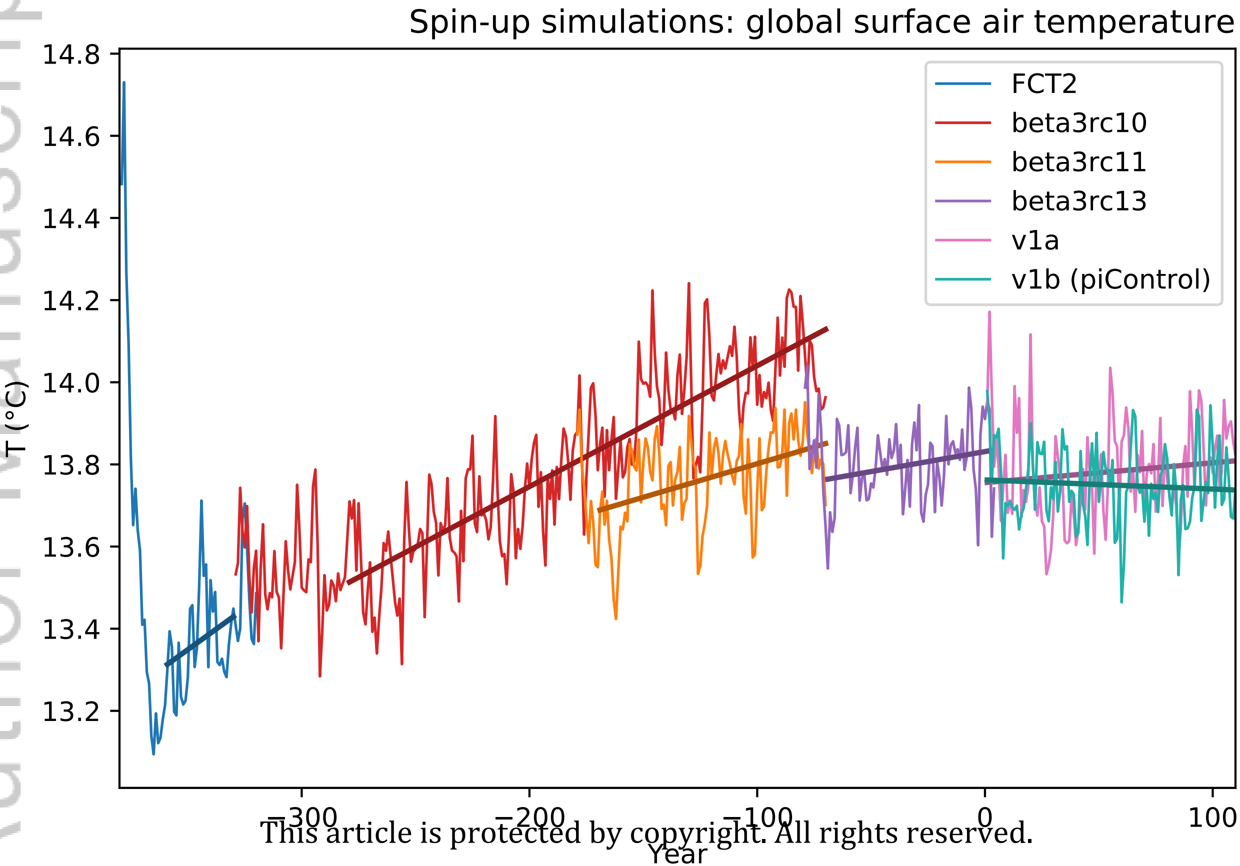
Spin-up simulations: global surface air temperature
T (°C)
14.8
14.6
14.4
14.2
14.0
13.8
13.6
13.4
13.2
−300
−200
−100
0
100
Year
FCT2
beta3rc10
beta3rc11
beta3rc13
v1a
v1b (piControl)

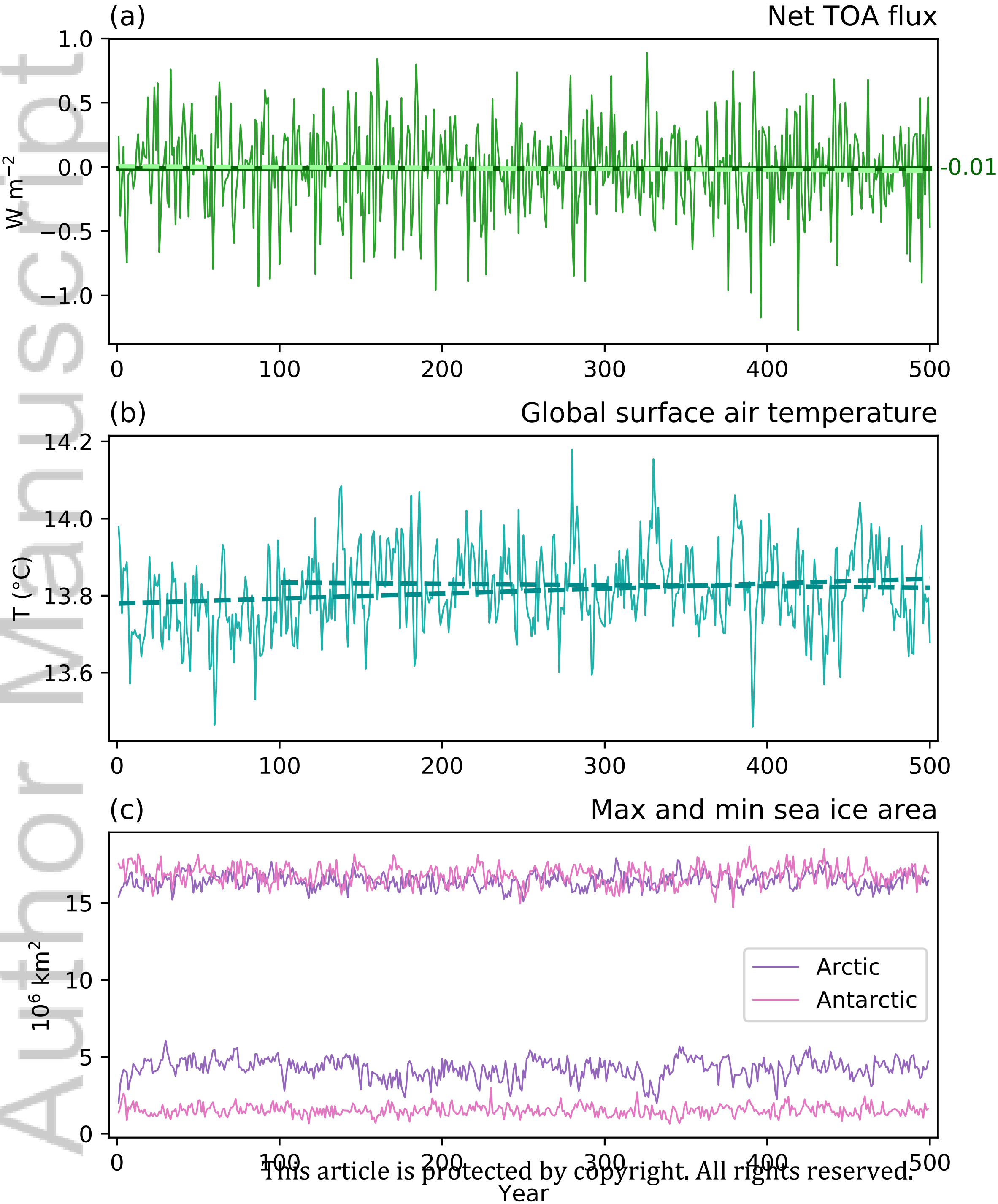

(a)
Net TOA flux
W m^{-2}
1.0
0.5
0.0
−0.5
−1.0
-0.01
0
100
200
300
400
500
(b)
Global surface air temperature
T (°C)
14.2
14.0
13.8
13.6
(c)
Max and min sea ice area
10^6 km^2
15
10
5
Arctic
Antarctic
Year

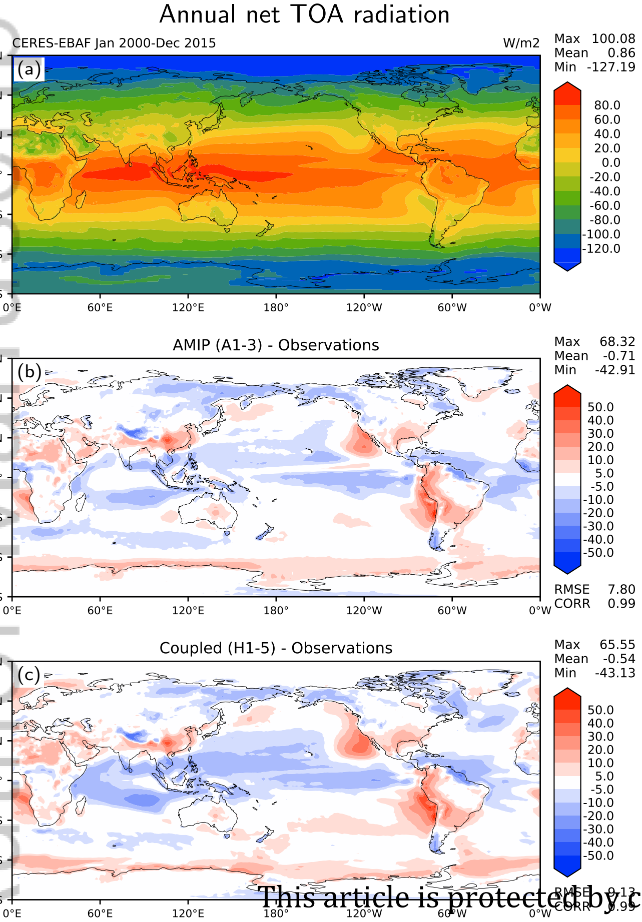
Annual net TOA radiation
CERES-EBAF Jan 2000-Dec 2015
W/m2
Max 100.08
Mean 0.86
Min -127.19
(a)
80.0
60.0
40.0
20.0
0.0
-20.0
-40.0
-60.0
-80.0
-100.0
-120.0
AMIP (A1-3) - Observations
Max 68.32
Mean -0.71
Min -42.91
(b)
RMSE 7.80
CORR 0.99
Coupled (H1-5) - Observations
Max 65.55
Mean -0.54
Min -43.13
(c)
50.0
40.0
30.0
20.0
10.0
5.0
-5.0
-10.0
-20.0
-30.0
-40.0
-50.0
RMSE 9.13
CORR 0.99
90°N
60°N
30°N
0°
30°S
60°S
90°S
0°E
60°E
120°E
180°
120°W
60°W
0°W

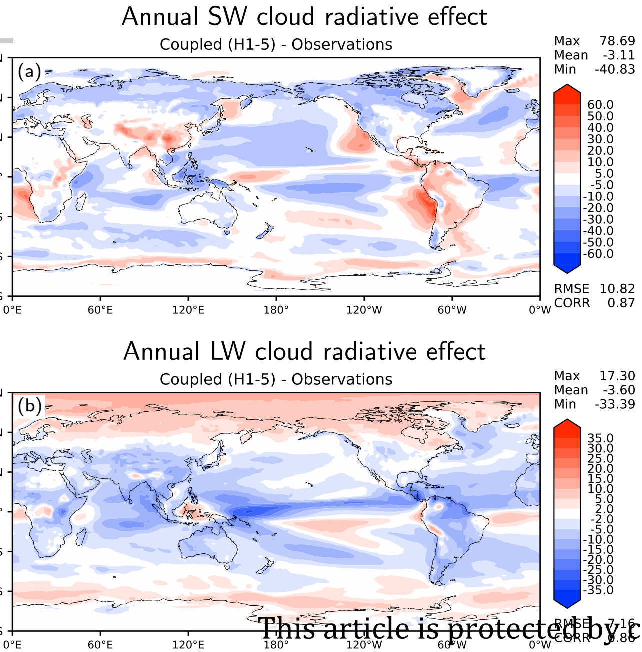

Annual SW cloud radiative effect
Coupled (H1-5) - Observations
(a)
Max 78.69
Mean -3.11
Min -40.83
60.0
50.0
40.0
30.0
20.0
10.0
5.0
-5.0
-10.0
-20.0
-30.0
-40.0
-50.0
-60.0
RMSE 10.82
CORR 0.87
90°N
60°N
30°N
0°
30°S
60°S
90°S
0°E
60°E
120°E
180°
120°W
60°W
0°W
Annual LW cloud radiative effect
Coupled (H1-5) - Observations
(b)
Max 17.30
Mean -3.60
Min -33.39
35.0
30.0
25.0
20.0
15.0
10.0
5.0
2.0
-2.0
-5.0
-10.0
-15.0
-20.0
-25.0
-30.0
-35.0
RMSE 7.16
CORR 0.86

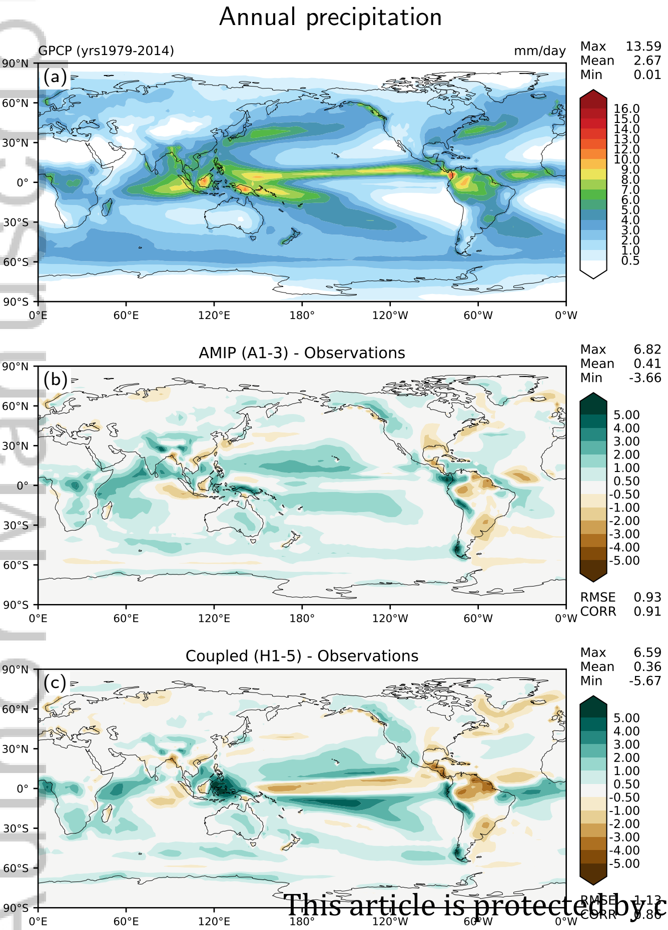
Annual precipitation
GPCP (yrs1979-2014)
mm/day
Max 13.59
Mean 2.67
Min 0.01
(a)
16.0
15.0
14.0
13.0
12.0
10.0
9.0
8.0
7.0
6.0
5.0
4.0
3.0
2.0
1.0
0.5
AMIP (A1-3) - Observations
Max 6.82
Mean 0.41
Min -3.66
(b)
RMSE 0.93
CORR 0.91
Coupled (H1-5) - Observations
Max 6.59
Mean 0.36
Min -5.67
(c)
5.00
4.00
3.00
2.00
1.00
0.50
-0.50
-1.00
-2.00
-3.00
-4.00
-5.00
RMSE 1.13
CORR 0.86
90°N
60°N
30°N
0°
30°S
60°S
90°S
0°E
60°E
120°E
180°
120°W
60°W
0°W

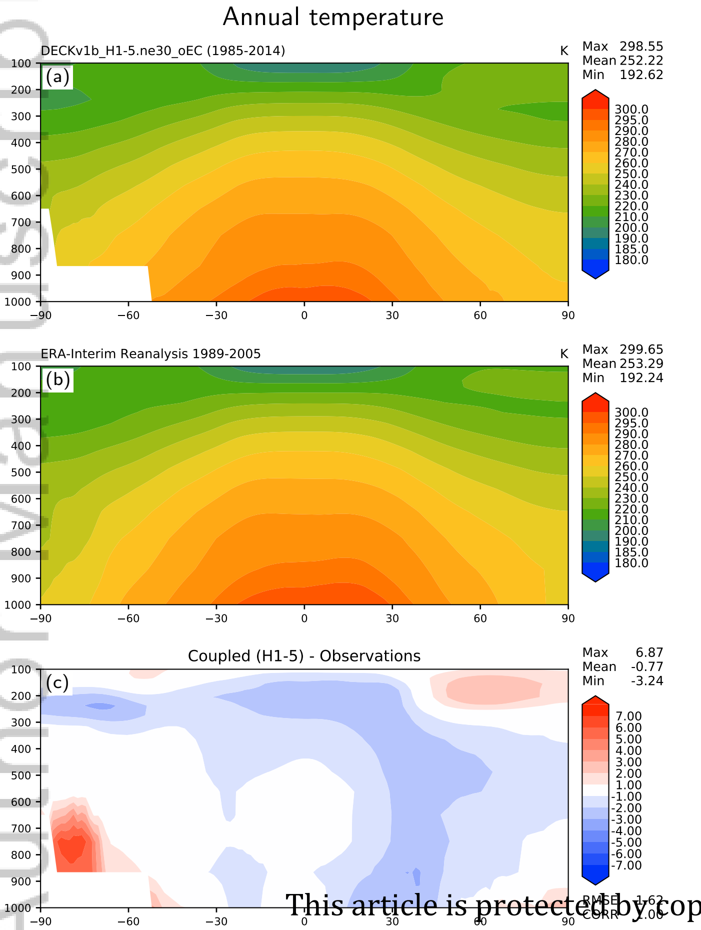
Annual temperature
DECKv1b_H1-5.ne30_oEC (1985-2014)
K
Max 298.55
Mean 252.22
Min 192.62
(a)
ERA-Interim Reanalysis 1989-2005
K
Max 299.65
Mean 253.29
Min 192.24
(b)
Coupled (H1-5) - Observations
Max 6.87
Mean -0.77
Min -3.24
(c)
RMSE 1.62
CORR 1.00
100
200
300
400
500
600
700
800
900
1000
−90
−60
−30
0
30
60
90
300.0
295.0
290.0
280.0
270.0
260.0
250.0
240.0
230.0
220.0
210.0
200.0
190.0
185.0
180.0
7.00
6.00
5.00
4.00
3.00
2.00
1.00
-1.00
-2.00
-3.00
-4.00
-5.00
-6.00
-7.00

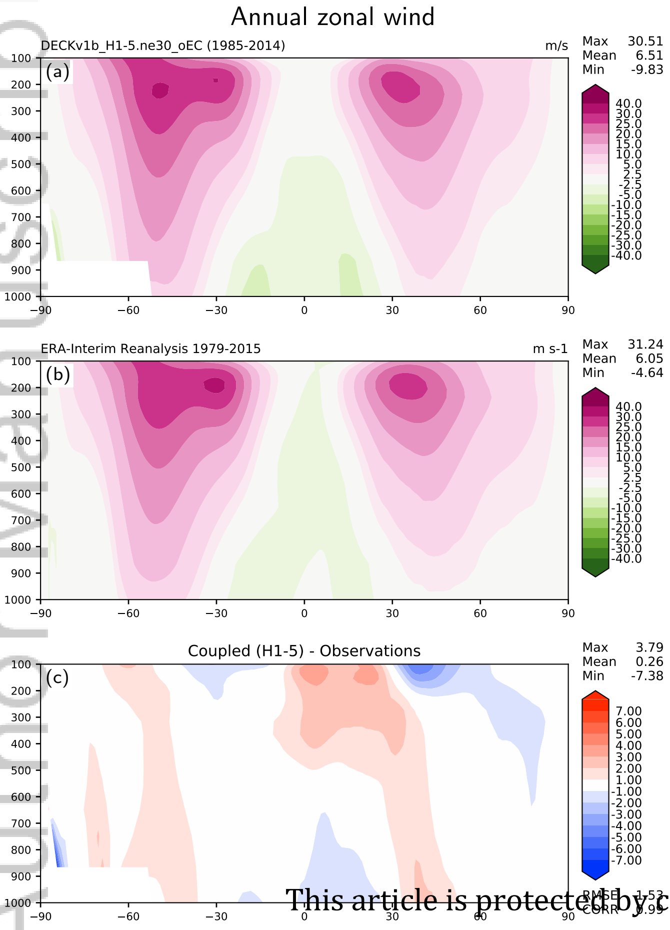
Annual zonal wind
DECKv1b_H1-5.ne30_oEC (1985-2014)
m/s
(a)
Max 30.51
Mean 6.51
Min -9.83
ERA-Interim Reanalysis 1979-2015
m s-1
(b)
Max 31.24
Mean 6.05
Min -4.64
Coupled (H1-5) - Observations
(c)
Max 3.79
Mean 0.26
Min -7.38
RMSE 1.53
CORR 0.99

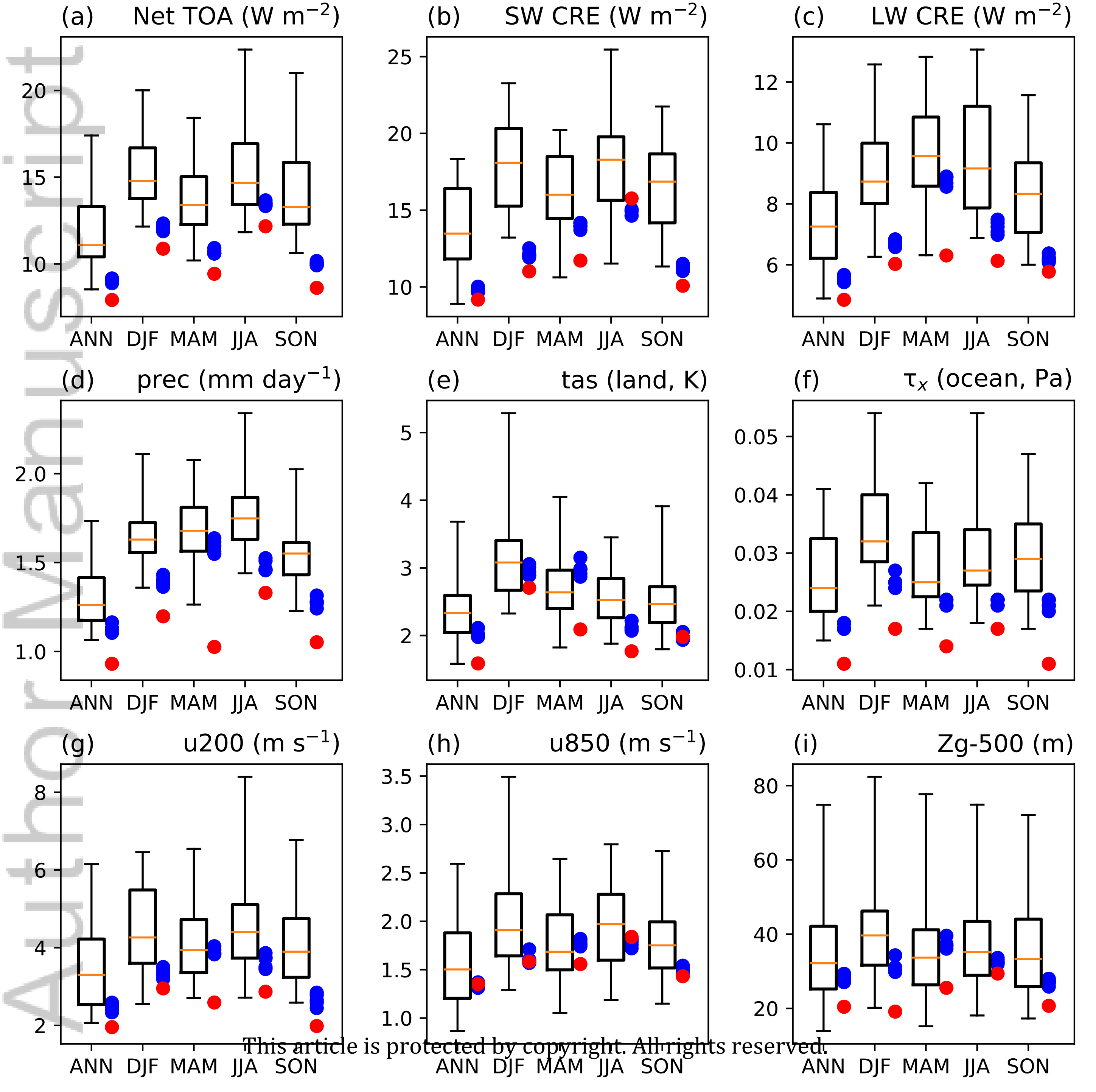

(a) Net TOA (W m^{-2})
(b) SW CRE (W m^{-2})
(c) LW CRE (W m^{-2})
(d) prec (mm day^{-1})
(e) tas (land, K)
(f) τ_x (ocean, Pa)
(g) u200 (m s^{-1})
(h) u850 (m s^{-1})
(i) Zg-500 (m)
ANN DJF MAM JJA SON

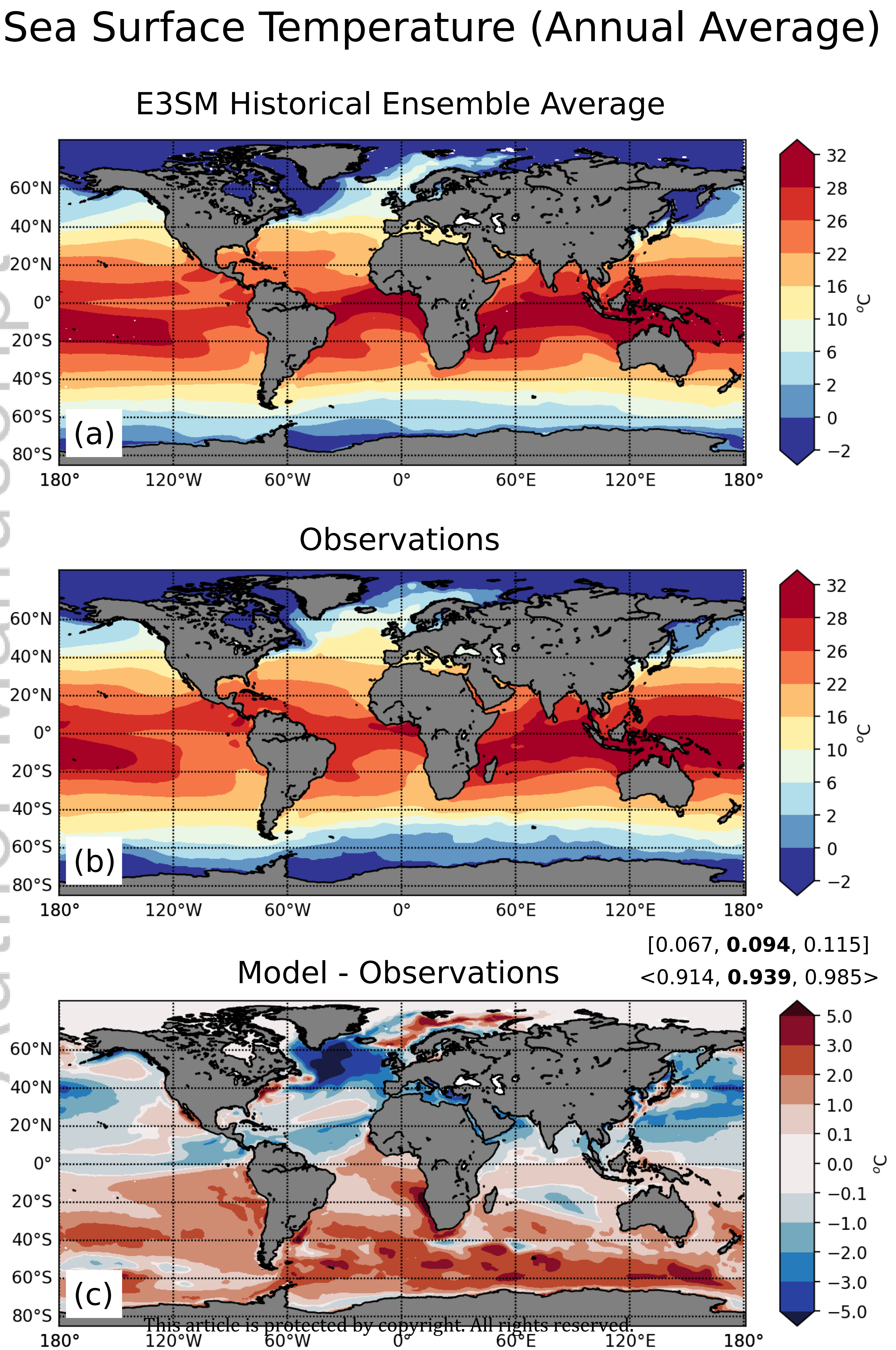
Sea Surface Temperature (Annual Average)
E3SM Historical Ensemble Average
(a)
60°N
40°N
20°N
0°
20°S
40°S
60°S
80°S
180°
120°W
60°W
0°
60°E
120°E
180°
32
28
26
22
16
10
6
2
0
−2
°C
Observations
(b)
[0.067, **0.094**, 0.115]
<0.914, **0.939**, 0.985>
Model - Observations
(c)
5.0
3.0
2.0
1.0
0.1
0.0
−0.1
−1.0
−2.0
−3.0
−5.0

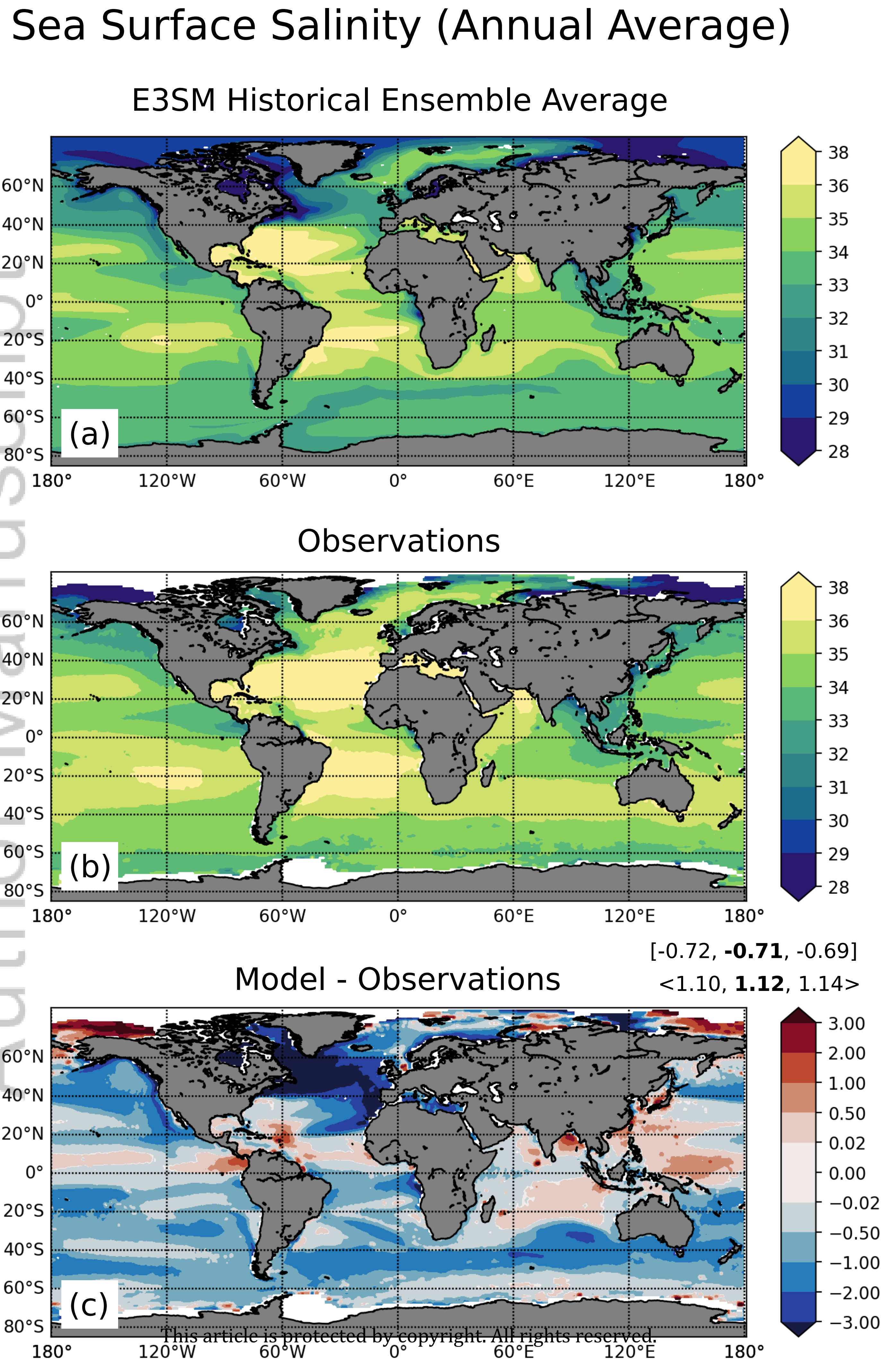
Sea Surface Salinity (Annual Average)
E3SM Historical Ensemble Average
(a)
Observations
(b)
[-0.72, **-0.71**, -0.69]
<1.10, **1.12**, 1.14>
Model - Observations
(c)
60°N
40°N
20°N
0°
20°S
40°S
60°S
80°S
180°
120°W
60°W
0°
60°E
120°E
180°
38
36
35
34
33
32
31
30
29
28
3.00
2.00
1.00
0.50
0.02
0.00
−0.02
−0.50
−1.00
−2.00
−3.00

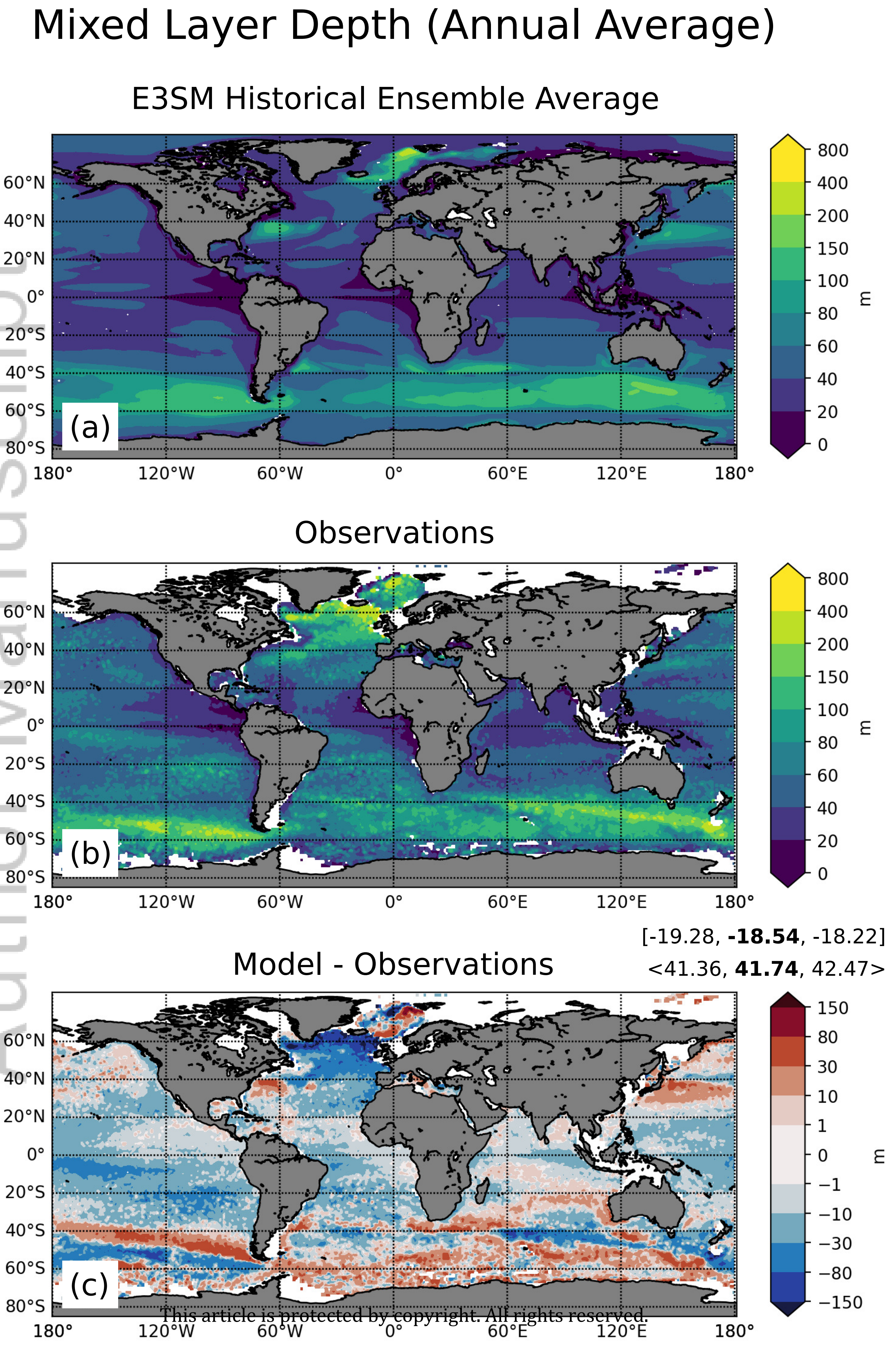

Mixed Layer Depth (Annual Average)
E3SM Historical Ensemble Average
(a)
Observations
(b)
Model - Observations
[-19.28, **-18.54**, -18.22]
<41.36, **41.74**, 42.47>
(c)
60°N
40°N
20°N
0°
20°S
40°S
60°S
80°S
180°
120°W
60°W
0°
60°E
120°E
180°
800
400
200
150
100
80
60
40
20
0
m
150
80
30
10
1
0
−1
−10
−30
−80
−150

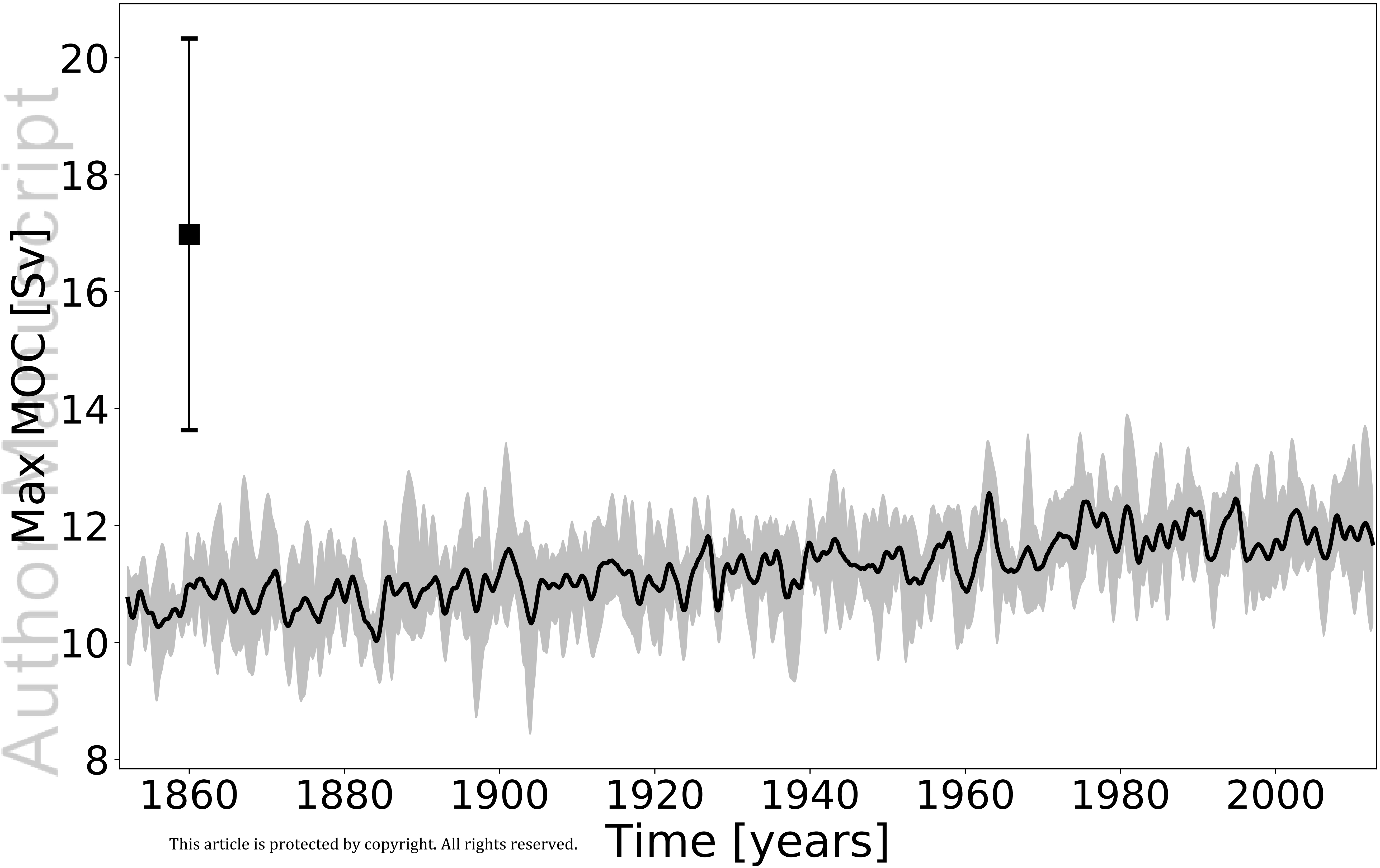

Max MOC [Sv]
8
10
12
14
16
18
20
1860
1880
1900
1920
1940
1960
1980
2000
Time [years]

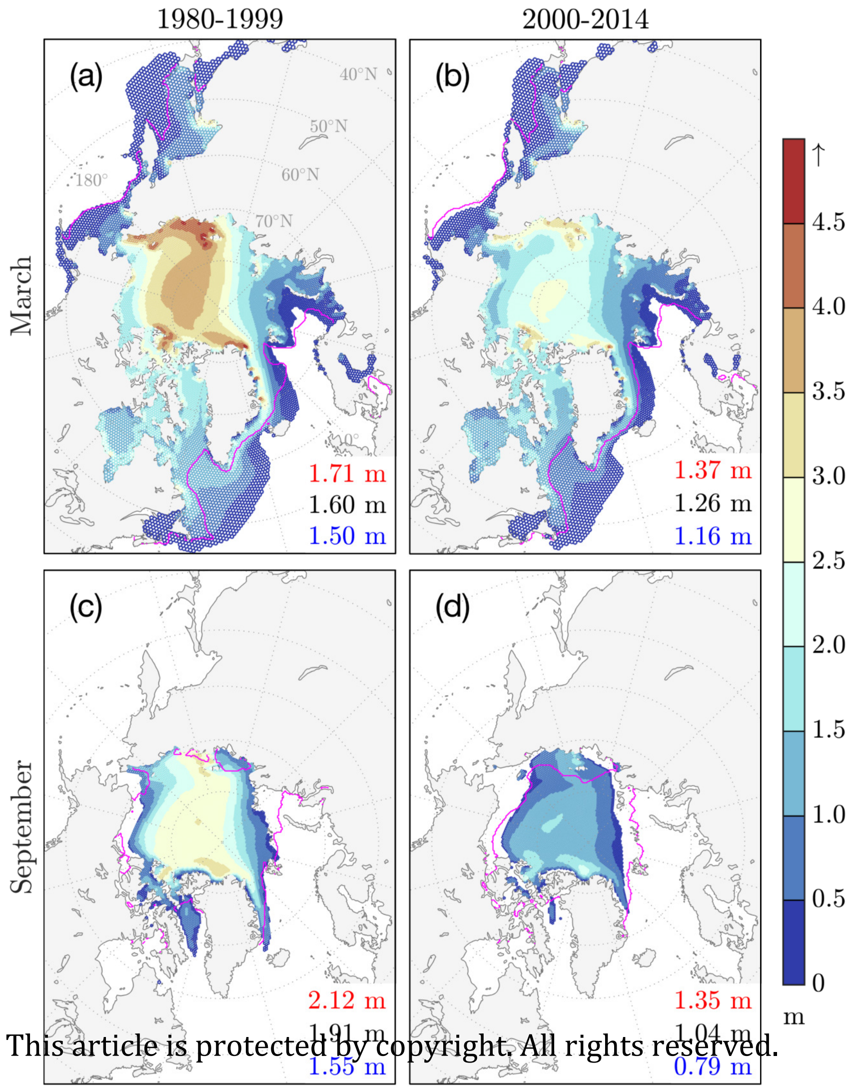
1980-1999
2000-2014
March
September
(a)
40°N
50°N
60°N
70°N
180°
1.71 m
1.60 m
1.50 m
(b)
1.37 m
1.26 m
1.16 m
(c)
2.12 m
1.91 m
1.55 m
(d)
1.35 m
1.04 m
0.79 m
↑
4.5
4.0
3.5
3.0
2.5
2.0
1.5
1.0
0.5
0
m

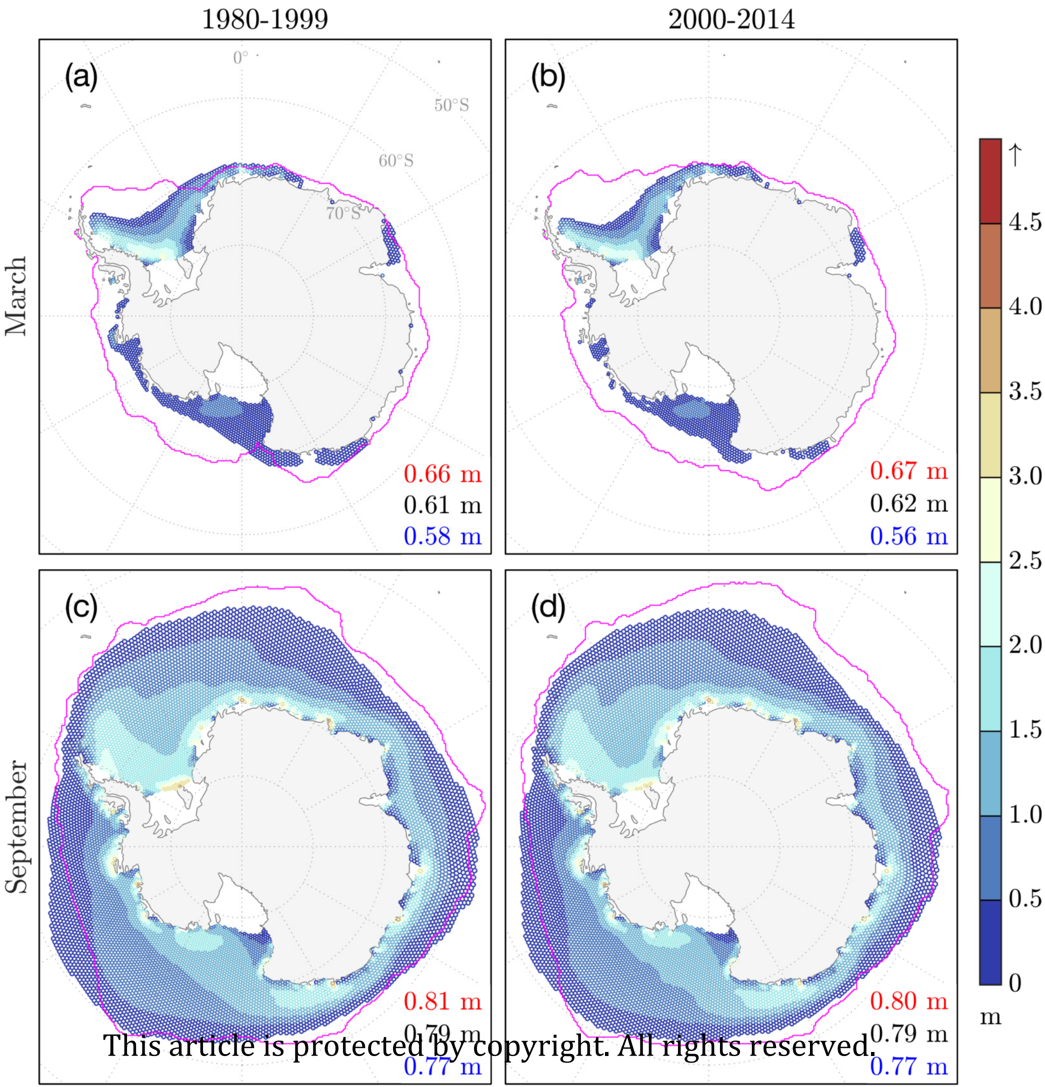
1980-1999
2000-2014
March
September
(a)
(b)
(c)
(d)
0°
50°S
60°S
70°S
0.66 m
0.61 m
0.58 m
0.67 m
0.62 m
0.56 m
0.81 m
0.79 m
0.77 m
0.80 m
0.79 m
0.77 m
4.5
4.0
3.5
3.0
2.5
2.0
1.5
1.0
0.5
0
m

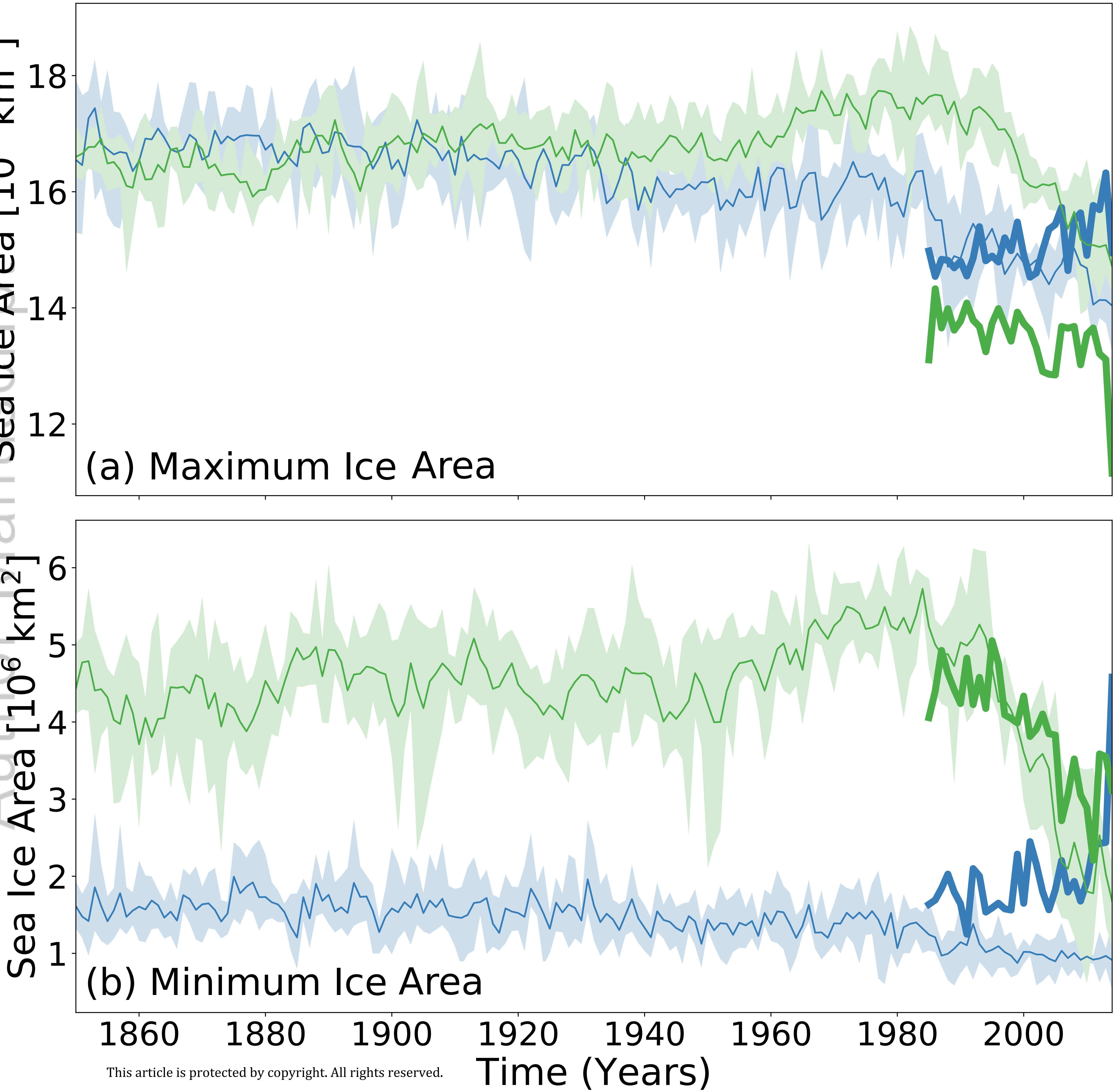

Sea Ice Area [10^6 km^2]
18
16
14
12
(a) Maximum Ice Area
Sea Ice Area [10^6 km^2]
6
5
4
3
2
1
(b) Minimum Ice Area
1860
1880
1900
1920
1940
1960
1980
2000
Time (Years)

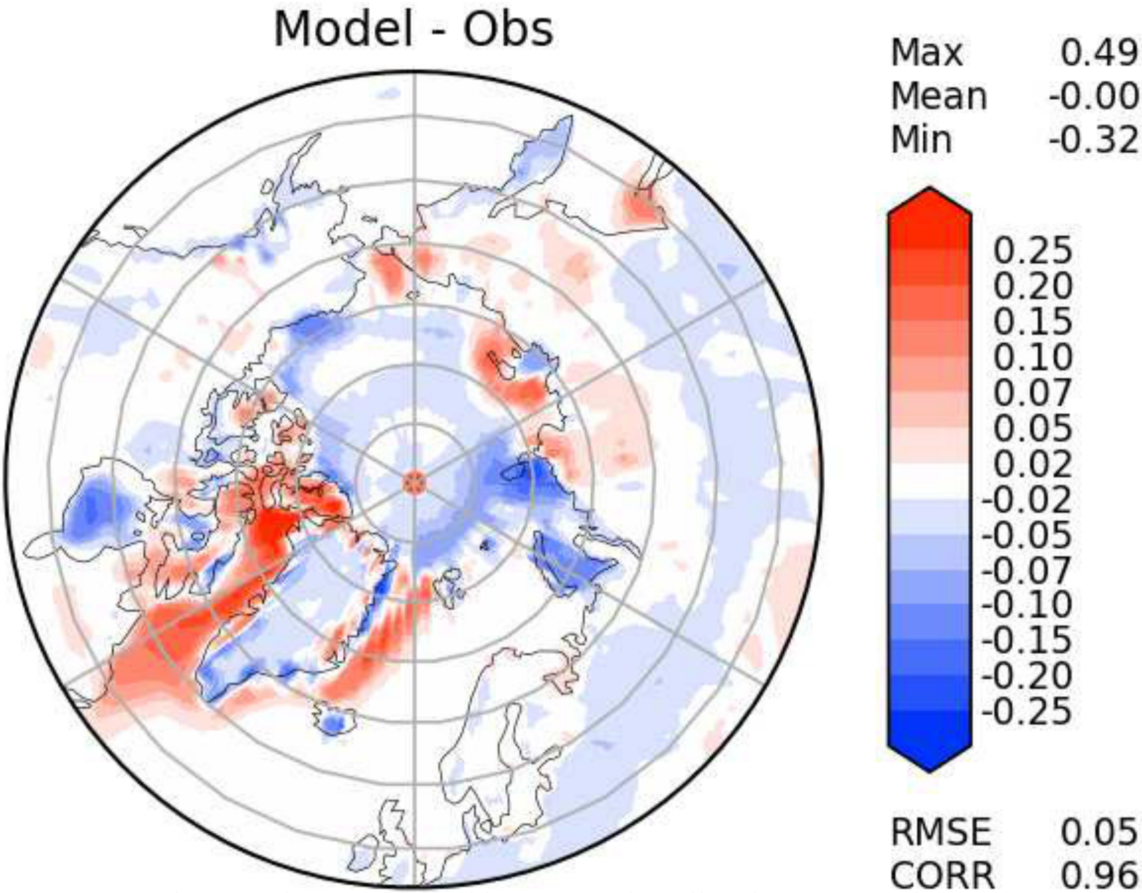
Model - Obs
Max 0.49
Mean -0.00
Min -0.32
0.25
0.20
0.15
0.10
0.07
0.05
0.02
-0.02
-0.05
-0.07
-0.10
-0.15
-0.20
-0.25
RMSE 0.05
CORR 0.96

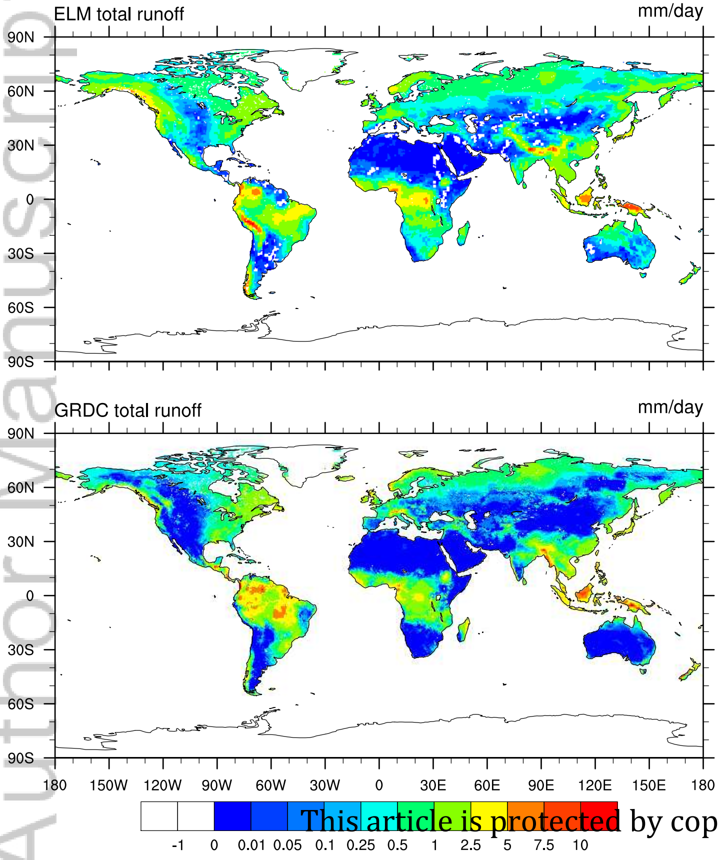
ELM total runoff
mm/day
90N
60N
30N
0
30S
60S
90S
GRDC total runoff
mm/day
180
150W
120W
90W
60W
30W
0
30E
60E
90E
120E
150E
180
-1
0
0.01
0.05
0.1
0.25
0.5
1
2.5
5
7.5
10

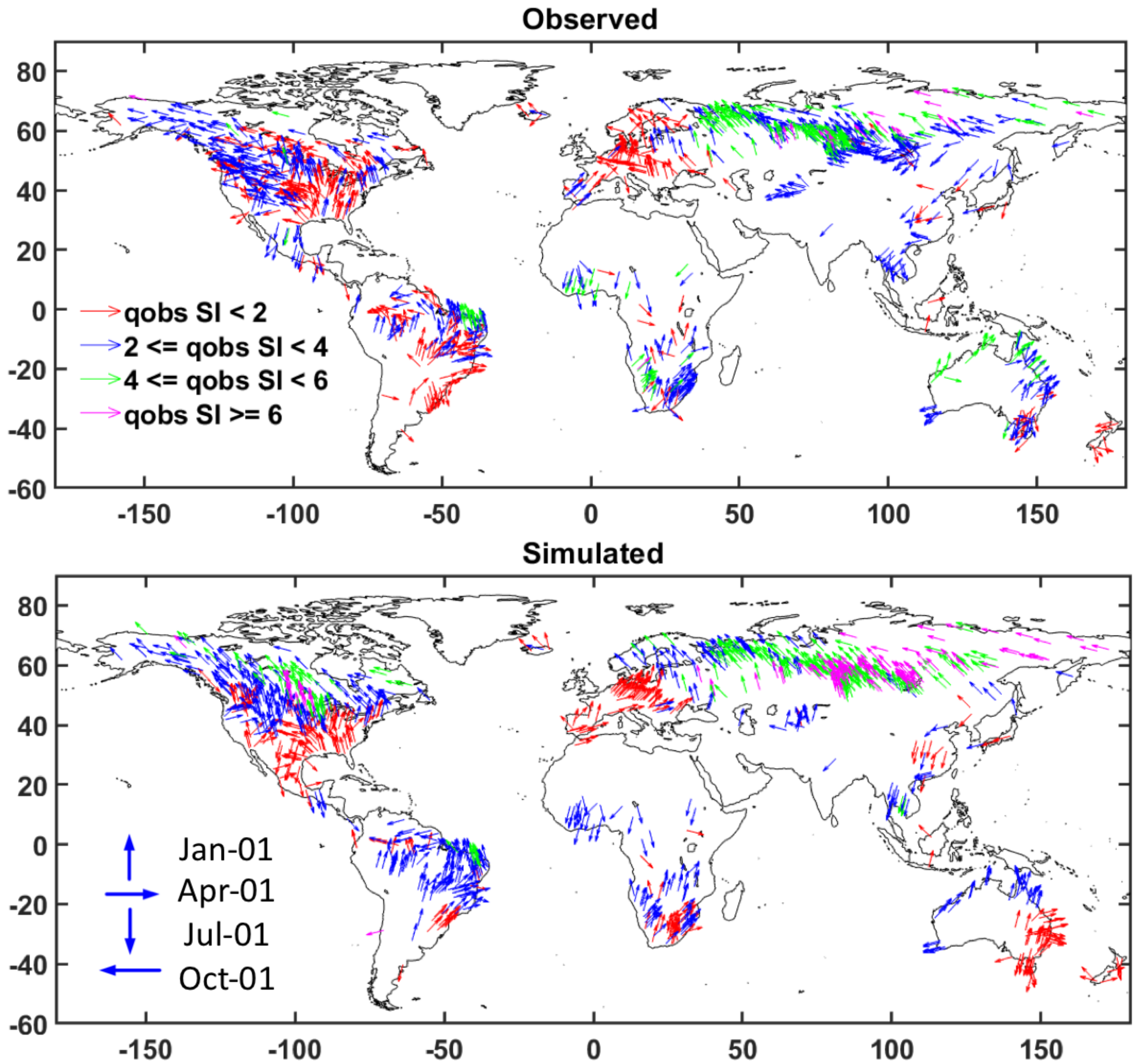

2018MS001603-f19-z-.png

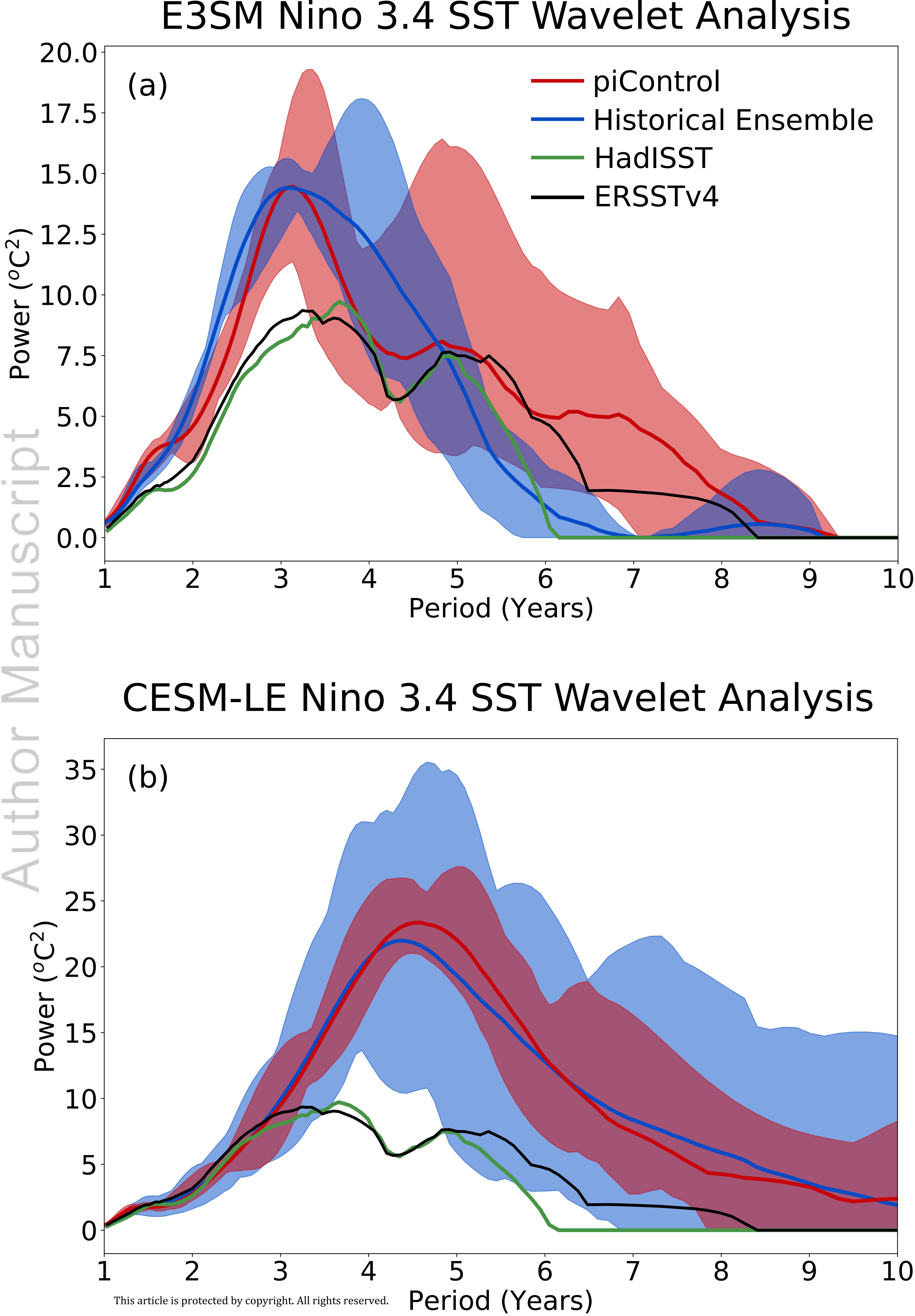
E3SM Nino 3.4 SST Wavelet Analysis
(a)
piControl
Historical Ensemble
HadISST
ERSSTv4
Power ($^oC^2$)
Period (Years)
CESM-LE Nino 3.4 SST Wavelet Analysis
(b)
Power ($^oC^2$)
Period (Years)

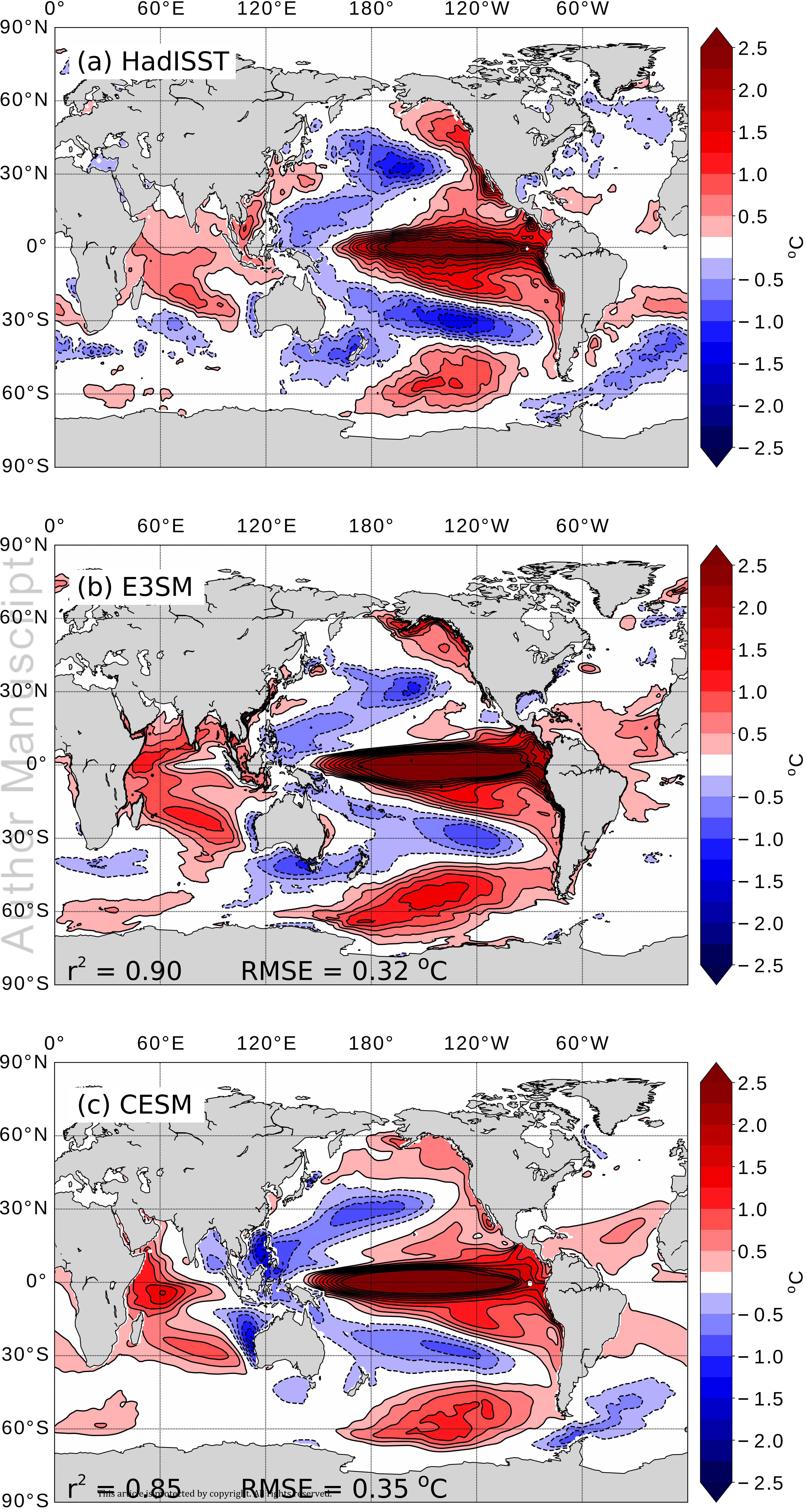
(a) HadISST
(b) E3SM
(c) CESM
0°
60°E
120°E
180°
120°W
60°W
90°N
60°N
30°N
0°
30°S
60°S
90°S
2.5
2.0
1.5
1.0
0.5
−0.5
−1.0
−1.5
−2.0
−2.5
°C
r² = 0.90 RMSE = 0.32 °C
r² = 0.85 RMSE = 0.35 °C

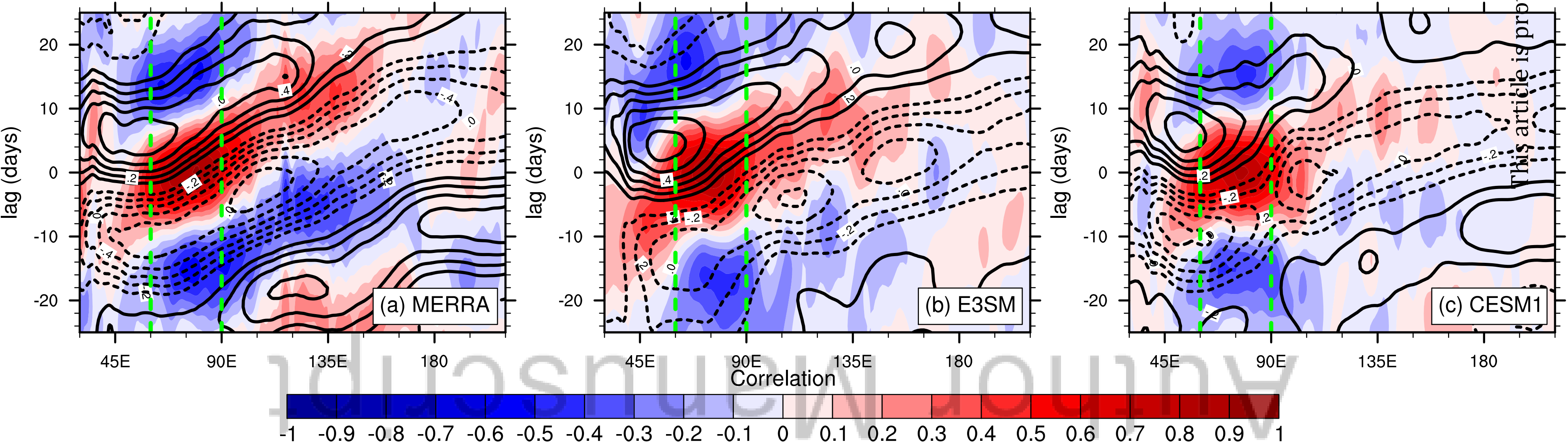
(a) MERRA
(b) E3SM
(c) CESM1
lag (days)
45E
90E
135E
180
Correlation
-1 -0.9 -0.8 -0.7 -0.6 -0.5 -0.4 -0.3 -0.2 -0.1 0 0.1 0.2 0.3 0.4 0.5 0.6 0.7 0.8 0.9 1

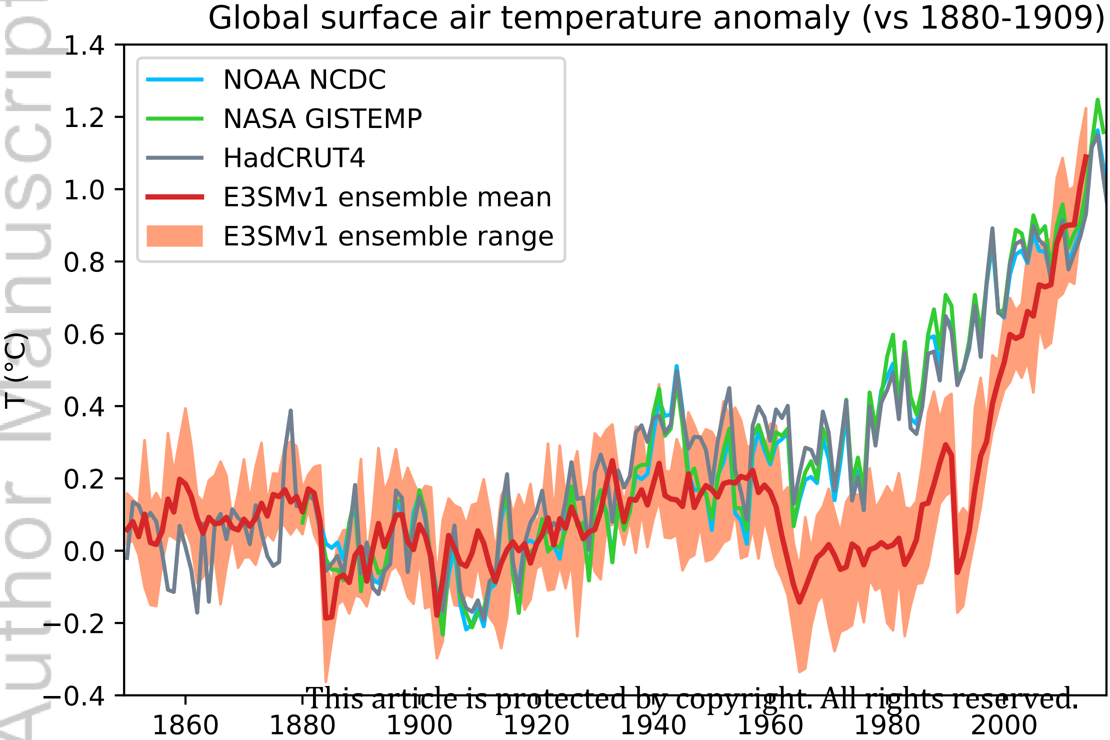
Global surface air temperature anomaly (vs 1880-1909)
NOAA NCDC
NASA GISTEMP
HadCRUT4
E3SMv1 ensemble mean
E3SMv1 ensemble range
T (°C)
1.4
1.2
1.0
0.8
0.6
0.4
0.2
0.0
−0.2
−0.4
1860
1880
1900
1920
1940
1960
1980
2000

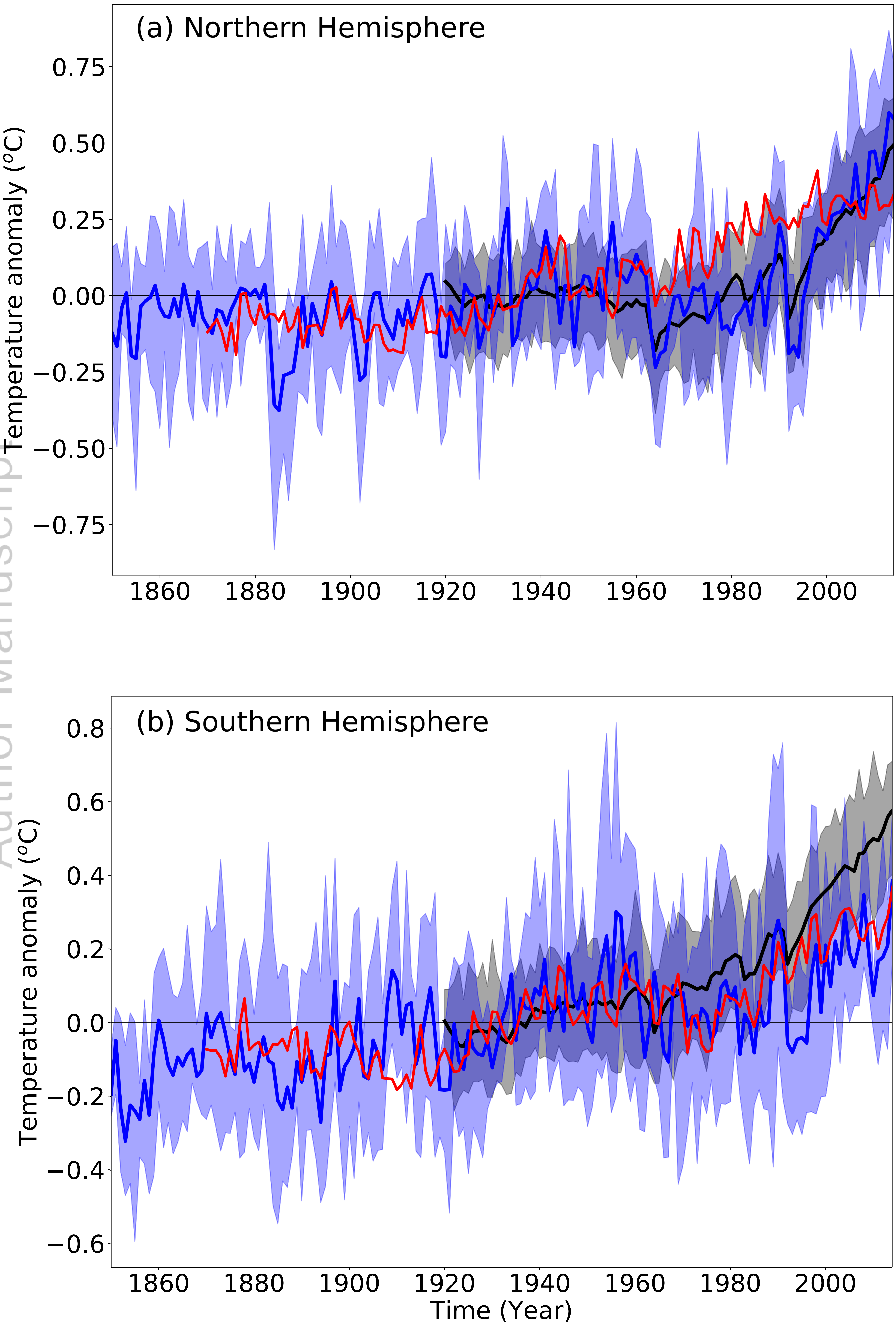

(a) Northern Hemisphere
0.75
0.50
0.25
0.00
−0.25
−0.50
−0.75
Temperature anomaly (^{o}C)
1860
1880
1900
1920
1940
1960
1980
2000
(b) Southern Hemisphere
0.8
0.6
0.4
0.2
0.0
−0.2
−0.4
−0.6
Temperature anomaly (^{o}C)
1860
1880
1900
1920
1940
1960
1980
2000
Time (Year)

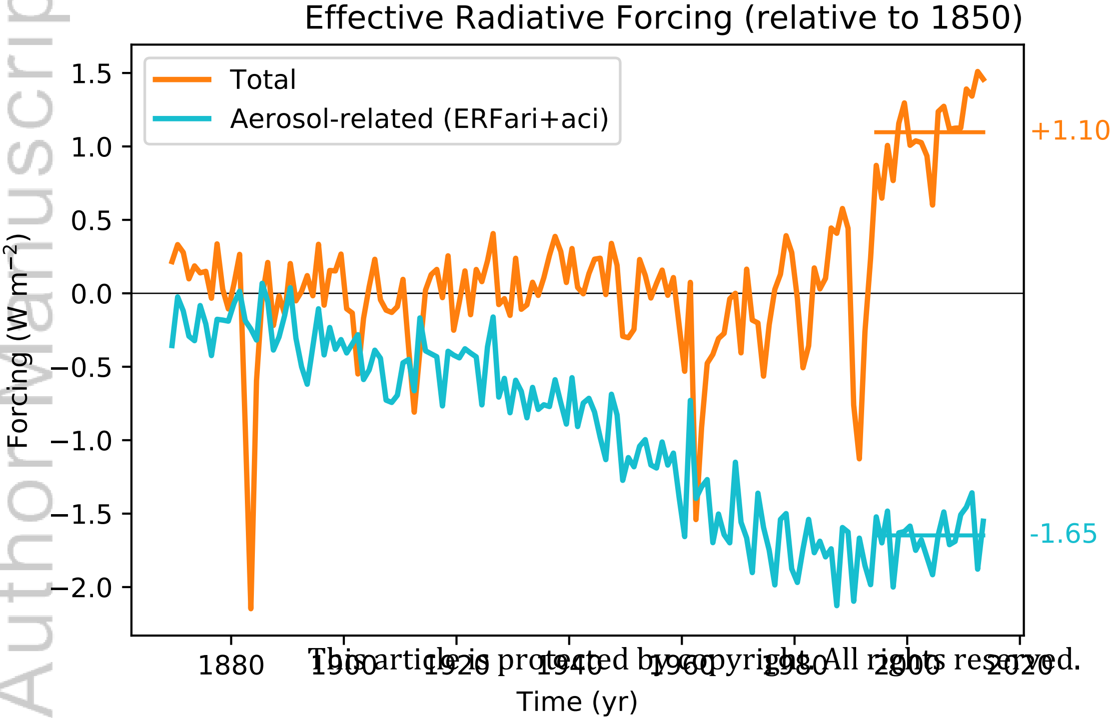
Effective Radiative Forcing (relative to 1850)
Total
Aerosol-related (ERFari+aci)
Forcing (W m^{-2})
1.5
1.0
0.5
0.0
−0.5
−1.0
−1.5
−2.0
+1.10
-1.65
1880
1900
1920
1940
1960
1980
2000
2020
Time (yr)

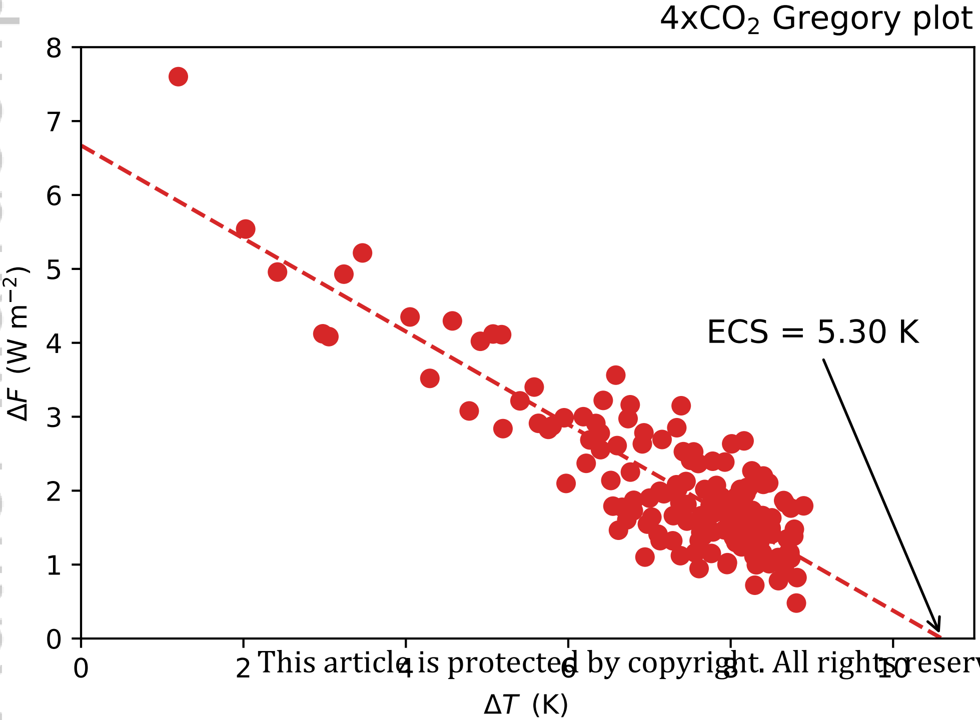
4xCO2 Gregory plot
ECS = 5.30 K
ΔF (W m−2)
ΔT (K)
0
1
2
3
4
5
6
7
8
0
2
4
6
8
10

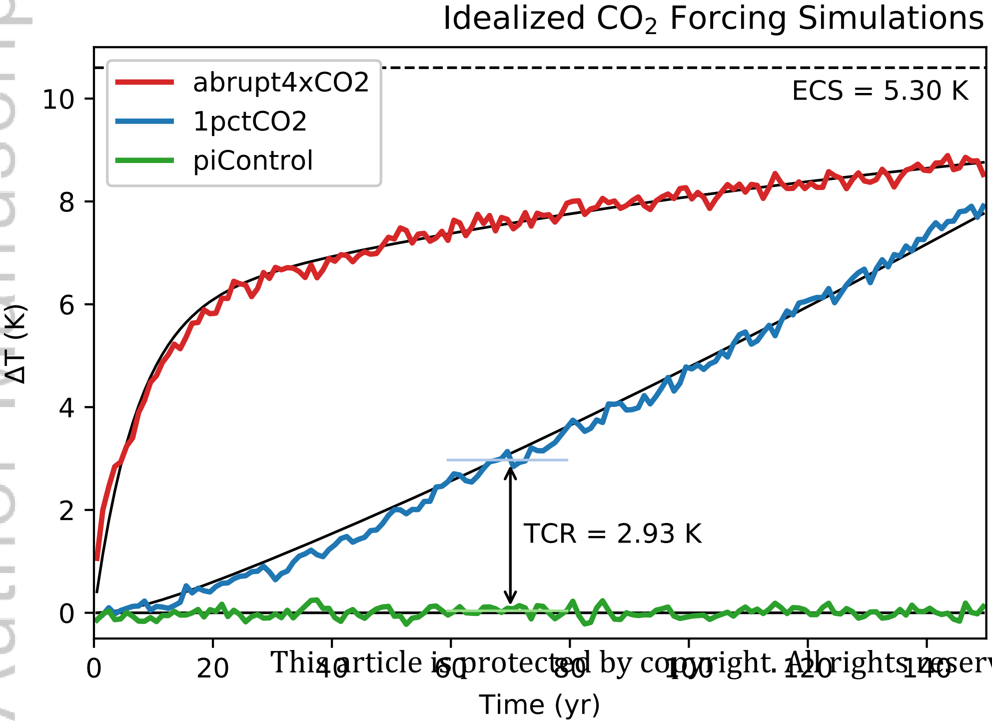
Idealized CO_2 Forcing Simulations
abrupt4xCO2
1pctCO2
piControl
ECS = 5.30 K
TCR = 2.93 K
ΔT (K)
0
2
4
6
8
10
0
20
40
60
80
100
120
140
Time (yr)

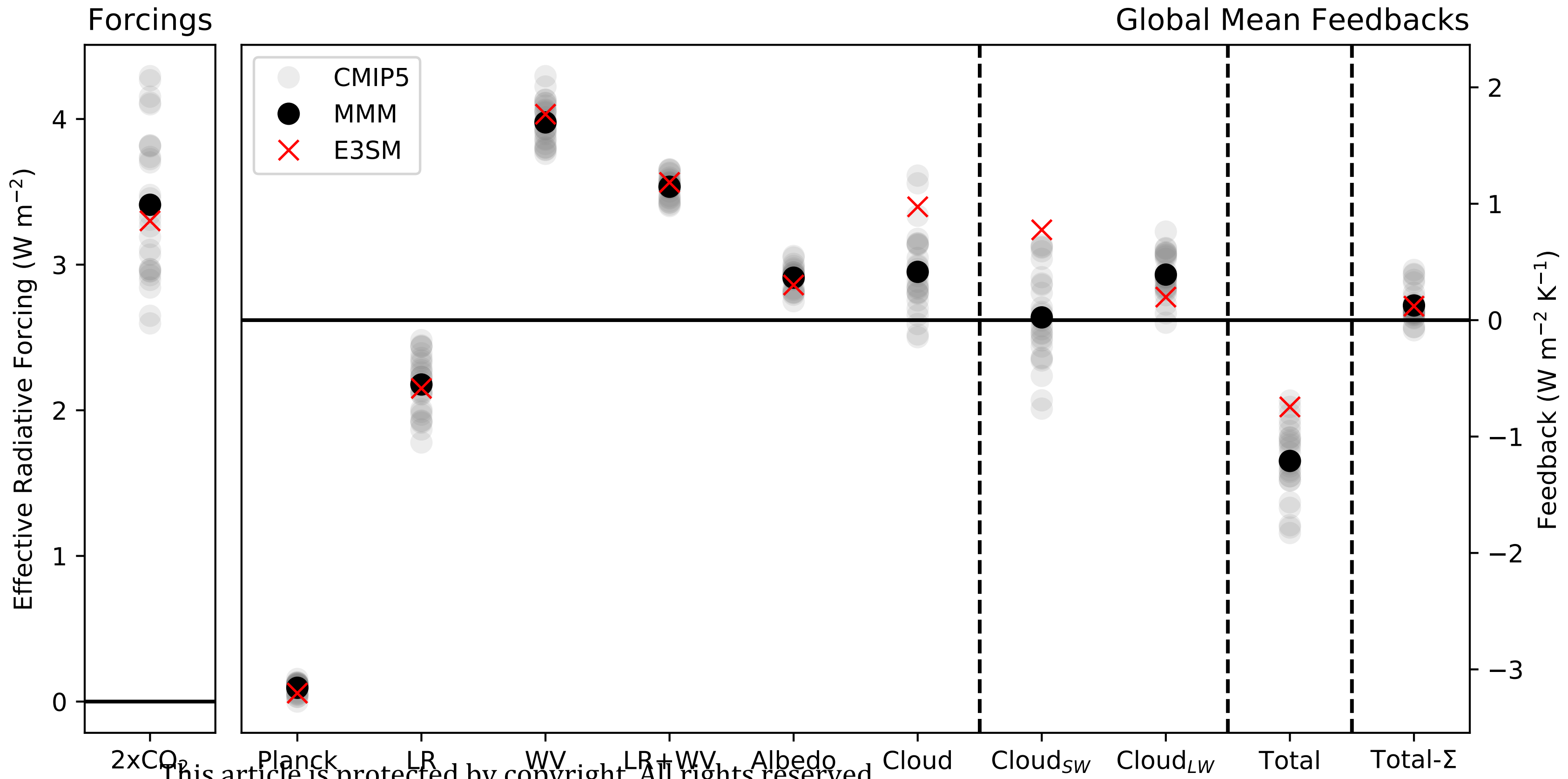
Forcings
Global Mean Feedbacks
CMIP5
MMM
E3SM
Effective Radiative Forcing (W m^{-2})
Feedback (W m^{-2} K^{-1})
0
1
2
3
4
2
1
0
−1
−2
−3
2xCO$_2$
Planck
LR
WV
LR+WV
Albedo
Cloud
Cloud$_{SW}$
Cloud$_{LW}$
Total
Total-Σ

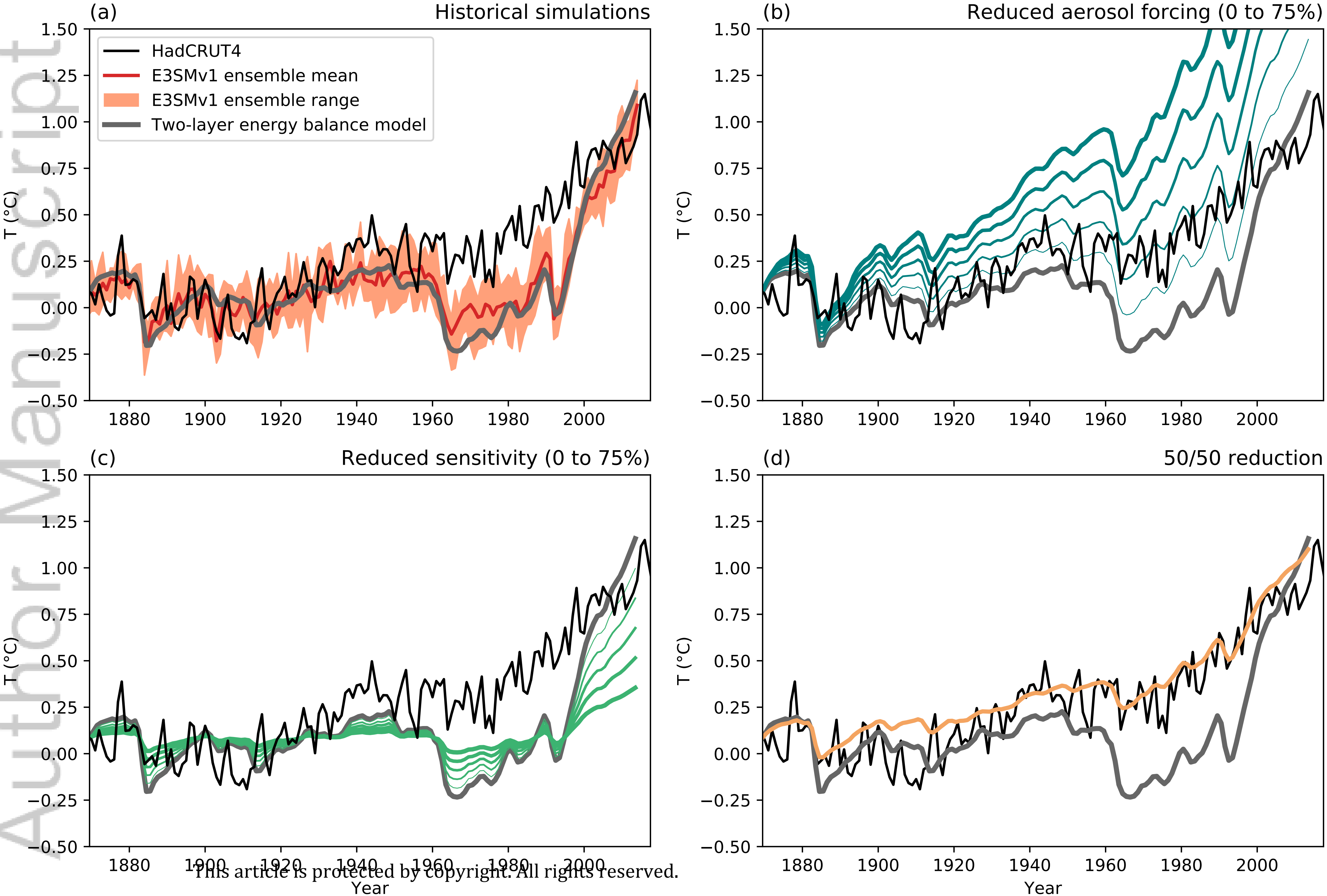
(a)
Historical simulations
HadCRUT4
E3SMv1 ensemble mean
E3SMv1 ensemble range
Two-layer energy balance model
(b)
Reduced aerosol forcing (0 to 75%)
(c)
Reduced sensitivity (0 to 75%)
(d)
50/50 reduction
T (°C)
Year
1.50
1.25
1.00
0.75
0.50
0.25
0.00
−0.25
−0.50
1880
1900
1920
1940
1960
1980
2000

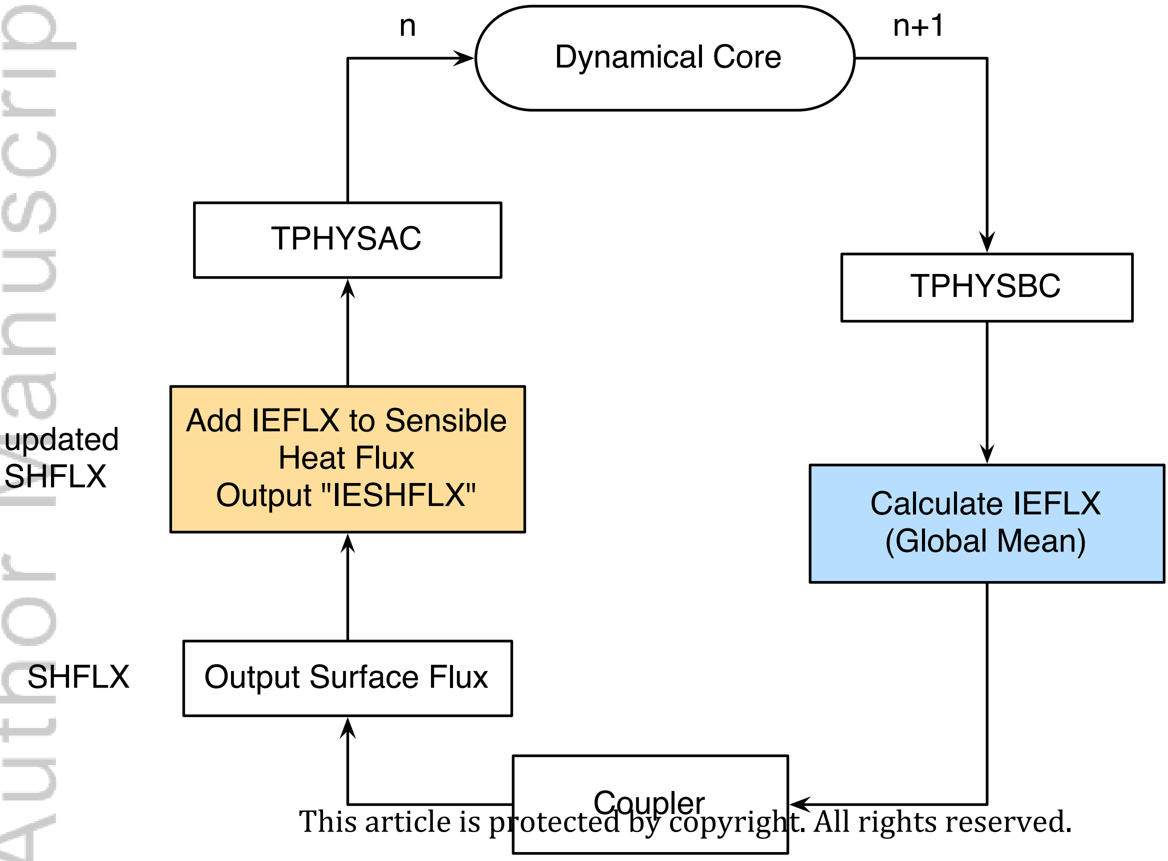

n
Dynamical Core
n+1
TPHYSAC
TPHYSBC
updated
SHFLX
Add IEFLX to Sensible
Heat Flux
Output "IESHFLX"
Calculate IEFLX
(Global Mean)
SHFLX
Output Surface Flux
Coupler